

**Functional surface nanodroplets for sensitive chemical analysis and  
nanomaterials synthesis**

by

Zixiang Wei

A thesis submitted in partial fulfillment of the requirements for the degree of

Doctor of Philosophy

in

Chemical Engineering

Department of Chemical and Materials Engineering  
University of Alberta

© Zixiang Wei, 2022

# Abstract

Surface nanodroplets are nano-scale droplets immobilized on a solid surface with an immiscible liquid environment. These droplets possess a large surface area to volume ratio and some desirable properties such as a long lifetime and excellent stability, compared to the bulk droplets. Surface nanodroplets can be formed in a simple and highly controllable process of solvent exchange. Thus, surface nanodroplets have the potential to be applied in lab-on-chip device design, highly sensitive chemical sensing, micro-reactors, high-resolution imaging, catalytic reaction and others. The novelty of our works is that we applied the advantages of accelerated mass transfer and reaction rate of the surface nanodroplet in fast acid mixture detection and controllable surface-bound materials synthesis.

This thesis reports acid detection and nanomaterials synthesis by using functional surface nanodroplets. The surface nanodroplets containing halochromic chemical compounds are formed by solvent exchange. A colorimetric reaction takes place in the droplets by extracting acidic analyte from the bulk. The time scale of the color change depends on the droplet size, interfacial properties and the dissociation constant of the analyte. The decoloration time is specific to the acid type, giving the possibility to distinguish the multi-component mixtures. Compared to other acid detectors, surface nanodroplets give a faster and more visualized result based on the color change and show potential in instrument-free detection. Furthermore, a partition shifting down of the analyte is found by the coupled extraction and reaction process of the surface nanodroplet. A higher sensitivity of the colorimetric reaction in droplets is obtained compared to the bulk system. The coupled nanoextraction and chemical reaction

have been theoretically investigated and show good agreement with the experimental results. Finally, the surface nanodroplets are used as the template and nucleation site to fabricate the surface-bound materials from the biphasic reaction. Surface nanodroplets enhanced the biphasic reaction, reducing the need of catalyst and additive chemicals, compared to the reaction in bulk. Micro- or nano-structures of metal and metal oxides are fabricated, which can be applied in photo-catalytic degradation and surface enhancement Raman scattering.

# Preface

The research work in Chapters 2 of the thesis was part of an international research collaboration with Dr. Miaosi Li at Royal Melbourne Institute of Technology (RMIT). The method, data collection and analysis and numerical simulations were my original work, as well as the introduction in Chapter 1.

- Chapter 2 has been published as **Wei, Z.**, Li, M., Zeng, H., & Zhang, X. Integrated nanoextraction and colorimetric reactions in surface nanodroplets for combinative analysis. *Analytical Chemistry*, 2020, 92(18), 12442-12450. I am the main contributor who performed experiments, collected data and wrote the manuscript. Li, M., Zeng, H. and Zhang, X. supervised this project and revised the manuscript.
- Chapter 3 has been published as **Wei, Z.**, You, J., Zeng, H., & Zhang, X. Interfacial partitioning enhances microextraction by multicomponent nanodroplets. *The Journal of Physical Chemistry C*, 2022, 126, 3, 1326–1336. I am the main contributor who performed the experiment, collected the data and wrote the manuscript. You, J. helped to build up the simulation model. Zeng, H. supervised this work. Zhang, X. supervised this work and revised the manuscript.
- Chapter 4 has been published as **Wei, Z.**, Dabodiya, T. S., Chen, J., Lu, Q., Qian, J., Meng, J., Zeng, H., Qian, Hui. & Zhang, X. In-situ fabrication of

metal oxide nanocaps based on biphasic reactions with surface nanodroplets. *Journal of Colloid and Interface Science*, 2021, 608(3), 2235-2245. I am the main contributor who performed the experiment, collected the data and wrote the manuscript. Dabodiya, T. S. performed the experiment and wrote the manuscript. Chen, J. performed the characterization and simulation and wrote the manuscript. Lu, Q., Qian, J. and Meng, J. assisted in the experiment and sample preparation. Zeng, H., Qian, Hui. and Zhang, X. supervised this work and revised the manuscript.

- Chapter 5 is under preparation as **Wei, Z.**, Li, Y., Zeng, H., & Zhang, X. Nanorings of silver nanoparticles for surface enhancement Raman scattering. I am the main contributor who performed the experiment, collected the data and wrote the manuscript. Li, Y. helped to prepare the sample. Zeng, H. supervised this work. Zhang, X. supervised this work and revised the manuscript.

*"Life is like riding a bicycle. To keep your balance, you must keep moving."*

*- Albert Einstein*

# Acknowledgments

When I recall the days during my Ph.D. in the past three and half years, I would like to express my sincere gratitude for the support and help from many people.

First of all, I would like to express my deep and sincere gratitude to my supervisor Dr. Xuehua Zhang, for your support, careful guidance, patience and encouragement throughout my study. All your kind comments benefit me in improving my writing skills, thinking critically, presenting the work in a practical way, keeping me self-motivated. All of this has been invaluable throughout my life.

Then, I would like to thank my co-supervisor Dr. Hongbo Zeng for your support and encourage during my study. Your positive attitude always encourages me.

I would like to acknowledge my supervisor committee Dr. John M. Shaw for your valuable comments on my research and thesis.

I am greatly indebted to many researchers. I would thank (in no particular order) Dr. Miaosi Li, Dr. Jiasheng Qian, Dr. Jay Bem You, Hui Qian, Dr. Jian Chen, Qiuyun Lu, Jia Meng, Qimeng Yang, Yanan Li, Yawen Gao, Tulsı Satyavir Dabodiya, Zhengxin Li, Zhipeng Yu and all of the other members in Soft Matter & Interfaces Group for your help and valuable suggestions for my research.

I am incredibly grateful to my parents, Hongshuan Wei and Ling Wang, for your love and encouragement. Without your support, I would not be able to complete my Ph.D. study.

# Table of Contents

|          |  |          |
|----------|--|----------|
| <b>1</b> | <b>Introduction</b>  | <b>1</b> |
| 1.1      | Extraction, reaction and nanomaterial fabrication of microdroplets . . . . . | 1        |
| 1.1.1    | Microdroplets for chemical extraction enhancement . . . . .                  | 1        |
| 1.1.2    | Microdroplets for chemical reaction acceleration . . . . .                   | 7        |
| 1.1.3    | Microdroplets for materials synthesis . . . . .                              | 10       |
| 1.2      | Surface nanodroplets . . . . .   | 11       |
| 1.3      | Ouzo effect . . . . .  | 13       |
| 1.4      | Formation of surface nanodroplets by solvent exchange . . . . .              | 14       |
| 1.4.1    | Flow conditions for the solvent exchange . . . . .                           | 16       |
| 1.4.2    | Geometry of the fluid chamber . . . . .                                      | 19       |
| 1.4.3    | Effects from solution composition . . . . .                                  | 20       |
| 1.4.4    | Effects of physicochemical properties of the substrate . . . . .             | 22       |
| 1.5      | Chemical reactions of surface nanodroplets . . . . .                         | 32       |
| 1.6      | Applications of surface nanodroplets . . . . .                               | 33       |
| 1.6.1    | Surface nanodroplets for chemical sensing . . . . .                          | 33       |
| 1.6.2    | Surface nanodroplets for optical enhancement . . . . .                       | 34       |
| 1.7      | Thesis Objectives . . . . .  | 37       |
| 1.8      | Thesis Outline . . . . .   | 38       |
| <b>2</b> | <b>Integrated nanoextraction and colorimetric reactions in surface nan-</b>  |          |

|  |           |
|--|-----------|
| <b>droplets for combinative analysis</b>   | <b>42</b> |
| 2.1 Introduction . . . . .   | 42        |
| 2.2 Experimental section . . . . .   | 45        |
| 2.2.1 Chemicals and materials . . . . .  | 45        |
| 2.2.2 Formation of pH sensitive femtoliter droplets . . . . .  | 46        |
| 2.2.3 Detection of acids in oil phase . . . . .  | 47        |
| 2.2.4 Detection of acids in an organic phase by bulk mixing . . . . .  | 49        |
| 2.2.5 Colorimetric identification of acid mixtures and anti-counterfeiting<br>of alcohol spirits by droplets . . . . . | 49        |
| 2.3 Results and discussion . . . . .   | 51        |
| 2.3.1 Formation of colored droplets for acid extraction and detection  | 51        |
| 2.3.2 Sensitivity of colorimetric reaction in droplets . . . . .   | 52        |
| 2.3.3 Acid specificity of colorimetric reaction rate in droplets . . . . .   | 54        |
| 2.3.4 Colorimetric analysis of acid mixtures for anti-counterfeiting<br>alcoholic drinks . . . . .                     | 62        |
| 2.4 Conclusions . . . . .  | 64        |
| <br>   |           |
| <b>3 Interfacial partitioning enhances microextraction by multicomponent nanodroplets</b>                              | <b>66</b> |
| 3.1 Introduction . . . . .   | 66        |
| 3.2 Experimental section . . . . .   | 70        |
| 3.2.1 Chemicals and materials . . . . .  | 70        |
| 3.2.2 Formation of functional surface nanodroplets . . . . .   | 71        |
| 3.2.3 Extraction of acid from the flow and colorimetric reaction in<br>droplets . . . . .                              | 72        |
| 3.2.4 Determination of temporal solute concentration in the flow . . .   | 73        |
| 3.3 Results and discussion . . . . .   | 74        |
| 3.3.1 Temporal concentration of the solute in the external flow . . .  | 74        |

|       |  |    |
|-------|--|----|
| 3.3.2 | Partition-dominated droplet decoloration at high concentration of acids . . . . .                        | 76 |
| 3.3.3 | Enhanced partition at low concentration of acids . . . . .   | 78 |
| 3.3.4 | Interfacial partition enhanced by nanodroplets reaction . . . . .  | 81 |
| 3.3.5 | Theoretical decoloration rate coupling interfacial partition and chemical reaction in droplets . . . . . | 83 |
| 3.3.6 | Rate-limiting step in droplet decoloration at low acid concentration . . . . .                           | 84 |
| 3.3.7 | Acid specificity of mass transfer coefficient $\beta$ . . . . .  | 85 |
| 3.3.8 | Effects of reactant concentration in droplets on reaction rates  | 90 |
| 3.4   | Conclusions . . . . .  | 91 |

|          |  |           |
|----------|--|-----------|
| <b>4</b> | <b>In-situ fabrication of metal oxide nanocaps based on biphasic reactions with surface nanodroplets</b> | <b>94</b> |
| 4.1      | Introduction . . . . .   | 94        |
| 4.2      | Experimental section . . . . .   | 97        |
| 4.2.1    | Chemicals and materials . . . . .  | 97        |
| 4.2.2    | Preparation of metal oxide nanocaps on a substrate . . . . .   | 97        |
| 4.2.3    | Preparation of porous iron oxide nanocaps from binary droplets   | 98        |
| 4.2.4    | Characterization of size and structures of metal oxide nanocaps  | 100       |
| 4.2.5    | Photodegradation catalyzed by iron oxide nanocaps . . . . .  | 101       |
| 4.3      | Results and discussion . . . . .   | 104       |
| 4.3.1    | Formation and morphology of iron oxide nanocaps . . . . .  | 104       |
| 4.3.2    | Effect of time and temperature of heating . . . . .  | 106       |
| 4.3.3    | Formation of porous nanocaps from binary surface nanodroplets  | 112       |
| 4.3.4    | Formation of other metal oxide nanocaps . . . . .  | 115       |
| 4.3.5    | Porous nanocaps for photodegradation . . . . .   | 117       |
| 4.4      | Conclusions . . . . .  | 118       |

|          |  |            |
|----------|--|------------|
| <b>5</b> | <b>Nanorings of silver nanoparticles for surface enhancement Raman scattering (SERS)</b> | <b>126</b> |
| 5.1      | Introduction . . . . .   | 126        |
| 5.2      | Experimental section . . . . .   | 130        |
| 5.2.1    | Chemicals and materials . . . . .  | 130        |
| 5.2.2    | Formation of highly order array of surface nanodroplets array                            | 130        |
| 5.2.3    | Fabrication of ring array of silver nanoparticles . . . . .                              | 131        |
| 5.2.4    | Detection of model compounds by SERS . . . . .   | 131        |
| 5.2.5    | Characterization . . . . .   | 132        |
| 5.3      | Results and discussion . . . . .   | 134        |
| 5.3.1    | Fabrication of array of nanorings . . . . .  | 134        |
| 5.3.2    | SERS detection by using nanorings of silver nanoparticles . . .                          | 136        |
| 5.3.3    | Enhanced detection by SERS substrate . . . . .   | 139        |
| 5.4      | Conclusions . . . . .  | 141        |
| <b>6</b> | <b>Conclusions and outlook</b>   | <b>144</b> |
| 6.1      | Conclusions . . . . .  | 144        |
| 6.2      | Outlook . . . . .  | 146        |
|          | <b>Bibliography</b>  | <b>148</b> |

# List of Tables

|     |  |    |
|-----|--|----|
| 2.1 | Molar mass, pKa and LgP of each acid from literature . . . . .   | 46 |
| 2.2 | Composition of different acid mixtures. . . . .  | 50 |
| 2.3 | pH value of Chinese spirit . . . . .   | 50 |
| 2.4 | LOD of different acids by using BG droplets and the calculated LgP of each acid. . . . .   | 61 |
| 3.1 | Dissociation constant (pKa), partition coefficient (LgP), critical concentration ( $C_w^*$ ) and molecular structure (MS) of the acids used in this work. . . . .  | 71 |
| 3.2 | Decoloration time of 5 $\mu m$ droplets from 5 mM of acid and the acid concentration ( $C_w$ ) in the droplets calculated from partition coefficient LgP. . . . .  | 79 |
| 3.3 | Mass transfer coefficient ( $\beta$ ), reaction coefficient (r) and apparent distribution constant ( $p^*$ ) of acetic acid and aromatic acid at the concentration ( $C_o$ ) of 0.5 mM to 5mM in the octanol solution. . . . .   | 86 |
| 3.4 | Mass transfer coefficient ( $\beta$ ), reaction coefficient (r) and apparent distribution constant ( $p^*$ ) of acetic acid and aromatic acid at the concentration ( $C_o$ ) of 50 mM to 100 mM in the octanol solution. . . . . | 87 |
| 3.5 | Mass transfer coefficient ( $\beta$ ), reaction coefficient (r) and apprent distribution constant ( $p^*$ ) of long-chain alkyl acid at the concentration ( $C_o$ ) in octanol solution. . . . .                                 | 88 |

|     |  |     |
|-----|--|-----|
| 4.1 | Experimental conditions for fabrication of metal oxide nanocaps. . . .   | 101 |
| 4.2 | XPS peaks of Fe2p . . . . .  | 108 |
| 4.3 | XPS peaks of O1s and C1s . . . . .   | 109 |
| 5.1 | List of the reported LoD on highly ordered substrate for SERS. . . .   | 129 |
| 5.2 | The conditions (pH value and concentrations) of the precursor solution<br>and the corresponding LoD and quantification range . . . . . | 132 |
| 5.3 | Assignment for the peaks in Raman spectra of R6G molecule[221] . .   | 134 |

# List of Figures

|     |  |    |
|-----|--|----|
| 1.1 | Applications of micro-scale droplets on solid substrate. (With permissions from Ref.[7]. Copyright (2019) American Physical Society.) . . .  | 2  |
| 1.2 | General sketch of the single-drop microextraction: Direct-SDEM (right) and HS-SDME (left). . . . .   | 4  |
| 1.3 | General sketch of the dispersive liquid-liquid microextraction procedure. (With permissions from Ref.[22]. Copyright (2011) Elsevier Ltd.)   | 6  |
| 1.4 | Dependence of the rate constants on reaction energy for the dilute gas phase (a), microdroplet interface (b), and bulk phase (c). A and B refer to two different reactants, S refers to solvent molecules, and C and D are two products. In order to make an analogy to gas-phase reactions, A is assumed to be the ionic form and B is neutral. A plus sign indicates that two particles are far from each other. An ellipsis indicates that the two particles are approaching but no bond is formed. A minus sign indicates bond formation. (With permissions from Ref.[29]. Copyright (2020) Annual Reviews.) . . . . . | 9  |
| 1.5 | General sketch of the surface nanodroplets. . . . .  | 12 |
| 1.6 | Sketch of the Ouzo region in ternary phase diagram. (With permissions from Ref.[62]. Copyright (2016) Elsevier Ltd.) . . . . .   | 15 |

|      |  |    |
|------|--|----|
| 1.7  | Sketch of the formation of permanent surface lens by surface nanodroplets. (With permissions from Ref.[64]. Copyright (2012) Royal Society of Chemistry) . . . . .   | 16 |
| 1.8  | Sketch of the fluid chamber for solvent exchange process. (With permissions from Ref.[65]. Copyright (2015) American Physical Society).  | 17 |
| 1.9  | Sketch of solvent exchange process at different angles. (With permissions from Ref.[70]. Copyright (2015) American Chemical Society) . .   | 20 |
| 1.10 | A sketch of the solvent exchange under the microchannel structure with the notations of the geometrical parameters. $w$ is the lateral channel width, $h_c$ is the channel height, $h_g$ is the gap height, and $l_g$ is the length of the gap. (With permissions from Ref.[71]. Copyright (2017) Royal Society of Chemistry) . . . . .  | 21 |
| 1.11 | Sketch of the solution composition during the solvent exchange in a three-phase diagram. (a) The initial solution composition at $X_0$ is undersaturated with water. The dilution curve is the red line, following which the solution becomes saturated at $X_s$ . The temporary over-saturation level of water at point C is the projection of line CD on the water axis. (b) The overall over-saturation level is reflected by blue shaded area A. (c) $X_s$ is above the Ouzo region. Macroscopic phase separation occurs along the tie line (dotted red line). The oil-rich sub-phase at $X'_s$ contributes to droplet formation. (d) The droplet size increases almost linearly with $A^{0.5}$ . (With permissions from Ref.[72]. Copyright (2016) American Chemical Society) . . . . . | 23 |
| 1.12 | (a) Plots of binary droplet composition compared to the component ratio in solution A. (b) Sketch shows the calculation of the over-saturation level from the solubility phase diagram with a known oil-to-ethanol initial ratio. (With permissions from Ref.[74]. Copyright (2018) American Chemical Society) . . . . .   | 24 |

|      |   |    |
|------|---|----|
| 1.13 | Representative optical image of polymerised nanodroplets (a), and the corresponding modified Voronoi tessellation (b), which is based on the distance between two the footprints of adjacent droplets. In (c) schematic top & side views. $N_d$ is the number of molecules in the droplet, and $N_V$ is the original number of molecules in the depleted volume around the droplet, which scales as $\sim A^{3/2}$ . (With permissions from Ref.[75]. Copyright (2017) Royal Society of Chemistry) . . . . .  | 25 |
| 1.14 | (a)–(l) Morphology and size of the polymerized droplets formed on pre-patterned hydrophobic substrates at five different oil concentrations $C_m$ . (With permissions from Ref.[77]. . . . .  | 27 |
| 1.15 | The sketch of droplet growth on patterned substrate under constant angle (CA) mode and constant radius (CR) mode. (With permissions from Ref.[78]. Copyright (2016) American Chemical Society) . . . . .  | 28 |
| 1.16 | Spatial arrangement of the nanodroplets around the microcap. (a, b) AFM and SEM images of nanodroplets sitting on a microcap. (c) Notation of the nanodroplets and the microcap. (d–i) AFM images of multiple nanodroplets around one microcap with Symmetric N-gons from N=2-7 (d–i). (j) Representation of the coalescence model when N = 9, 6, 3, respectively. The respective angles $\Phi$ between the droplets before and after the coalescence process are also shown. (k) Angle $\Phi$ (light blue line) and average angle $\bar{\Phi}$ (red line) between droplets vs. $r/R$ as revealed from the model. (Reproduced With permissions from Ref.[79]. Copyright (2015) American Chemical Society and Ref.[80]. Copyright (2018) Royal Society of Chemistry) . . . . . | 30 |

|      |   |    |
|------|---|----|
| 1.17 | (a) Imaging analysis process by using Matlab software: 1. Image contrast enhancement and binarization; 2. edge detection; 3. surface droplet detection; 4. circle fit through all detected droplets. The mean diameter of droplets was obtained as the intersection of points between the fitted circles and the surface of the fiber. (b) Confocal microscopy image of surface droplets on the microfiber. The shape of the droplets (dyed in red) is that of a clam shell. The definition of the lateral diameter $D_d$ and the height H is notated in the sketch. The ratio of H to $D_d$ is about 0.32. (With permissions from Ref.[81]. Copyright (2018) Royal Society of Chemistry) . . . . . | 31 |
| 1.18 | Sketch of the droplet formed on pH sensitive substrate and $MoS_2$ sample. (With permissions from Ref.[82]. Copyright (2016) American Chemical Society) . . . . .   | 32 |
| 1.19 | a) Schetch of the programmed flow sequence for the automation of formation of functionalised surface droplets. b) Schematic of the extraction, concentration, and in situ detection based on surface droplets. c) The reaction scheme of VE with $AgNO_3$ to produce AgNPs. (With permissions from Ref.[85]. Copyright (2019) John Wiley and Sons) . .  | 35 |

|      |   |    |
|------|---|----|
| 1.20 | (A) TIRF image of microlens decorated substrate immersed in a 50% ethanol solution containing Nile red. Inset shows TIRF image of glass substrate immersed in a 50% ethanol solution containing Nile red. (B) 3D representation of a TIRF image for individual microlens. The height and color map are given by the recorded experimental intensity. The lens is an added schematic. The approximate focal length and enhancement are schematically depicted by the arrows. (C) Tilted SEM of a representative gold decorated microlens and schematic representation of the bubble growth via plasmonic heating. Scale bar = 1 $\mu m$ . (With permissions from Ref.[89]. Copyright (2018) American Chemical Society) . . . . . | 36 |
| 2.1  | Schematic of preparing and applying surface droplets for the extraction and detection of acidic compounds in oil. (a) The sketch of the fluid chamber.(b) The formation process of the surface droplets containing pH indicator by solvent exchange and detection of the acid in oil (Solution C) by droplets contacting with the Oil flow.(c) Acid molecules in the oil phase are extracted into the aqueous droplets and react with halochromic compound in the droplets. . . . .   | 48 |
| 2.2  | Color of a droplet containing halochromic compound before and after contact with acid. Molecular structures of BP and BG are shown on the bottom row. Top row: a droplet before (left) and after (right) in contact with 1-octanol for 5 minutes. Middle row: a droplet before (left) and after (right) contact with octanol containing $1.7 \times 10^{-4} M$ acetic acid for BP droplet in (a) and $1.0 \times 10^{-4} M$ acetic acid for BG droplet in (b). Length of the scale bar: 25 $\mu m$ . . . . .  | 52 |

- 2.3 Test of two bulk mixing methods for detection of acetic acid in octanol by BP (a) and BG (b) aqueous solutions. 0.04% aqueous solutions of BP (1) and BG (1') were perpetrated by mass fraction. From (2) to (5), 1 mL (top row) and 2 mL (bottom row) of prepared BP solution were added into 1ml 1-octanol containing acetic acid from the concentration of  $1.7 \times 10^{-4}M$  to  $1.7 \times 10^{-1}M$  with 10 times intervals. From (2') to (5'), 1 mL (top row) and 2 mL (bottom row) of prepared BG solutions were added into 1 mL 1-octanol containing acetic acid from the concentration of  $1.0 \times 10^{-4}M$  to  $1.0 \times 10^{-1}M$  with 10 times intervals. 55
- 2.4 Detection of acetic acid in oil by surface droplets containing BG. (a) Time series images of droplet discoloration from  $5 \times 10^{-4}M$  acid in oil. The droplet size decreases from the top to the bottom row. Length of the scale bar:  $25 \mu m$ . (b) The color intensity at different time after the droplets in contact with oil containing  $5 \times 10^{-4}M$ . (c) Time series images of droplet discoloration from  $1 \times 10^{-4}M$  acid in oil. (d) The color intensity at different time after the droplets in contact with oil containing  $1 \times 10^{-4}M$ . The error bar is from three repeats of the measurement. . . . . 56
- 2.5 Detection of different acids and acid mixtures in oil by surface droplets containing BG. Time of the droplet discolor as a function of the droplet radius at different concentrations of acetic acid (a). The acid concentration is  $5 mM$  in (b) and  $50 mM$  in (c). (D) Detection of acid mixtures at different ratio in oil by surface droplets containing BG. Acetic acid, gallic acid and benzoic acid were mixed at different ratio, as shown in Table 2.2. Dotted lines are the linear fitting. The error bar is from two to three repeats of the measurement. . . . . 57

|     |  |    |
|-----|--|----|
| 2.6 | Determination of counterfeit Chinese spirit through surface droplet based nanodetector. (a) Time series pictures of the droplet discoloration from Fenjiu. (b) Time series pictures of the droplet discoloration from Erguotou. (c) Time of the droplet discolor versus the reciprocal of the droplet size from different spirit.(d) Time of the droplet discolor versus the reciprocal of the droplet size at two types of Fenjiu. Dotted lines are the linear fittings. The error bar is from three repeats of the measurement. The images of the droplet decoloration in contact with oil that contains compounds extracted from Fenjiu (e) and from Erguotou (f) at 0 s, 180 s and 240 s by using a commercial smartphone camera. (Length of scale bar: 25 $\mu m$ in a,b and 2 $mm$ in e and f) . . . | 65 |
| 3.1 | Sketch of forming droplets (a) and the acid extraction and the colorimetric reaction in the droplets (b). . . . .  | 72 |
| 3.2 | (a) Images of the fluorescence intensity changes during displacing pure octanol by the dye solution. (b) Fluorescence intensity (I) from the solution as a function of time. The dye concentration was $1 \times 10^5$ , $5 \times 10^5$ , and $1 \times 10^4 g/L$ , respectively. (c) Logarithmic plot of maximal fluorescence intensity versus the concentration of the dye in the solution. (d) Error function fitted (dashed line) dye concentration as a function of time at the dye concentration of $1 \times 10^5 g/L$ . . . . .   | 75 |
| 3.3 | (a) Optical images and the time scale of the droplet decoloration in contact with the oil containing 50 mM of different acids. (b) The plot of droplet decolor time as a function of droplet size after injecting oil containing 50 mM of acids. (c) The plot of droplet decolor time as a function of droplet size after injecting oil containing 50 mM, 500 mM and 2500 mM of heptanoic acid. . . . .  | 77 |

|     |   |    |
|-----|---|----|
| 3.4 | <p>(a) Optical images of the same sized droplets (<math>R=25 \mu m</math>) that change color at 5mM of acid in oil. Scale bar: <math>25 \mu m</math>. (b) The plot of droplet decolor time as a function of droplet size after injecting oil containing 5 mM of n-butyric acid and valeric acid. (c) and (d) are the plots of droplet decolor time as a function of droplet size after injecting oil containing 5 mM of acetic acid and aromatic acids, respectively. Solid lines in (b) were fitted from Eq.3.3. Dashed lines in (c) and (d) were fitted from Eq.3.7. . . . . .</p>          | 80 |
| 3.5 | <p>(a) Sketch of four steps in nanoextraction and colorimetric reaction in droplets. Acid molecules penetrated the oil-water interface by direct dissolution and surface adsorption-desorption (step 1: <math>t_1</math>). Acid dissociated to release protons (step 2: <math>t_2</math>). The protons react with the BG, leading to a color change (step 3: <math>t_3</math>). The total time scale of the colorimetric reaction is the combination of those four processes (<math>1/t=1/t_1+1/t_2+1/t_3</math>). (b) The concentration gradient of the acid at the interface. . . . . .</p> | 81 |
| 3.6 | <p>Distribution coefficient shift down with the decrease in the acid concentration in oil (<math>C_o</math>) for heptanoic acid (b) and other acids(a), respectively. (c) <math>\beta</math> from the fitting of Eq.3.1 at high concentration as a function of p for alkyl and aromatic acids. (d) r from the fitting of Eq.3.7 at 5 mM as a function of apparent distribution coefficient (<math>p^*</math>) for aromatic acids. . . . . .</p>   | 89 |
| 3.7 | <p>The initial color intensity along droplet diameter and the images (a) and the limit of detection (LoD) (b) for benzoic acid. The droplets were formed by solution A containing BG at the concentration of 0.02 g/ml, 0.002 g/ml and 0.0004 g/ml. Scale bar: <math>25 \mu m</math>. Here the distance of 0 means the edge of the droplets. . . . . .</p>  | 91 |

|     |  |    |
|-----|--|----|
| 3.8 | Error function fitting (dotted line) of the fluorescence intensity that increases from time 0 at the dye concentration of $5 \times 10^5 g/L$ (a) and $1 \times 10^4 g/L$ (b). . . . .   | 92 |
| 3.9 | The plot of droplet decolor time as a function of droplet size after injecting oil containing 100 mM of PHBA and benzoic acid (a), 1 mM of n-butyric acid and gallic acid (b) and 0.5 mM of acetic acid (c). The solid line is fitted from Eq.3.3. The dash line is fitted from Eq.3.7. . . . .  | 93 |
| 4.1 | Brief sketch of the fluid chamber (a) and surface nanodroplets formation and reaction in the fabrication of nanocaps of iron oleate (b). Solution A: ternary solution of ethanol, water and oleic acid. Solution B: water. Solution C: precursor solution. (c) and (d) are ternary phase diagrams of ethanol, water and oil mixtures and the enlarge images of the ouzo region. Here, the red lines represent oleic acid. While gray lines represent decane (a) and 1-octanol (b), respectively. The blue lines represent the dilution path during the solvent exchange process as the dilution path penetrates the solubility line of the oil. oil droplets form due to the over-saturation.[66] Ternary diagram of oleic acid is reproduced from [Li et al. J. Phys. Chem. C. 125, 28, 2021, 15324–15334.]. Copyright [2021] American Chemical Society. Ternary diagram of 1-Octanol is reproduced from [Arce et al. J. Chem. Eng. Data. 39 (2), 1994, 378-380.]. Copyright [1994] American Chemical Society. Ternary diagram of decane is reproduced from the IUPAC-NIST solubility database. . . . . | 99 |

|     |   |     |
|-----|---|-----|
| 4.2 | (a) Optical images of surface nanodroplets during the reaction at 0 s, 14 s, 36 s and 193 s. (b) Iron oxide nanocaps on the substrate. (c) Morphology of the nanocaps obtained by AFM after heating at 500°C for 2 hours in air. (d) The height profiles of the nanocaps from AFM reveal that the contact angle of the nanocaps around 7°. Length of scale bare: 20 $\mu m$ in (a) and 50 $\mu m$ in (b). . . . .   | 103 |
| 4.3 | Images of three nanocaps milled by focused ion beam at diameter of (a) 4.5 $\mu m$ , (b)7.8 $\mu m$ and (c) 16.1 $\mu m$ . The images on the left were taken at 57° from the normal plan to the substrate. Length of the scale bar: 1 $\mu m$ . . . . .   | 104 |
| 4.4 | XPS spectra of the surface droplets after various heating process. (a) Iron <i>Fe2p</i> spectra (b) Oxygen <i>O1s</i> spectra (c) Carbon <i>C1s</i> spectra. Black solid line is cumulative observed values of binding energy for each element.Filled area under different colours denotes decovoluted peaks during peak fittings. (d) Optical images of nanocaps after different heating process. Treatment conditinos I-V are listed in Table 4.1. Length of scale bar: 15 $\mu m$ . . . . .                          | 107 |
| 4.5 | (a) TEM images of nanocaps heated at 500° for 2 hrs. (b) The corresponding selected-area electron beam diffraction (SAED) pattern image together with its simulation. (c) The high-resolution TEM (HRTEM) image of (a). (d) HRTEM of a higher magnification for the area indicated by a square in (c) and the simulation of the HRTEM image illustrated by a rectangle inset with white profile. The lattice-spacings belong to $\{10\bar{1}1\}$ (d-spacing 0.42 nm) and $\{1\bar{1}02\}$ (d-spacing 0.37 nm) . . . . . | 111 |

|      |  |     |
|------|--|-----|
| 4.6  | Surface and inner structures of iron oxide nanocaps fabricated from binary surface nanodroplets. (a) shows the creviced surface of the nanocap from oleic acid-octanol binary surface droplets. (b) The FIB-milled nanocap was fabricated from oleic acid-octanol binary surface droplets. (c) shows the inner structure of (b), indicating that the height of the nanocap increases toward to the center. (d) The rough but uncracked surface of the nanocap from pure oleic acid droplets. (e) and (g) show the inner structure of the nanocap synthesized from oleic acid-decane binary surface droplets (f), similar to the shape of (c). (h) High resolution images of the porous structure of the nanocaps synthesized from oleic acid-octanol binary surface droplets and oleic acid-decane binary surface droplets, respectively. (i) The sketch of the reaction process of binary surface nanodroplets with iron precursor. . . . . | 113 |
| 4.7  | Optical (first column) and SEM images (second and third columns) of nanocaps of copper oxide (a), yttrium oxide (b) and Zinc oxide (c). Length of scale bare: 25 $\mu m$ (first column), 15 $\mu m$ (second column) and 2 $\mu m$ (third column). . . . .  | 116 |
| 4.8  | (a) Sketch of the fluid chamber for photo-degradation test. (b) Optical images of non-porous nanocaps (No.1), moderately porous nanocaps (No.2) and highly porous nanocaps (No.3) on the glass slide. (c) The surface coverage of the nanocaps corresponding to (b). (d) Normalized efficiency of photodegradation by nanocaps. The efficiencies are normalized by dividing the net efficiency of ( $E_{cap}-E_{glass}$ ) by surface coverage (S). Length of scale bar in (b): 25 $\mu m$ (top row) and 15 $\mu m$ (bottom row).Error bars in (c) and (d) were obtained from 3 repeats of the experiment. . . . .  | 119 |
| 4.9  | Sketch of the milling process by FIB.. . . .   | 120 |
| 4.10 | The chemical structure of the methyl orange and the degradation path.  | 120 |

|      |  |     |
|------|--|-----|
| 4.11 | Optical images of surface oleic acid nanodroplets(a) and the iron oxide nanocap after heating at 500°C (b). Probability density function (PDF) of the surface droplets (c) and nanocap (d), corresponding to (a) and (b), respectively. (e) The surface coverage decreases after formation of nanocaps, indicating the significant mass loss during this process. Scale bar: 50 $\mu m$ . . . . .            | 121 |
| 4.12 | (a) and (b) are surface oleic acid droplets at larger size and intervals. (c) and (d) are the nanocaps after heating, corresponding to (a) and (b), respectively. . . . .  | 122 |
| 4.13 | Optical Images of nanocaps at high surface coverage (a) and low surface coverage (b), before and after 60 min sonication and (b) at 25 ml/hr, before and after 60 min sonication. White circles represent the broken nanocap after sonication. (c) The surface coverage of the nanocaps on the surface before and after 60 minutes sonication. Scale bar: 100 $\mu m$ .                                      | 123 |
| 4.14 | (a) The UV-vis spectra of the MO before and after degradation. The degradation efficiencies by using transparent cover glass and the cover glass with non-porous nanocap (No.1), moderately porous nanocap (No.2) and highly porous nanocap (No.3), respectively. . . . .  | 123 |
| 4.15 | (A) Low magnification TEM images of the nanocaps from acid-octanol binary droplets. The SAED pattern shown as an inset is high magnification TEM images of the nanocaps (B). The marked rings assigned to (01-12) and (10-14) of $\alpha - Fe_2O_3$ , respectively. (C) HRTEM image obtained from marked area in (B) displays a similar crystalline feature as the nanocaps from pure acid droplets. . . . . | 124 |

|      |  |     |
|------|--|-----|
| 4.16 | (A) Low magnification TEM images of the nanocaps from acid-decane binary droplets. The SAED pattern shown as an inset is high magnification TEM images of the nanocaps (B). The indexation on the SAED pattern suggests it be $\alpha - Fe_2O_3$ .(C)The HRTEM image obtained from marked area in (B) displays a similar crystalline feature as the nanocaps from pure acid droplets. . . . .  | 125 |
| 5.1  | Sketch of the solvent exchange process for formation of surface nanodroplets (a), formation of the silver nanoparticles around the surface droplet interface (b), and fabrication of the ordered silver nanoparicels ring (c). Sol.A: ternary solution of water,ethanol and VE. Sol.B: pure water. Sol.C (precursor solution): base solution of silver nitrate solution. (d) Sketch of SERS detection of R6G solution in a chamber by using ordered silver nanorings as substrate (left) or cover glass (right).   | 133 |
| 5.2  | (a) Optical images of surface VE nanodroplets in an array on a pre-patterned substrate. (b) Optical images (top row) and SEM images (bottom row) of the ordered ring of silver nanoparticles fabricated from surface nanodroplets. At 1) pH=10, silver nitrate concentration ( $C_{sn}$ )=0.1 mM, 2) pH=10, silver nitrate concentration ( $C_{sn}$ )=0.5 mM, 3) pH=9, silver nitrate concentration ( $C_{sn}$ )=0.5 mM and 4) pH=11, silver nitrate concentration ( $C_{sn}$ )=0.5 mM. (c) Average size of the silver nanoparticles at reaction conditions corresponding to b. (d) EDX result indicated the formation of silver. The scale bar is 50 $\mu m$ for (a), 5 $\mu m$ for top row of (b) and 1 $\mu m$ for bottom row of (b). . . . . | 137 |
| 5.3  | Raman spectra of R6G at the LoD of different substrates ( $10^{-7}M$ for sample 1 and 3, $10^{-8}M$ for sample 2). . . . .   | 138 |

|     |  |     |
|-----|--|-----|
| 5.4 | Surface enhancement Raman spectra of R6G at different concentrations by using 50x lens (a) and 5x lens (d). Three repeats in the experiments at the LoD by using 50x lens (b) and 5x lens (e) demonstrate high reproducibility. The correlation of R6G concentration and the peak intensity of $1508\text{ cm}^{-1}$ in lg-lg plot show linear relation by using 50x lens (c) and 5x lens (f). Error bars are from 3 repeats of the experiment to ensure the reproducibility. . . . .                  | 140 |
| 5.5 | (a) and (d) are the surface enhancement Raman spectra of the R6G at different concentrations by using 50x lens and 5x lens, respectively. Three repeats in the experiments at the LoD by using 50x lens (b) and 5x lens (e) demonstrate a good reproducibility. (d) and (f) are the linear correlation of the concentration of R6G and the peak intensity at $1508\text{ cm}^{-1}$ in lg-lg plot, respectively. Error bars are from 3 repeats of the experiment to ensure the reproducibility. . . . . | 142 |

# List of Symbols

## Latin

$Ar$  Archimedes number

$C$  Concentration

$c$  Solubility

$D$  Diffusion constant

$DLLME$  Dispersive liquid-liquid microextraction

$E$  Efficiency

$K$  Dissociation constant

$LogP$  Partition coefficient

$p$  Distribution coefficient

$Pe$  Peclet number

$r$  Reaction rate or dissociation rate

$SDME$  Single-droplet microextraction

## Greek

$\beta$  Mass transfer coefficient

$\gamma$  Interfacial tension

$\lambda$  Diffusion layer thickness

|          |                                 |
|----------|---------------------------------|
| $\rho$   | Density                         |
| $\tau$   | Duration of the over-saturation |
| $\theta$ | Contact angle                   |

# Chapter 1

## Introduction

Micro-sized and even smaller droplets are important in emulsion, lab-on-chip devices, micro-reactor, chemical sensing, materials synthesis and among many others, as shown in Figure 1.1.[1–7] The microdroplets have large surface area to volume ratios. Here the surface area to volume ratio ( $s$ ) can be defined as  $S/V$ .  $S$  is the surface area of the droplets and  $V$  is the volume of the droplets. Recently, attention has been drawn to the significantly enhanced reaction rate of the microdroplets.

### 1.1 Extraction, reaction and nanomaterial fabrication of microdroplets

#### 1.1.1 Microdroplets for chemical extraction enhancement

Liquid-liquid extraction has been widely applied in chemical extraction and detection. The principle of liquid-liquid extraction is based on the solubility difference of the target analyte between sample solution and extractant. For example,  $C_2Cl_4$  is widely used to extract polycyclic aromatic hydrocarbons (PAHs) from water due

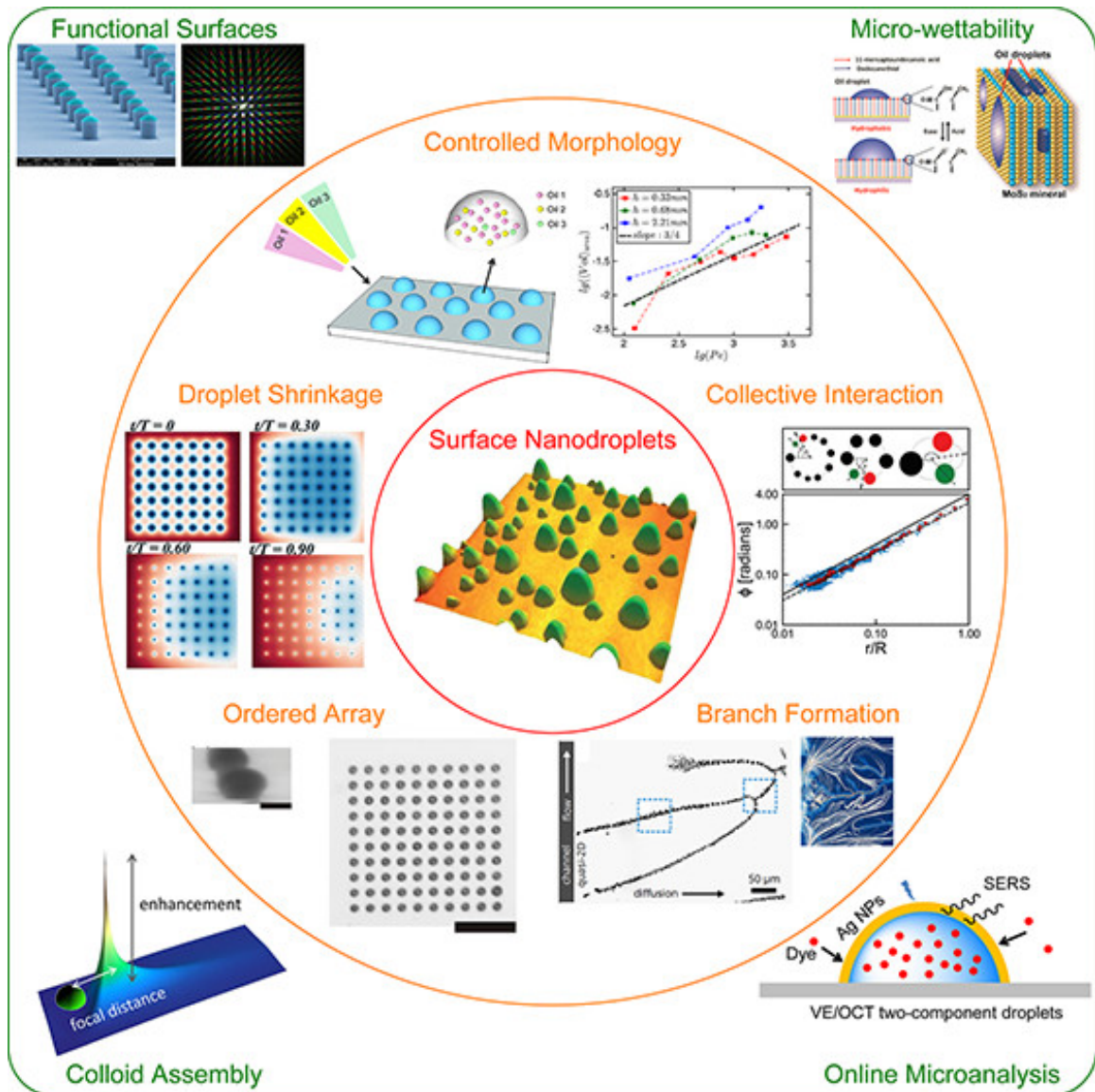


Figure 1.1: Applications of micro-scale droplets on solid substrate. (With permissions from Ref.[7]. Copyright (2019) American Physical Society.)

to the much higher solubility of PAHs in  $C_2Cl_4$  than in water[8]. Noticeably, the sample solution should be immiscible with the extractant. The main drawbacks of the traditional liquid-liquid extraction are time-consuming because of the excessive processes of shaking, heating, centrifugation and filtration [9–14].

Researchers have tried to increase the extraction efficiency by enhancing the mass transfer. Thus, microdroplets have been applied in liquid-liquid extraction to improve the extraction efficiency due to the large surface area to volume ratio, as shown in Figure 1.1. Two common microdroplet-based liquid-liquid extractions are used, including single-droplet microextraction (SDME) and dispersive liquid-liquid microextraction (DLLME).

#### **a. Single-droplet microextraction (SDME)**

Single-droplet microextraction is an approach that uses a single droplet at a volume of 1-10  $\mu L$  to extract target analytes from sample solution liquid[15]. A syringe with a fine tip was used to control the droplet volume and hold the droplet during the extraction process. To achieve high-efficiency extraction, the extractant liquid microdroplet was fully immersed into the sample solution, realizing a completed interaction between two liquids, as shown in Figure 1.2 right. Noticeably, the extraction liquid should be immiscible with the sample solution. This method is also named as direct immersion SDME (direct-SDME)[16, 17]. By using direct-SDME, researchers achieved four orders of magnitude higher extraction rate of paraben and phthalate than the conventional liquid-liquid extraction[18, 19].

When extracting a volatile or semi-volatile analyte, it is unnecessary to immerse the extractant droplet inside the sample liquid. A more clean-up method named head space SDME (HS-SDME) has been explicitly applied to this situation. In HS-SDME, the droplet also was controlled and stabilized by a syringe with a fine tip. However,

the droplet is suspended on the top of the vial without contacting the sample liquid, as shown in Figure 1.2 left. The volatile analyte is evaporated from the sample solution and captured by the extractant droplet[20]. Generally, heating is used to enhance the evaporation rate of the analyte and thus enhance the extraction efficiency[20]. By using HS-SDME, the sensitivity of the detection of terpenes can be enhanced up to 200 times of the traditional liquid-liquid extraction method[21].

Due to the limitation of the syringe precision, SDME can not form droplets with a size less than  $1 \mu L$ . Since the mass transfer rate of the liquid-liquid extraction is inversely proportional to the droplet size, it has been proposed that the efficiency of the liquid-liquid extraction can be further improved by using smaller droplets. A novel self-emulsification method named dispersive liquid-liquid microextraction has been invented to achieve more efficient extraction by using dispersive microdroplets in bulk liquid[8].

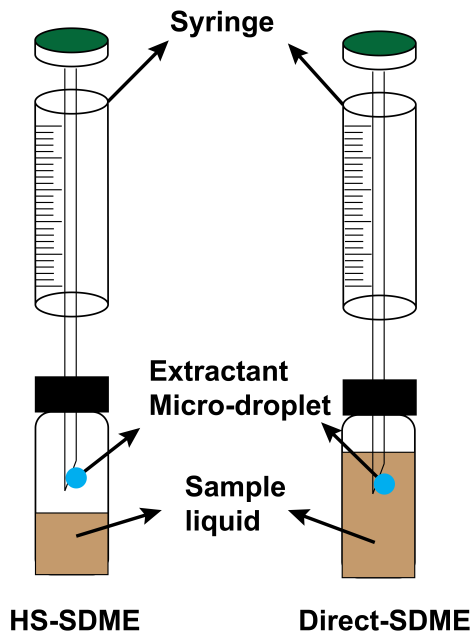


Figure 1.2: General sketch of the single-drop microextraction: Direct-SDME (right) and HS-SDME (left).

## **b. Dispersive liquid–liquid microextraction (DLLME)**

The process of the DLLME is sketched in Figure 1.3. If the sample solution is aqueous, the extractant needs to be a water-insoluble phase. When a mixture of extractant liquid and disperse solvent is injected into the aqueous phase, the extractant liquid spontaneously forms microdroplets and disperses in the sample solution due to the existence of the disperse solvent[22]. Generally, the disperse solvent is the co-solvent of extractant and sample solution. Those dispersed extractant microdroplets can exist for a few to tens of minutes and enable a high recovery rate. After the extraction process, centrifugation is applied to separate sample liquid and extractant liquid. Then the extractant liquid containing extracted analyte was taken out for analysis by using analytical instruments, including GC-MS[23], HPLC[24], UV-vis[25] and among other analytical instruments.

In DLLME, the disperse solvent is a co-solvent of sample solution and extractant liquid. Thus, the self-emulsification process is also known as Ouzo effect[26]. The principle of Ouzo effect emulsification is that when a poor solvent is added into a mixture of good solvent and co-solvent, the miscibility reduces sharply, leading to an oversaturation of good solvent and thus nucleation of the good solvent microdroplets. The detail of the Ouzo effect will be explained in the following section (section 1.3). The Ouzo effect can form the droplets with the volume of femtoliter and even a smaller scale[26], enabling a much faster mass transfer rate than other methods. Compared to SDME, DLLME have less time consumption. Most of the DLLME process can be finished within one minute[15]. According to two recent review articles, 40 chemicals in the analysis of forensic toxicity and 89 of pesticides and pharmaceuticals have been extracted by this method[27, 28].

The advantages of the DLLME are small consumption of extraction solvent, short time of extraction process and high enrichment factor. However, a downside of the method is that it is difficult to avoid toxic extracting solvents (e.g. carbon tetra-

chloride) or a large amount of harmful dispersive solvents (e.g. methanol). Next, DLLME requires the consumption of relatively large volumes (i.e. mL) of disperser solvents, which usually decreases the partition coefficient of analytes into the extracting solvent. The technique is also time and reagent-consuming requires dedicated instruments for separation, i.e., it is expensive. Moreover, although the performance of DLLME in aqueous samples is excellent, it is not yet suitable in complex matrices such as biological samples. Therefore, the method urgently needs further improvements, miniaturization, and extensions, and the cost must be considerably reduced.

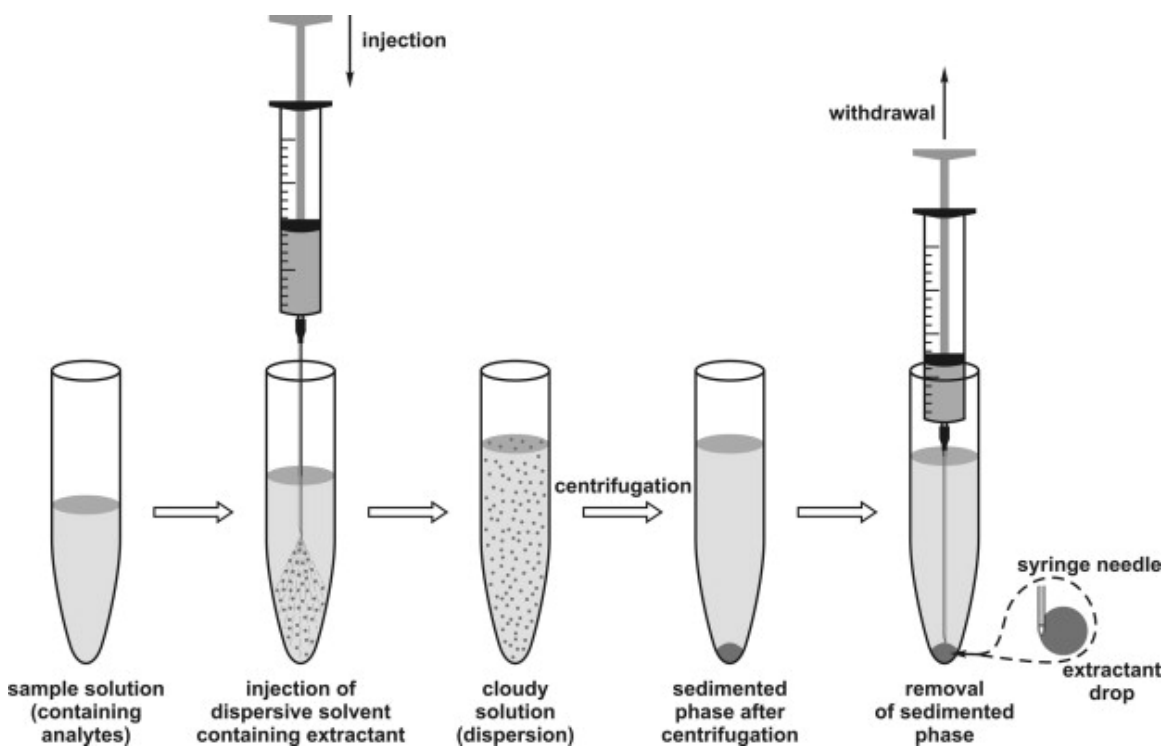


Figure 1.3: General sketch of the dispersive liquid-liquid microextraction procedure.

(With permissions from Ref.[22]. Copyright (2011) Elsevier Ltd.)

### 1.1.2 Microdroplets for chemical reaction acceleration

The reaction rate in microdroplets can be significantly enhanced.[29] Microdroplets can achieve even six orders of magnitude higher reaction rates compared to reactions that happened in the bulk surrounding.[30, 31] Meanwhile, microdroplets enable spontaneous reactions that would require catalyst when they happen in a bulk environment.[32] Such advantages of the chemical reaction enhancement in microdroplets attracted great research interest. Currently, five common methods are used to generate microdroplets for reaction acceleration, including reaction in sprays, microdroplet-microdroplet collision, microdroplet splashing on a substrate, individual levitated microdroplets and thin films. By using these methods, many reactions have been applied to achieve high output, including dehydration[33], Schiff base formation[34, 35], Oxidation of amine or sulfide[33] and among other reactions.

Currently, three hypotheses have been proposed, including the enthalpy effect, entropy effect and fast diffusion and mixing. The solvation state plays an essential role in the reaction rate constant in the enthalpy effect hypothesis.[36] When the reaction happens in the gas phase (no solvation state), the rate constant can be very high due to the low energy barrier, as shown in Figure 1.4a. In some cases, when the reaction happens in the bulk phase (full solvation state), the rate constant is around six magnitudes lower than the reaction in the gas phase, measured from the experimental results. Thus, researchers proposed this difference by a high energy barrier in the bulk phase due to a transition state formed during the reaction, as shown in Figure 1.4c. Wei et al.[29] attributed the acceleration of the reaction in microdroplets to the intermediate state of the solvation between the gas phase and bulk phase, as shown in Figure 1.4b. As partial solvation ions can be easily formed by microdroplets, due to the coulombic explosions, as studied by mass-spectrometry[37]. The partial solvation of the reactant in the microdroplet decreases the energy barrier for the reaction, leading to a higher reaction rate constant than the reaction in the bulk phase.

Another thermodynamic hypothesis is the entropy effect. Zhou et al. found an ordered orientation of the solute molecules at the surface of the droplets.[38] The ordered distribution of the molecules may have a lower entropy and higher energy at the initial state (before the reaction), leading to a lower energy barrier during the reaction than the bulk. Wei et al. attributed this ordered orientation of the molecules at the surface to electrostatic repulsion[29]. Further evidence to support this hypothesis is that the water is more like to form an ice structure at the interface of gas-phase or solid-phase than that in bulk due to the less polar of the water molecular at the interface[39]. However, if the droplet's inner volume is considered the same as the bulk phase, the total reaction enhancement should not be such noticeable since the interface region of the droplet is only a small volume of the whole droplet. Other researchers think that the fast mass transfer and mixing may be one of the main reasons for the reaction acceleration by microdroplets. Fallah-Araghi et al.[40] proposed a model of reaction-diffusion at the droplet interface based on Fick's law. They found that the reaction products at the interface could leave the surface region and then move inside the droplets. Furthermore, if the reaction is much faster at the interface, the concentration gradient of the reactant and products from the interface to the center of the droplet would be larger, leading to a more rapid diffusion. In addition, the flow of the external phases can attribute to turbulence inside of the droplet, leading to a faster diffusion and mixing[41].

In order to analyze the reaction process, some analytical instruments, including high-performance liquid chromatography (HPLC), ultraviolet-visible spectroscopy (UV-vis), nuclear magnetic resonance (NMR) and mass spectrometry (MS), were used to monitor the consumption of reactant and generation of the product during the reaction.[42–45] However, due to the short lifetime of the microdroplets, the current methods only focus on the reaction that happens in micro-second and even shorter time scale. Some other long-term reactions like reversible reactions and the very low concentration still remain research interest.

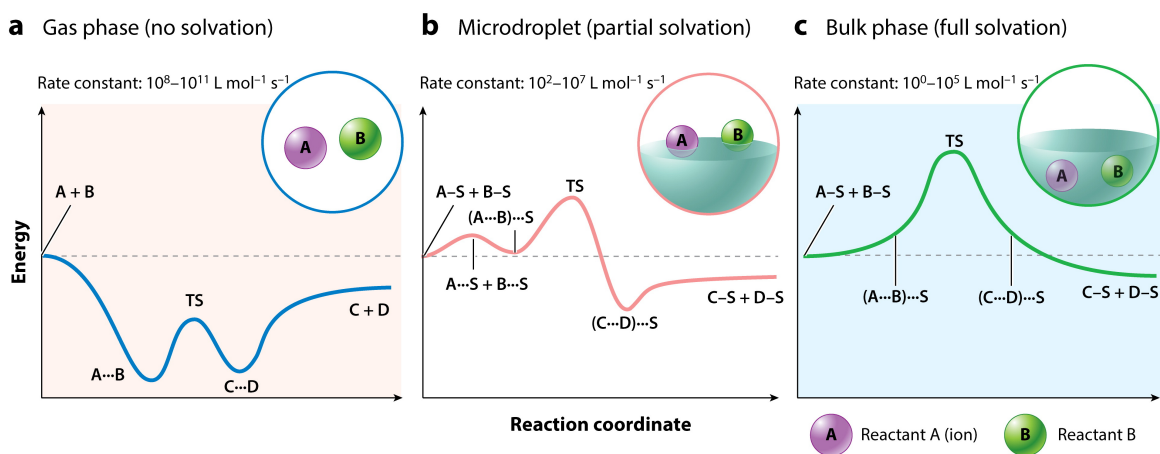


Figure 1.4: Dependence of the rate constants on reaction energy for the dilute gas phase (a), microdroplet interface (b), and bulk phase (c). A and B refer to two different reactants, S refers to solvent molecules, and C and D are two products. In order to make an analogy to gas-phase reactions, A is assumed to be the ionic form and B is neutral. A plus sign indicates that two particles are far from each other. An ellipsis indicates that the two particles are approaching but no bond is formed. A minus sign indicates bond formation. (With permissions from Ref.[29]. Copyright (2020) Annual Reviews.)

### 1.1.3 Microdroplets for materials synthesis

Many material syntheses are based on chemical reactions. As microdroplets have already shown good reaction enhancement, researchers proposed to use microdroplets in materials synthesis enhancement. The electrospray has been considered to replace the traditional redox reaction in materials synthesis. Li et al. formed gold and silver nanoparticles by using electrospray of gold and silver salts. The as-produced nanoparticles range from 2.2 nm to 6.5 nm and show an excellent catalytic reaction in reducing 4-nitrophenol. The rate constant of the catalytical reaction of the nanoparticles forming by electrospray is two magnitudes higher than the nanoparticles forming from traditional redox reaction[46]. By using different precursor solutions, the electrospray method can also be used to fabricate other nanoparticles.

The size and morphology of the materials fabricated by electrospray show a relatively large deviation due to the uncontrollable formation of the microdroplet during the spray process. Thus, micro-fluidic systems have been applied to generate microdroplets with a stable size and morphology[47, 48]. The convection flow inside and outside of the microdroplets in the micro-fluidic system can further enhance the mass transfer and reaction[47]. Ameloot et al. applied biphasic reaction and micro-fluidic system in the synthesis of metal-organic framework (MOF) hollow sphere structure. The products show a fixed size with  $375 \mu m$  in diameter and have been applied in the selection of small molecules[49]. Especially, thanks to the highly controllable process of the reaction, micro-fluidic systems have been used to fabricate Janus materials, which have areas with different physical or chemical proprieties in individual particle[47]. For example, Yu et al., by using the microfluidic system, fabricated titanium oxide and carbon black micro-spheres. When a patterned electric field was applied, the titanium oxide area showed a white color while carbon black showed black.[50] Such advantages of the materials synthesis by using microdroplets attracted thousands of researchers and have been applied to a broad range of materials. Not limited

to electrospray and micro-fluidic systems, different methods for microdroplet formation and different types of materials synthesis are still keeping developing.

## 1.2 Surface nanodroplets

The surface nanodroplets are the droplets immobilized on a solid substrate within an immiscible phase (usually another liquid phase). Here, the nano refers to the height of the droplets is ranging from tens to hundreds of nanometers. The base diameter of the droplet may range from hundreds of nanometers to tens of micrometers. Surface nanodroplets are spherical cap shape, as shown in Figure 1.5. The height of the droplet ( $H$ ) is the distance from the top of the droplet to the substrate.  $H$  may be larger or smaller than the sphere radius ( $R$ ) based on the contact angle ( $\theta$ ). Only when  $\theta = 90^\circ$ ,  $H$  and  $L/2$  (lateral radius) equal to  $R$ . Here,  $L$  refers to the lateral diameter. The contact angle is determined by Young's equation[51]:

$$\cos\theta = \frac{\gamma_{SL} - \gamma_{SD}}{\gamma_{LD}} \quad (1.1)$$

Here,  $\gamma$  is the interfacial tension. SL means the substrate-liquid interface. SD and LD are substrate-droplet interface and liquid-droplet interface, respectively. From Eq.1.1, the morphology of the surface droplet is determined by the properties of the liquid phase, droplet phase and the substrate. The diverse selections of these three phases make the surface droplet have multiple morphologies with different contact angles  $\theta$  and have broad application scopes.

The volume of the surface droplet ( $V$ ) can be calculated by the lateral diameter ( $L$ ), Height of the droplet  $H$  and the contact angle  $\theta$ . The relation can be written as:

$$V = \frac{\pi}{24}H(3L^2 + 4H^2) \quad (1.2)$$

As mentioned above, the surface nanodroplets are tens to hundreds of nanometers in height and hundreds of nanometers to tens of micrometers in lateral diameter. The

volume of the surface nanodroplets is calculated as femtoliter scale from Eq.1.2.

Thanks to the pinning of the droplets on the substrate, the surface nanodroplets show the advantage of a long lifetime. Compared to the microdroplets in bulk mentioned in previous sections, the surface nanodroplets facilitate long-time reactions, which can help to understand the reaction mechanism. The droplets in bulks are always keeping moving due to the Brownian movement. However, surface droplets are stabilized on the substrate, which allows in-situ and real-time research on the dynamic process of reaction, extraction and among other techniques.

Efforts have been made on the formation method of the surface nanodroplets, includ-

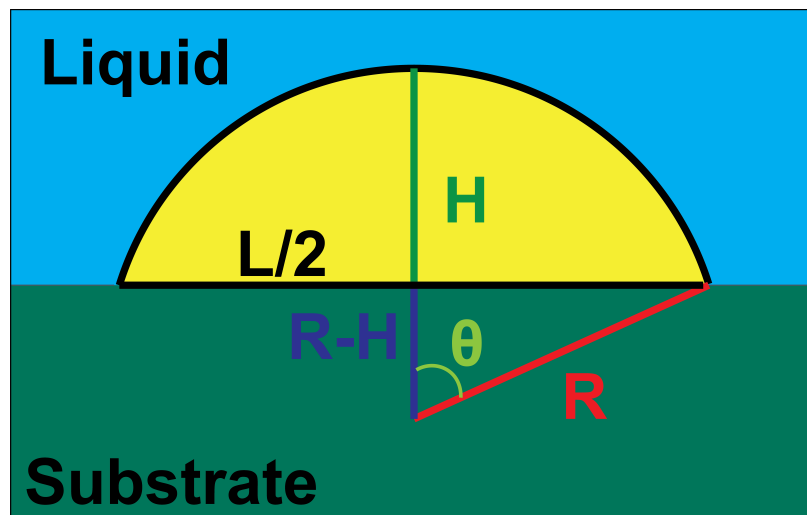


Figure 1.5: General sketch of the surface nanodroplets.

ing injecting printing[52, 53] nanodeposition[54, 55] and de-wetting of thin films[56, 57]. The inject printing method for the formation of surface droplets is the direct deposition of the droplets on a substrate by a fine tip[53]. The nanodeposition method is similar to inject printing but utilizes spray, especially electrospray, to deposit a large number of small droplets on the substrate surface[55]. As for the de-wetting of the thin films, when the substrate is exposed to an electron beam, the surface properties changes, leading to a difference in the wettability between the un-exposed area and the exposed area. Thus the water film leaves the hydrophobic area and accumulates

in the hydrophilic area, forming surface droplets on the substrate[57].

The methods mentioned above have unique advantages. For example, inject printing shows the benefits of flexibility in size and liquid types, low cost, and potential for automation. The de-wetting of the thin-film method is a highly controllable method in fabricating the surface droplet and can fabricate the droplets with the size down to a sub-micron scale. However, there are still some limitations of those methods due to the capillary force, external energy and others.

Limited by the capillary force, the inject printing method currently can only fabricate droplets with the size of tens micro-liter. The de-wetting of the thin film shows the potential to reach the femtoliter scale of the droplet. However, the current challenges include strict instrument requirements, low droplet aspect ratios, and low surface coverage. As for the nanodeposition, the deposited droplet shows a large deviation in the droplet sizes. Solvent exchange, inspired by the Ouzo effect, can overcome the drawbacks motioned above and show advantages in a highly controllable manner, low cost, convenience and flexibility in forming the surface droplet with a small volume (femtoliter or smaller).

### **1.3 Ouzo effect**

Ouzo is a very famous Greek alcoholic beverage which contains alcohol and anise oil. When water was added, the Ouzo mixture became cloudy due to the spontaneous formation of anise oil microdroplets. This phenomenon is named as Ouzo effect, also known as nanoprecipitation[58], solvent displacement process[59],spontaneous emulsification[60] or solvent shifting[61]. Recently, the Ouzo effect has been widely applied in many areas, not limiting in dispersed droplet formation, liquid-liquid extraction and nanomaterials synthesis.

The mechanism of the Ouzo effect is quite interesting. As oil and water are immiscible,

ethanol acts as a disperse liquid that is miscible with both oil and water, also known as co-solvent. When water is added to a mixture of oil and ethanol, the miscibility of the oil reduces sharply, leading to an oversaturation of the oil. This oversaturation provides the energy to overcome the barrier of nucleation. The as-nucleated oil droplets formed a depletion area near the droplets. In this depletion area, no more nucleation can happen, leading to a meta-stable phase of the oil droplets, as known as the Ouzo effect.[26] The Ouzo effect is low-cost and energy effective for droplets formation without the requirement for external energy, stirring or surfactants.

The ternary phase diagram in Figure 1.6 clearly shows the solubility equilibrium of water-oil-cosolvent system. Here, S represents the co-solvent of oil and water. The binodal curve is the equilibrium line (solubility line). The area above the binodal curve is one phase region, while the area below the binodal curve is the phase separation region. The Ouzo region is between the binodal curve and spinodal curve, as shown in Figure 1.6. The ouzo region is a metastable region where oil droplets can exist for a long time.

## **1.4 Formation of surface nanodroplets by solvent exchange**

Inspired by the Ouzo effect, Zhang et al. reported a simple and straightforward method to form surface nanodroplets on a hydrophobic substrate in a water surrounding[63]. The as-formed surface nanodroplets have the contact angle of  $10^\circ$ . This method is named solvent exchange. In the process, one solvent displaces another liquid in a chamber. With further investigation of the solvent exchange, this method has been demonstrated as a low-cost, environmentally friendly, simple, fast and highly controllable for the formation of diverse surface nanodroplets. Impor-

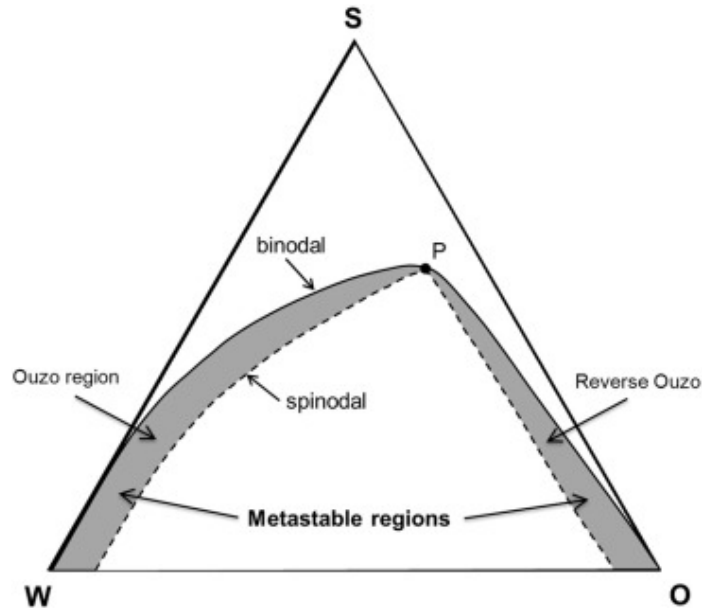


Figure 1.6: Sketch of the Ouzo region in ternary phase diagram. (With permissions from Ref.[62]. Copyright (2016) Elsevier Ltd.)

tantly, an approach (See Figure 1.7) is developed to convert surface nanodroplets of monomer to permanent surface microlenses via in-situ photopolymerization process. The approach decreases the difficulty of characterization and further demonstrates the volume of the surface nanodroplets with femtoliter volumes[64].

Typically, the solvent exchange is preformed in a narrow chamber, as shown in Figure 1.8. The fluid chamber firstly is filled with a good solvent of the oil (solution A) and then the good solvent is slowly replaced by a poor solvent of oil (solution B). During the replacement, oil microdroplets can be formed both in bulk and on the substrate surface due to the oversaturation of oil at the mixing front. However, compared to the bulk, the droplets on the solid surface have less surface area because of the spherical cap shape. Thus, the required energy for nucleation is less for surface droplets than for bulk droplets. In other words, droplets are more likely to be formed on the solid surface during nucleation. Several factors can impact the formation process of the surface nanodroplets by the solvent exchange, including flow conditions, solution

composition, and substrate properties.

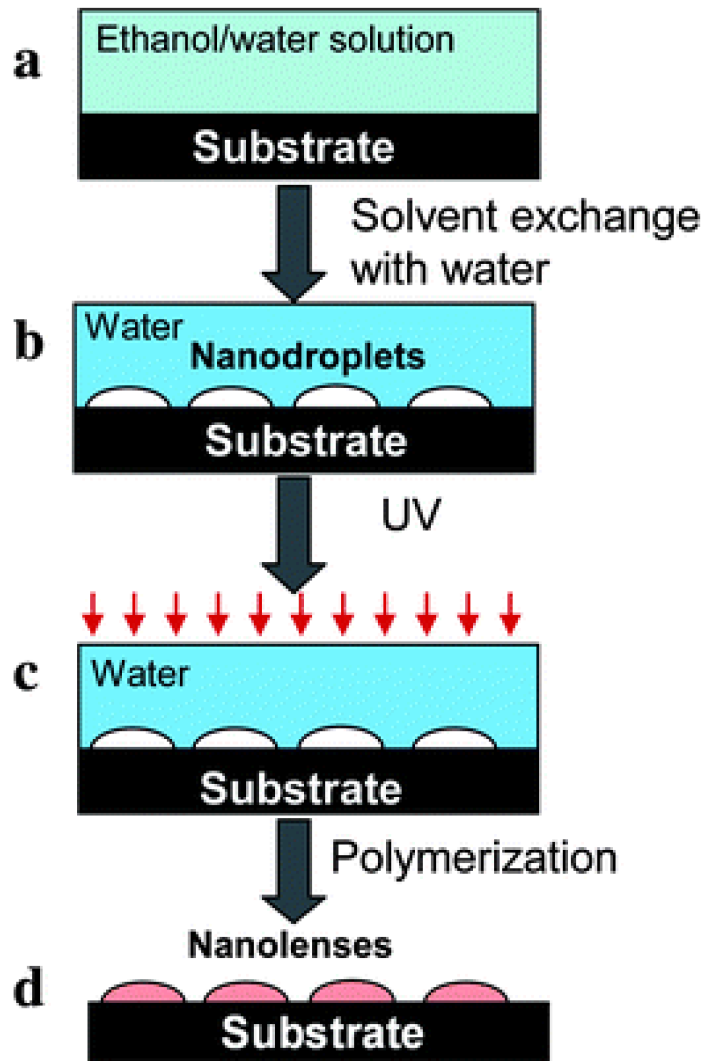


Figure 1.7: Sketch of the formation of permanent surface lens by surface nanodroplets.

(With permissions from Ref.[64]. Copyright (2012) Royal Society of Chemistry)

#### 1.4.1 Flow conditions for the solvent exchange

The flow condition plays an important role in forming surface nanodroplets. Zhang et al. found that the droplet volume increases with the flow rate and further investigated

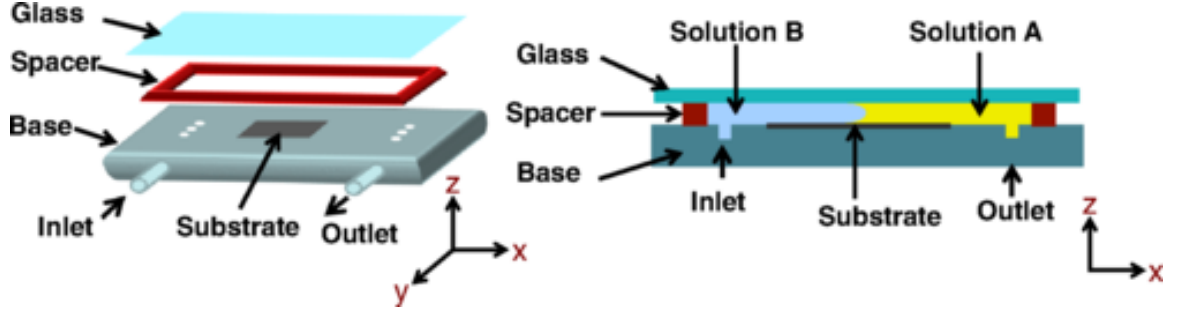


Figure 1.8: Sketch of the fluid chamber for solvent exchange process. (With permissions from Ref.[65]. Copyright (2015) American Physical Society).

the mechanism of heterogeneous nucleation and the following growth of the surface nanodroplets during the solvent exchange[66]. The over-saturation pulse at the mixing front of good solvent and poor solvent can be expressed as:

$$\zeta(t) = \frac{c_\infty}{c_s} - 1 \quad (1.3)$$

Here,  $\zeta(t)$  is the over-saturation level as a function of time,  $c_s$  is the solubility of the oil in the solution,  $c_\infty$  is the solubility of the oil at equilibrium state.

When the over-saturation front passes the substrate, the surface nanodroplets nucleate, grow and stop growth after the mixing front passes. The growing process of the droplet is based on the diffusive mass transfer of oil from the bulk to the droplet surface. As we know, the diffusion process is driven by the concentration gradient ( $\partial_r c|_R$ ). The growth model of the surface nanodroplets is assumed to be in a constant contact angle mode and then can be expressed as[66]:

$$\dot{m} = 4\pi\rho_{oil}R^2\dot{R} = 4\pi D_c R^2 \partial_r c|_R \quad (1.4)$$

$D_c$  is the diffusion constant.

The flow inside of the chamber is in a laminar region, the diffusion layer thickness ( $\lambda$ ) can be expressed as:  $\lambda \sim R/\sqrt{Pe}$ [67], due to the Prandtl–Blasius–Pohlhausen-type behavior. Here, Peclet number  $Pe$  is a dimensionless number expressed as:  $Pe = \frac{Q}{wD}$ .  $Q$  is the flux and  $w$  is the width of the chamber. Thus, the concentration gradient

can be rewritten as:

$$\partial_r c|_R \sim \frac{c_\infty - c_{s,wat}}{\lambda} \sim c_{s,wat} \frac{\zeta(t)}{\lambda} \sim c_{s,wat} \sqrt{Pe} R^{-1} \zeta(t) \quad (1.5)$$

After substituting Eq.1.5 to Eq.1.3, the growth process can be expressed as:

$$R\dot{R} \sim \frac{Dc_{s,wat}}{\rho_{oil}} \sqrt{Pe} \zeta(t) \quad (1.6)$$

The above equation is integrated from 0 to  $R_f$  and from 0 to  $t=\infty$ .  $\zeta(t)$  can be represented by  $\zeta_{max}\tau$ . Thus:

$$R_f \sim \left( \frac{Dc_{s,wat}}{\rho_{oil}} \zeta_{max}\tau \sqrt{Pe} \right)^{1/2} \quad (1.7)$$

Here,  $\tau$  is the duration of the over-saturation pulse passing a given location, that is, the time scale of the droplet growth. In the fluid chamber,  $\tau \sim h^2/D$ , due to the laminar flow.  $h$  is the channel height of the chamber. Thus, the final relation between droplet volume and flow condition ( $Pe$ ) can be written as:

$$Vol \sim R_f^3 \sim h^3 \left( \frac{c_{s,wat}}{\rho_{oil}} \right) \left( \frac{c_{s,eth}}{c_{s,wat}} - 1 \right) Pe^{3/4} \quad (1.8)$$

Eq.1.8 shows a good agreement with the experiment data, suggesting that the theoretical model is valid for the solvent exchange process.

The dynamic process of nanodroplet growth during the solvent exchange has been investigated by Dyett et al. by using total internal reflection fluorescence (TIRF) microscopy with a high temporal and spatial resolution[68]. TIRF enables monitoring of the growth of surface nanodroplets during the solvent exchange. The duration of the over-saturation ( $\tau$ ) is  $\sim Pe^{-1/2}$ , which can be described as the Taylor-Aris dispersion[69]. The over-saturation can be expressed as:

$$\zeta(t) = \zeta_{max} e^{-\frac{(t-t_0)^2}{2\tau^2}} \quad (1.9)$$

Thus, when substitute  $\zeta(t)$  to Eq.1.6 and apply error function, then the new expression is written as:

$$R(t)^2 \sim \frac{Dc_{s,wat}}{\rho_{oil}} \sqrt{Pe} \zeta_{max}\tau \text{Erf}\left(\frac{t-t_0}{\sqrt{2}\tau}\right) \quad (1.10)$$

Eq.1.10 can be further simplified by using  $\tau \sim Pe^{-1/2}$ .

$$R(t)^2 \sim h^2 \frac{C_{s,wat}}{\rho_{oil}} \sqrt{Pe} \text{Erf}\left(\frac{t-t_0}{\sqrt{2\tau}}\right) \quad (1.11)$$

Further integration of Eq.1.11 gives the dynamic volume of the droplet  $V(t)$ :

$$V(t) \sim (R(t))^3 \sim V_f(Pe) \left(\text{Erf}\left(\frac{t-t_0}{\sqrt{2\tau}}\right)\right)^{3/2} \quad (1.12)$$

In 2015, Yu et al. investigated the gravity effect on the formation of surface nanodroplets by tilting the angle of the substrate during the solvent exchange[70], as shown in Figure 1.9. They found that the centerline of the over-saturation pulse was shifted to the gravitational direction, leading to a longer growth time for the upper wall and shorter growth time for the lower wall. Archimedes number was applied to evaluate the gravity effect:

$$Ar = \frac{gh^3 \Delta\rho}{\nu \rho} \quad (1.13)$$

Here,  $\nu$  is the kinetic viscosity of the liquid.

When  $Ar$  is less than 1, the gravity effect can be neglected. To account for the gravity effect, they assumed the position of the shifted centerline of the over-saturation pulse (the maximum of the velocity) as  $\alpha$ . Thus, Eq.1.8 can be re-written as:

$$Vol \sim (1-\alpha)^3 h^3 \left(\frac{C_{s,wat}}{\rho_{oil}}\right)^{3/2} \left(\frac{C_{s,eth}}{C_{s,wat}} - 1\right)^{3/2} Pe^{3/4} \quad (1.14)$$

Eq.1.14 is helpful and can be used for the design of the channel height for the solvent exchange.

## 1.4.2 Geometry of the fluid chamber

The equations above show that the droplet volume depends on  $\sim h^3$ . Zhang et al. reported that the surface nanodroplets volume increases with the channel height[66]. In addition, stronger convection rolls in a deeper chamber lead to better mixing of the ethanol and water and thus larger droplets.

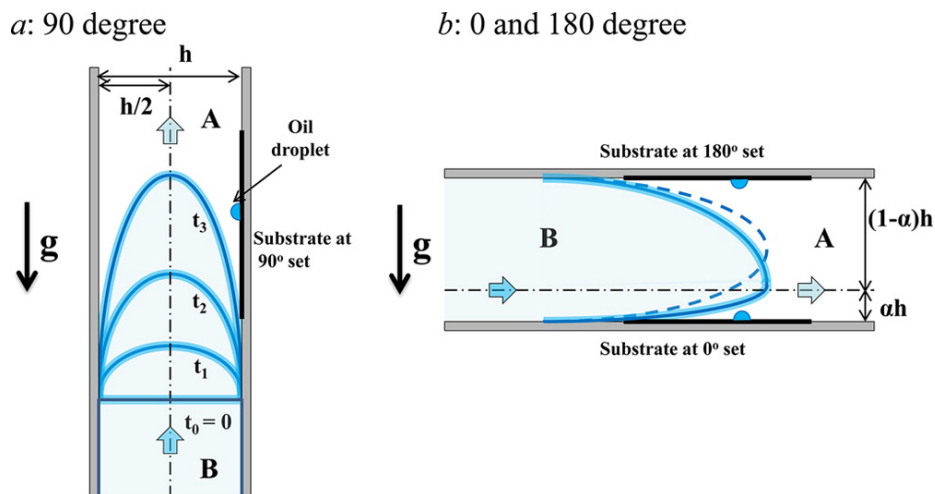


Figure 1.9: Sketch of solvent exchange process at different angles. (With permissions from Ref.[70]. Copyright (2015) American Chemical Society)

Yu et al. further investigated the influence of the channel height on the droplet formation by using a micro-structured channel with varied channel heights, as shown in Figure 1.10. Larger droplets were found at the gap with a larger channel height. Compared to the homogeneous chamber, the varied channel height leads to an enhancement of the droplet volume[66]. The author attributed the effects to the longer time  $\tau$  for droplet growth, asymmetric oil concentration in the gap, and the not fully developed flow due to the gap, respectively.

### 1.4.3 Effects from solution composition

In principle, the nucleation and growth of surface nanodroplets are based on the over-saturation of two solvents at the mixing front. Thus, the over-saturation level  $\zeta$  would be another factor to control the droplet formation during the solvent exchange.

Lu et al. investigated the influence of the solvent composition on the formation of water droplets[72, 73]. The solution composition during the solvent exchange is shown in Figure 1.11. Here,  $X_0$  is the initial composition of solution A (good solvent). While

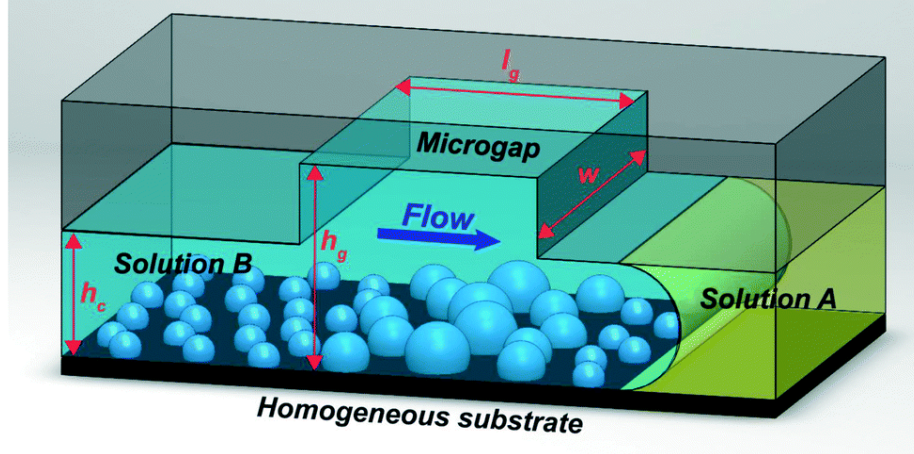


Figure 1.10: A sketch of the solvent exchange under the microchannel structure with the notations of the geometrical parameters.  $w$  is the lateral channel width,  $h_c$  is the channel height,  $h_g$  is the gap height, and  $l_g$  is the length of the gap. (With permissions from Ref.[71]. Copyright (2017) Royal Society of Chemistry)

$X_{end}$  is the final composition after the solvent exchange (poor solvent). Thus, the red line between  $X_0$  and  $X_{end}$  is the dilution path during the solvent exchange. When replacing solution A with solution B, the ratio of ethanol and water in the whole system is constant; thus, the red line is straight. The over-saturation happens when the dilution path contacts the equilibrium curve at the point of  $X_s$ . The integrated area between the dilution path and equilibrium curve thermodynamically represents the over-saturation level during the solvent exchange. Large areas indicate a significant over-saturation level, leading to a larger volume of the surface nanodroplets than small areas.

By applying the above thermodynamic explanation, a more precise expression of Eq.1.7 is:

$$R_f \approx \left( \frac{D}{\rho} P e^{1/2} \int_0^\infty c_s(t) \zeta(t) dt \right)^{1/2} \quad (1.15)$$

The droplet size is linear to the square root of the integrated area and shows good agreement with the experimental data, as shown in Figure 1.11d. Remarkably, when

the dilution path crosses the right part of the equilibrium curve, the above analysis is not valid because the dilution path goes over the ouzo region. A tie line has been applied to link the dilution path and Ouzo region, as shown in Figure 1.11c.

Recently, Li et al. formed the multi-component surface nanodroplets via the solvent exchange[74]. In this process, the oil phase in solution A is a mixture of two or three oils. Interestingly, the ratio of the oils in surface nanodroplets is not equal to their proportion in solution A, but is related to the over-saturation level of each oil. As different oils have different solubility curves in the water-ethanol-oil ternary diagram, at the same dilution path, the integrated area between the dilution path and the equilibrium curves are different, leading to differences in the over-saturation level. Li et al. calculated the integrated areas for each oil based on the ternary diagram. The ratio of the integrated area of different oils shows good agreement with the ratio of the oils that ended up in surface nanodroplets. As shown in Figure 1.12, the agreement indicates that the over-saturation principle is valid for a multi-component system.

#### **1.4.4 Effects of physicochemical properties of the substrate**

##### **a. Homogeneous substrate**

As mentioned before, the droplet volume increased with the increase of the flow rate[66]. Xu et al. found that the surface coverage of the droplet increases with the flow rate and then reaches a plateau[75]. The maximum surface coverage of the surface nanodroplets is between 35% to 50%, depending on the contact angle of the droplets. The author used the distribution function and Voronoi tessellation to analyze this phenomenon and then attributed this to the collective interaction effect of the surface nanodroplets and the coalescence during the nucleation and growth, as shown in Figure 1.13. The depleted area  $A$  increases linearly with the footprint area by the Voronoi tessellation model, indicating the diffusive driven growth of the

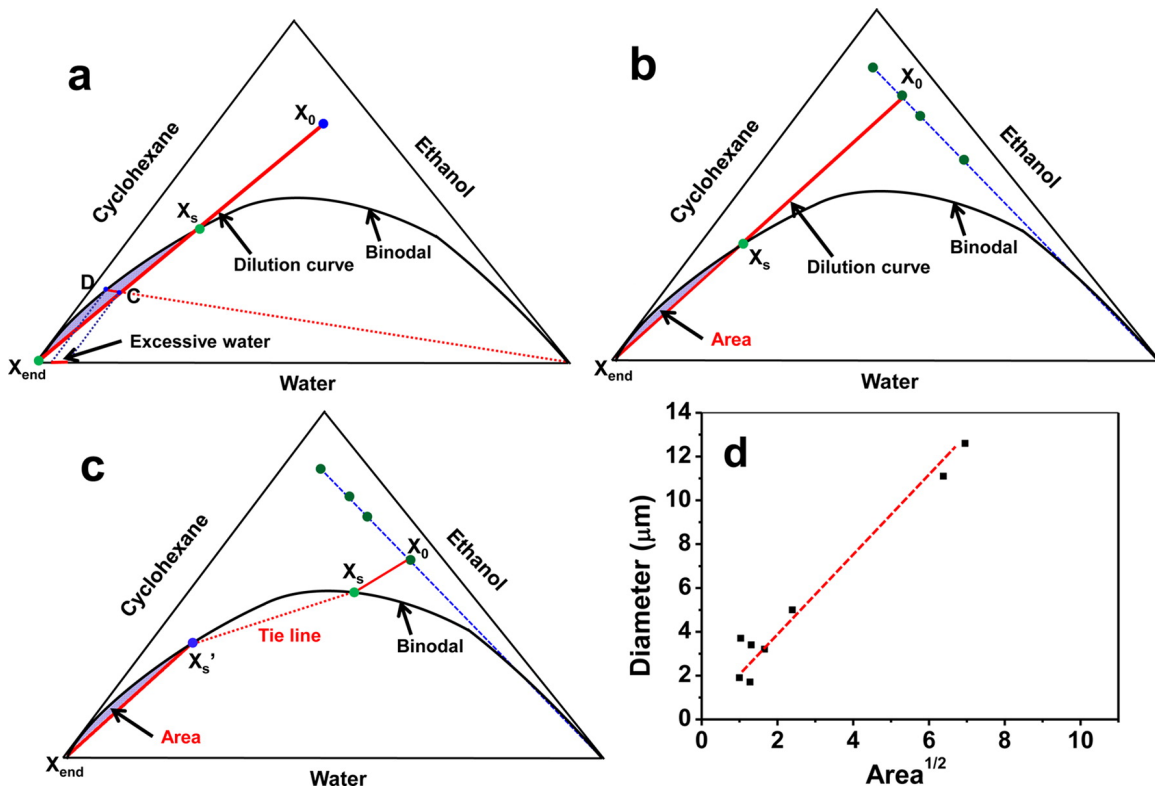


Figure 1.11: Sketch of the solution composition during the solvent exchange in a three-phase diagram. (a) The initial solution composition at  $X_0$  is undersaturated with water. The dilution curve is the red line, following which the solution becomes saturated at  $X_s$ . The temporary over-saturation level of water at point C is the projection of line CD on the water axis. (b) The overall over-saturation level is reflected by blue shaded area A. (c)  $X_s$  is above the Ouzo region. Macroscopic phase separation occurs along the tie line (dotted red line). The oil-rich sub-phase at  $X'_s$  contributes to droplet formation. (d) The droplet size increases almost linearly with  $A^{0.5}$ . (With permissions from Ref.[72]. Copyright (2016) American Chemical Society)

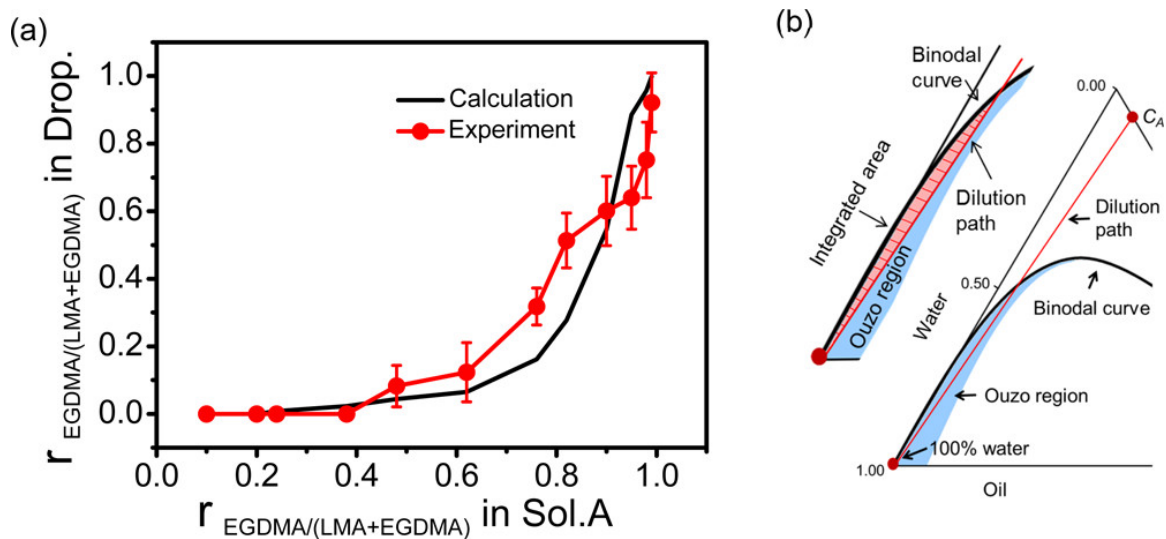


Figure 1.12: (a) Plots of binary droplet composition compared to the component ratio in solution A. (b) Sketch shows the calculation of the over-saturation level from the solubility phase diagram with a known oil-to-ethanol initial ratio. (With permissions from Ref.[74]. Copyright (2018) American Chemical Society)

droplet. The correlation between the droplet size and the footprint area is similar to that for surface nanobubbles.[76]

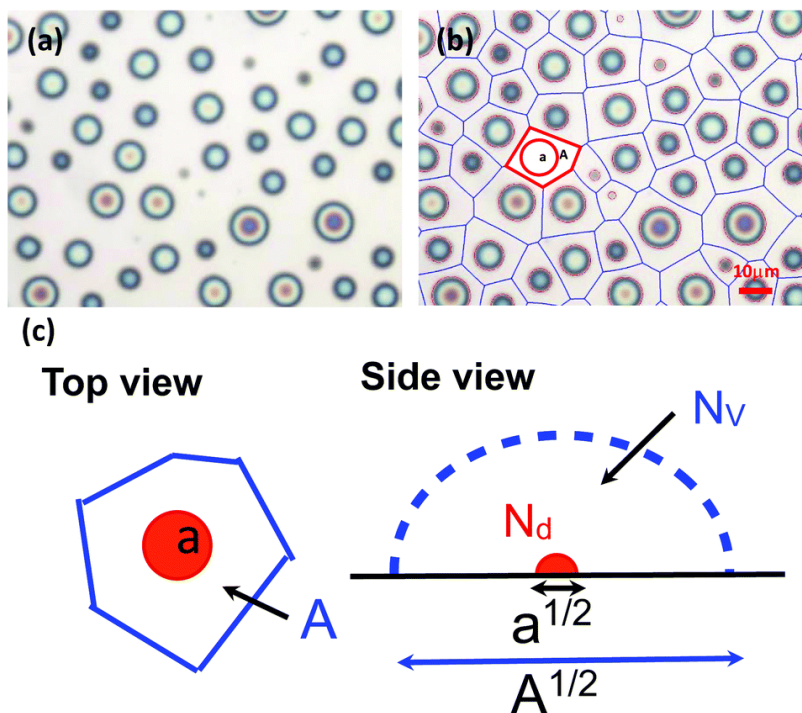


Figure 1.13: Representative optical image of polymerised nanodroplets (a), and the corresponding modified Voronoi tessellation (b), which is based on the distance between two the footprints of adjacent droplets. In (c) schematic top & side views.  $N_d$  is the number of molecules in the droplet, and  $N_V$  is the original number of molecules in the depleted volume around the droplet, which scales as  $\sim A^{3/2}$ . (With permissions from Ref.[75]. Copyright (2017) Royal Society of Chemistry)

## b. Chemically heterogeneous substrates

For the nucleation of surface nanodroplets during the solvent exchange, the existence of the substrate decreases the energy barrier for the nucleation. For forming oil

droplets, a hydrophobic substrate is usually needed, while a hydrophilic substrate is needed for forming water droplets. Bao et al. fabricated chemically pre-patterned substrate with hydrophobic micro-domains on a hydrophilic background[77]. By solvent exchange, the droplets formed selectively on the hydrophobic domains, as shown in Figure 1.14. Due to the pinning effect at the edge of the domain, a higher contact angle of the surface nanodroplets was found at a higher oil concentration in solution A. The ordered droplet arrays give the surface nanodroplets a border application potential, especially in optical fields.

Bao et al. further used the patterned substrate for studying the growth mode of surface nanodroplets[78], as sketched in Figure 1.15. The droplets grow at a constant contact angle (CA) mode at the initial state. When the based diameter of the droplet reaches the boundary of the patterned domain, further growth of the droplet follows the constant radius (CR) mode. Thus, the theoretical model of the droplet growth on a patterned substrate needs to be separated into two parts. When we look at an individual droplet, the Eq.1.6 can be re-written as:

$$R\dot{R} \sim \frac{D}{\rho_d}c(t)\sqrt{Pe}\zeta(t) \quad (1.16)$$

When assuming the competitive growth of the neighboring droplets and the vary early state ( $R=0$ ) can be neglected, after substituting and integration, the droplet growth function in CA mode can be written as:

$$L^2 \sim \frac{Dc_{s,0}}{\rho_d}\zeta_{max}Pe^{1/2}Erf(t_c(L, Pe)) \quad (1.17)$$

The following CR mode indicates that R is constant and contact angle  $\theta$  increases during the growth. Thus:

$$\frac{d\theta}{dt} = \frac{4D}{\rho_d L^2}(1 + \cos\theta)^2 f(\theta)c_s(t)\zeta(t) \quad (1.18)$$

By integration Eq.1.18 from initial contact angle  $\theta_c$  to final contact angle  $\theta_f$ , the droplet growth on patterned substrate under CA and CR mode can be determined.

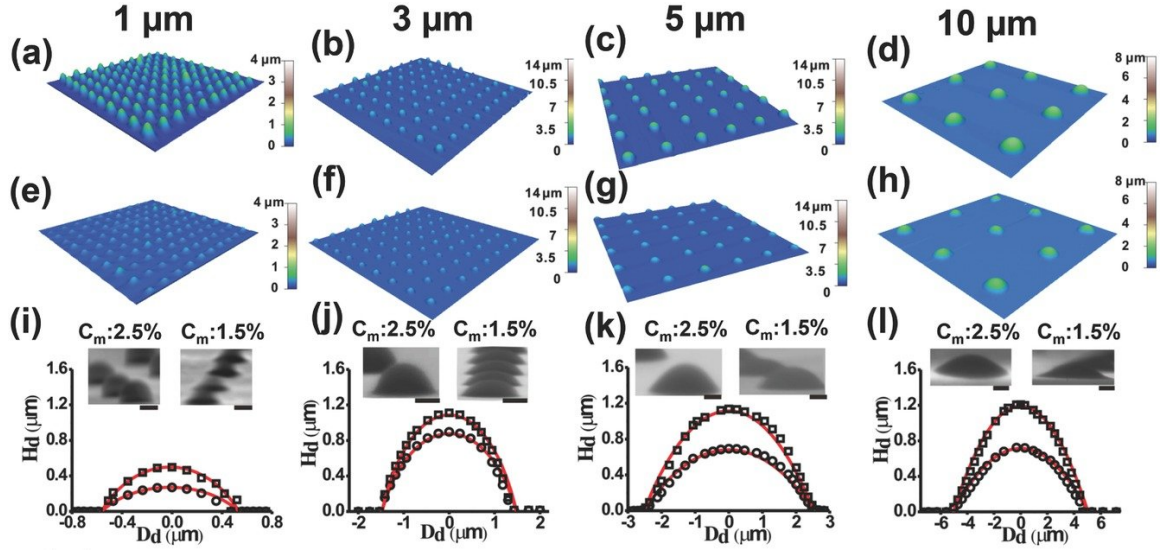


Figure 1.14: (a)–(l) Morphology and size of the polymerized droplets formed on pre-patterned hydrophobic substrates at five different oil concentrations  $C_m$ . (With permissions from Ref.[77].

### c. Micro-structured substrate

In 2015, Peng et al. firstly reported the formation of surface nanodroplets around a microcap[79]. Surface nanodroplets formed at the rim of the microcaps with a symmetrical arrangement in the position, size, and mutual distance, as shown in Figure 1.16d-i. Initially, a large number of small surface nanodroplets formed at the rim of the microcaps. At this stage, those droplets were similar in their size. During the later time, heterogeneous sizes of droplets were found. The number of the surface nanodroplets decreased with time due to the coalescence, leading to an increase in the individual droplet volume. In the end, only one surface nanodroplets remained on the side of the microcaps, as shown in Figure 1.16a,b.

Further research on the dynamic mechanism of this phenomenon of growing droplets was done by Dyett et al.[80]. The author used TIRF to in-situ monitor the coalescence process of the surface nanodroplets around the microcaps rim. The coalescence of the droplet happened in two neighboring droplets. The location of the merged droplet

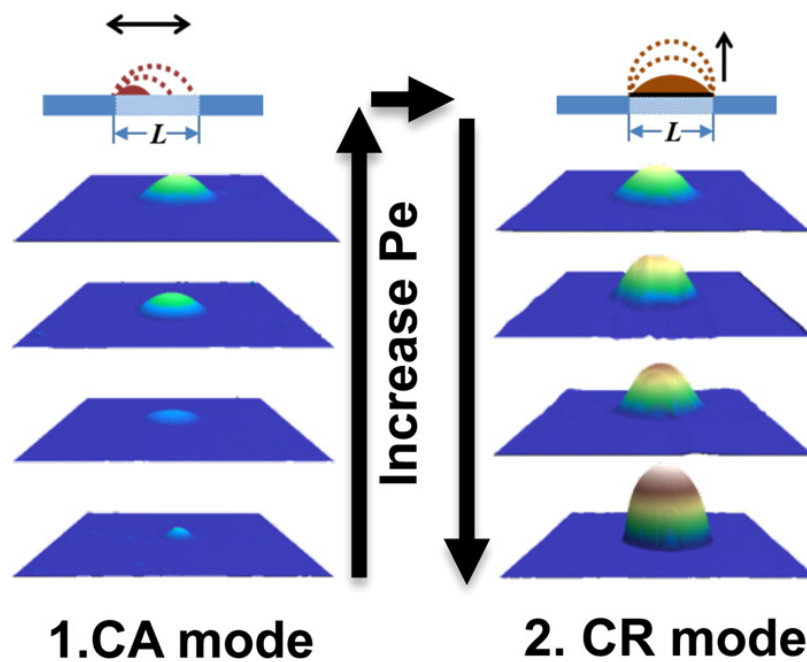


Figure 1.15: The sketch of droplet growth on patterned substrate under constant angle (CA) mode and constant radius (CR) mode. (With permissions from Ref.[78].

Copyright (2016) American Chemical Society)

was re-assigned and following a scaling law:  $\frac{\Delta\theta_1}{\Delta\theta_2} \approx (\frac{r_1}{r_2})^{-2}$ . Where  $r_1$  and  $r_2$  are the diameters of two droplets, respectively. While  $\Delta\theta_1$  and  $\Delta\theta_2$  are the angle differences between two un-merged (parent) droplets and the final position of the as-merged droplet, respectively. The scaling analysis suggested that the position of the merged droplet was mainly impacted by the larger parent droplet. A further dynamical model from the numerical analysis was established as :  $\Phi \sim r/R$ , as shown in Figure 1.16j,k. Here,  $\Phi = \frac{2\pi}{N}$ .  $R$  is the radius of the microcaps.

Yu et al. reported the formation of surface nanodroplets on the wall surface of a micro-fiber[81]. The surface now is not a plane but a curve. However, the surface nanodroplets can still be formed on the surface, as shown in Figure 1.17. Compared to the plane substrate, at the same condition, the droplet formation on a micro-fiber was significantly enhanced due to the local flow condition changed by the micro-fiber. Although the droplet size increased with flow rate, orientations of the fiber have a significant influence on growth dynamics.

#### **d. pH-responsive substrate**

Lu et al. reported the formation of surface oil nanodroplets on a pH-sensitive substrate via solvent exchange[82]. The gold substrate was coated with a monolayer of the binary mixture of 11-mercaptoundecanoic acid and dodecanethiol. This substrate is sensitive to the pH value, leading to a different surface wettability at different pH values, as shown in Figure 1.18. At different pH values, the contact angle varied. The  $MoS_2$  was used as the model sample with a 3D structure of different wettability. The contact angle of the droplets at  $MoS_2$  face and edge varied on the plane and on the edge due to the different wettability.

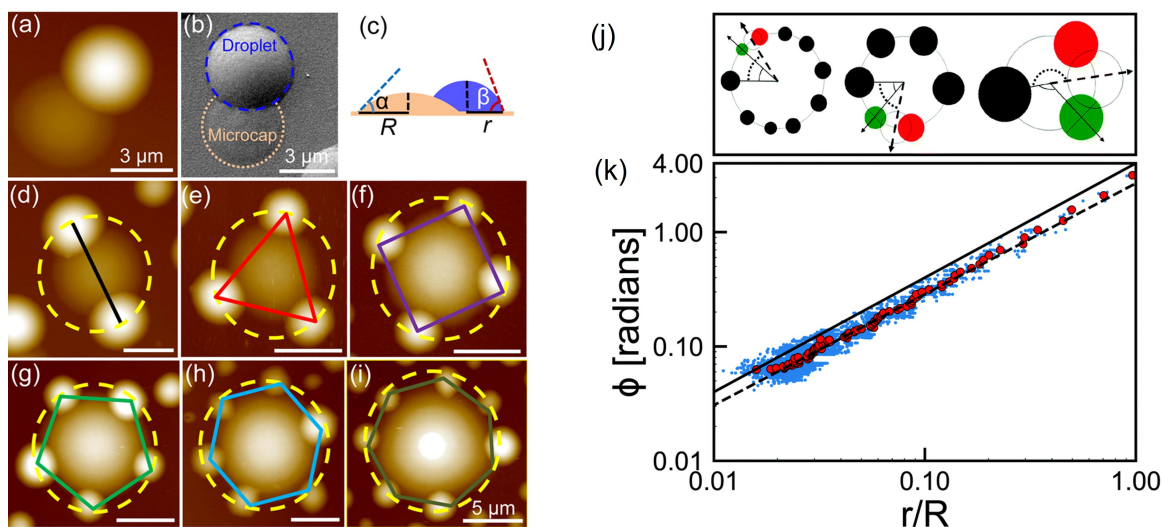
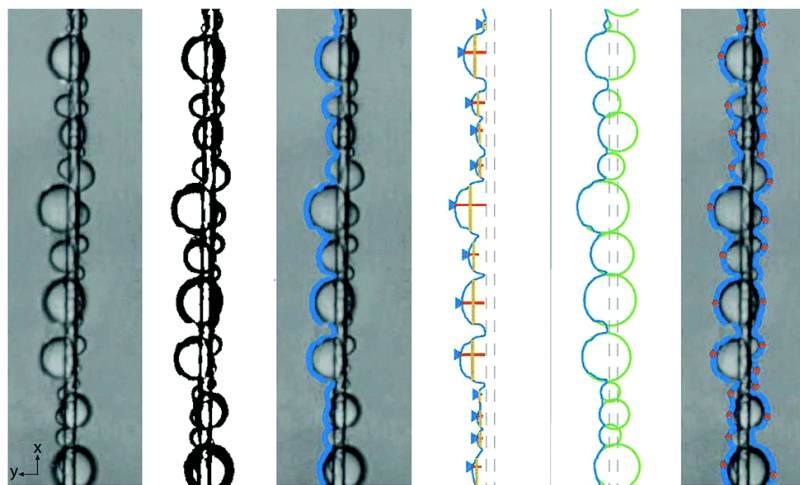


Figure 1.16: Spatial arrangement of the nanodroplets around the microcap. (a, b) AFM and SEM images of nanodroplets sitting on a microcap. (c) Notation of the nanodroplets and the microcap. (d–i) AFM images of multiple nanodroplets around one microcap with Symmetric N-gons from  $N=2-7$  (d–i). (j) Representation of the coalescence model when  $N = 9, 6, 3$ , respectively. The respective angles  $\Phi$  between the droplets before and after the coalescence process are also shown. (k) Angle  $\Phi$  (light blue line) and average angle  $\bar{\Phi}$  (red line) between droplets vs.  $r/R$  as revealed from the model. (Reproduced With permissions from Ref.[79]. Copyright (2015) American Chemical Society and Ref.[80]. Copyright (2018) Royal Society of Chemistry)

## (a) Imaging analysis process



## (b) Clam-shell shape

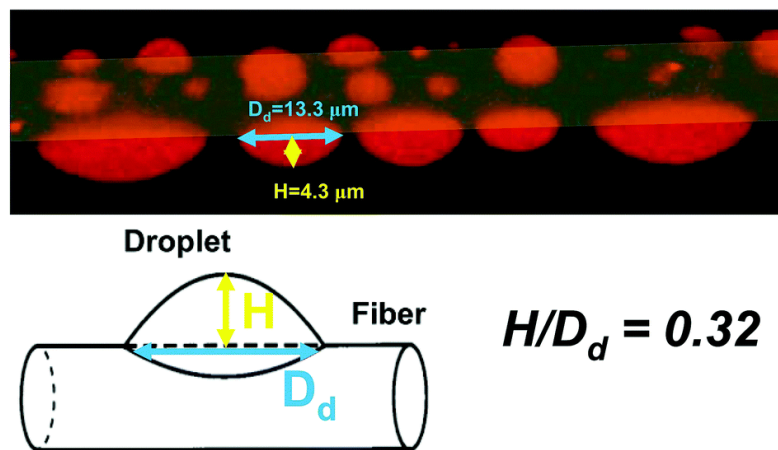


Figure 1.17: (a) Imaging analysis process by using Matlab software: 1. Image contrast enhancement and binarization; 2. edge detection; 3. surface droplet detection; 4. circle fit through all detected droplets. The mean diameter of droplets was obtained as the intersection of points between the fitted circles and the surface of the fiber. (b) Confocal microscopy image of surface droplets on the microfiber. The shape of the droplets (dyed in red) is that of a clam shell. The definition of the lateral diameter  $D_d$  and the height  $H$  is notated in the sketch. The ratio of  $H$  to  $D_d$  is about 0.32. (With permissions from Ref.[81]. Copyright (2018) Royal Society of Chemistry)

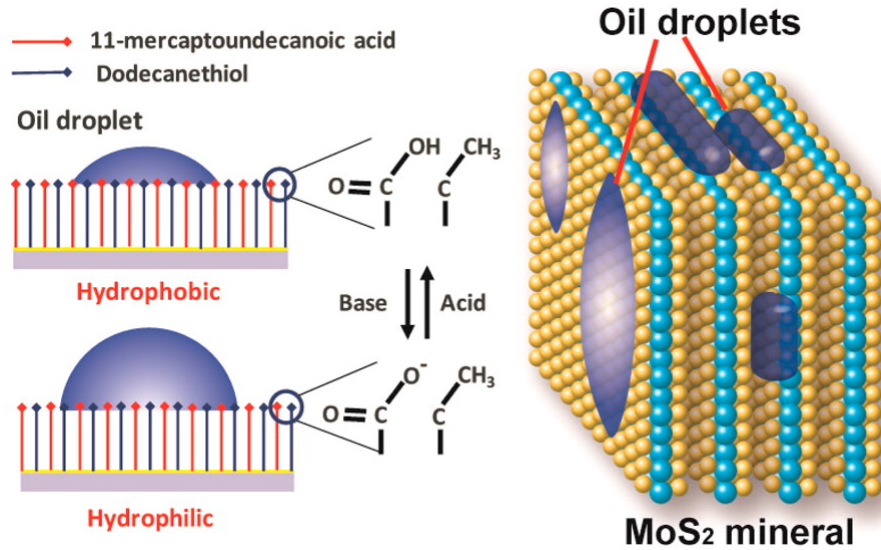


Figure 1.18: Sketch of the droplet formed on pH sensitive substrate and  $MoS_2$  sample. (With permissions from Ref.[82]. Copyright (2016) American Chemical Society)

## 1.5 Chemical reactions of surface nanodroplets

As surface nanodroplets can be stable on the surface, the reaction by surface nanodroplets can be detected easily without the influence of coalescence and movement. Li et al. investigated the mechanism of the biphasic reaction by surface nanodroplets[83, 84]. Oleic acid surface nanodroplets formed by solvent exchange and then reacted with NaOH solution. The droplets shrank during the reaction due to converting oleic acid to soap and then were removed from the droplet to bulk. The flow condition  $Pe$  and NaOH concentration were observed to affect the droplet shrinkage rate significantly. The scaling analysis gives the reaction:

$$t \sim Pe^{-3/2}(K_r c_{re,bulk})^{-1} \quad (1.19)$$

Here,  $t$  is the lifetime of the droplet (from the original state to disappear),  $K_r$  is the reaction constant and  $c_{re,bulk}$  is the NaOH concentration in water.

The follow-up work to investigate the size effect on the reaction rate showed that the reaction rate increased with the decrease in the droplet size[84]. The enhanced

reaction rate was independent of the surface coverage of the droplet and the flow rate of the external phase. A scaling analysis suggested  $\dot{R} \sim R^{-2}$ .

## 1.6 Applications of surface nanodroplets

Surface nanodroplets formed by solvent exchange exhibit the advantages of a long lifetime, excellent stability, flexibility and highly controllable formation. Those advantages make surface nanodroplets have broad applications, not limited to fundamental research in reaction kinetics, in-situ extraction and chemical sensing, materials synthesis and optical enhancement.

### 1.6.1 Surface nanodroplets for chemical sensing

Li et al. reported a method that combines surface nanodroplets for chemical extraction and surface enhancement Raman scattering (SERS) to achieve one-step high sensitivity chemical sensing[85], as sketched in Figure 1.19. Binary surface nanodroplets of vitamin E (VE) and octanol were formed by solvent exchange. Then silver precursor solution was injected to react with VE component, forming silver nanoparticles on the surface of the droplet. After the reaction, an aqueous solution with the target chemical was injected and the analyte was extracted into silver nanoparticles armored droplets. The Raman spectrometer was applied to analyze the extracted chemicals. The experiment results show that the limit of detection (LoD) for Rhodamine 6G (R6G) can be down to  $10^{-9}$  M with a quantitative analysis range of  $10^{-6}$  M to  $10^{-9}$  M. Compared to the traditional DLLME, this method can avoid multi-steps and the contaminations from the dispersive solvent.

The interface between two immiscible liquids can somehow act as a protective barrier. You et al. applied surface nanodroplets in the extraction of chemicals from a

suspension solution[86]. The surface nanodroplets were formed on the inner wall of a hydrophobized capillary tube with the total volume of the sub-milliliter scale. Then a simulated oil sand wastewater with Nile red (model compound) was injected. The narrow diameter of the capillary tube enables extraction with high efficiency. The detection of Nile red was evaluated by the fluorescence microscopy with LoD of  $10^{-8}$  M and also showed a good linear correlation of intensity and concentration from  $10^{-6}$  M to  $10^{-8}$  M. The low volume of the droplet liquid and feasibility in dirty suspension liquid make this method can be green, sustainable nanoextraction in severe environmental conditions.

Other works have been conducted to apply surface nanodroplets in chemical extraction and sensing, including the determination of partition coefficient[87] and encapsulated droplet the extraction enhancement[88]. The above examples demonstrate that the surface nanodroplets have broad application potential in this field.

### **1.6.2 Surface nanodroplets for optical enhancement**

Surface nanodroplets show a perfectly spherical shape without any defect due to the free phase of two immiscible liquids. The spherical shape shows good potential for optical enhancement. For example, Li et al. found that the fluorescence intensity in the encapsulated droplet is much higher than in bulk; even the bulk liquid is the same as the encapsulated droplet[88]. They attributed this phenomenon to the lens effect of the droplets that enhanced the intensity of the light.

Dyett et al. reported the focusing effect by the surface microlens[89]. Surface nanolenses were fabricated from in-situ polymerization of monomer nanodroplets. As shown in Figure 1.20A, when a surface lens was placed in the evanescent wave field, significant light intensity enhancement was observed compared to the area without the lens. The light intensity was enhanced by  $\sim 20$  times. The research further

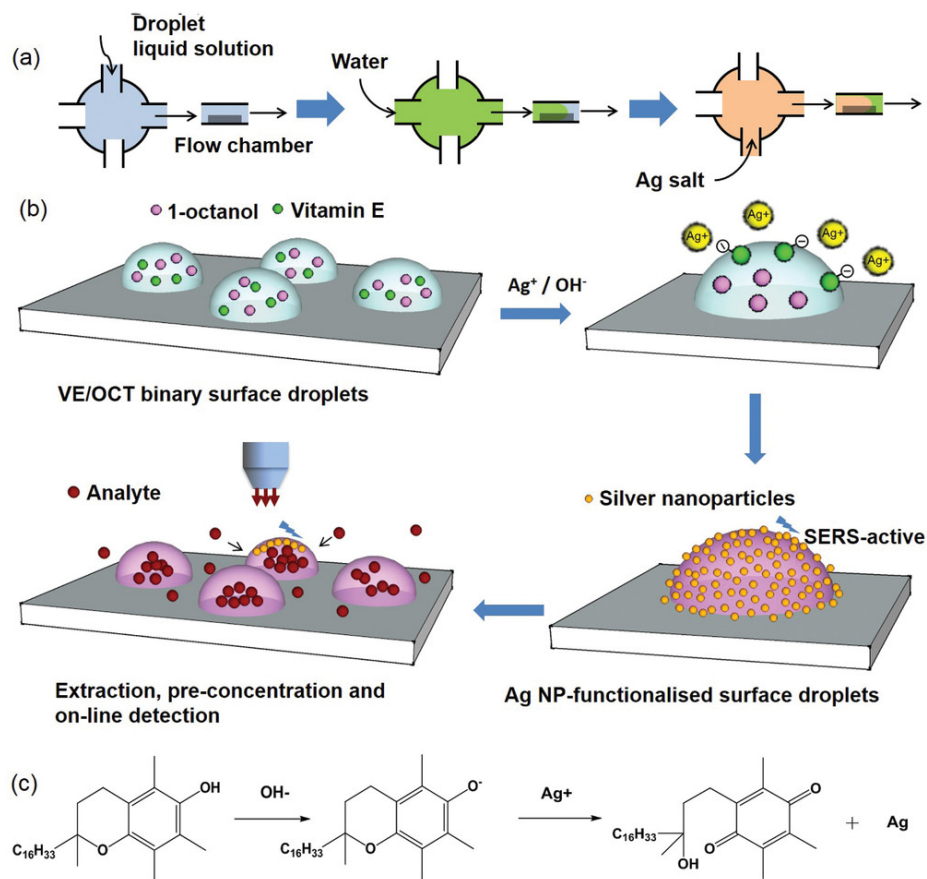


Figure 1.19: a) Sketch of the programmed flow sequence for the automation of formation of functionalised surface droplets. b) Schematic of the extraction, concentration, and in situ detection based on surface droplets. c) The reaction scheme of VE with  $\text{AgNO}_3$  to produce AgNPs. (With permissions from Ref.[85]. Copyright (2019) John Wiley and Sons)

showed that after being decorated with gold, the lens could generate plasmonic bubbles around the surface by laser illumination. The work demonstrated that the focusing effect of the light by the lens could lead to gas production at reduced power input, as shown in Figure 1.20C.

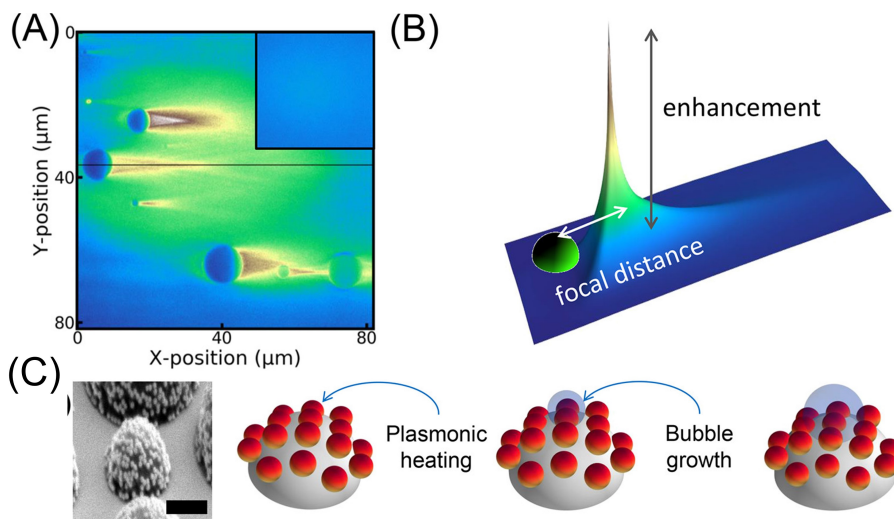


Figure 1.20: (A) TIRF image of microlens decorated substrate immersed in a 50% ethanol solution containing Nile red. Inset shows TIRF image of glass substrate immersed in a 50% ethanol solution containing Nile red. (B) 3D representation of a TIRF image for individual microlens. The height and color map are given by the recorded experimental intensity. The lens is an added schematic. The approximate focal length and enhancement are schematically depicted by the arrows. (C) Tilted SEM of a representative gold decorated microlens and schematic representation of the bubble growth via plasmonic heating. Scale bar = 1  $\mu m$ . (With permissions from Ref.[89]. Copyright (2018) American Chemical Society)

## 1.7 Thesis Objectives

Micro-sized droplets have practical implements in many areas. Surface nanodroplets are a specific type of micro-sized droplets immobilized on a solid surface. The advantages of the surface nanodroplets are long lifetime, stability, and others, which are desirable for the design of lab-on-chip devices, high-resolution near-field imaging, fast chemical sensing and many others. In recent research, the formation of the single component and multi-component surface nanodroplets has been well established.

As state-of-the-art when my Ph.D. study started in 2018, Li et al. applied surface nanodroplets in one-step ultra-sensitive chemical sensing by combining the nanoextraction and SERS[85]. Their study reported the formation of binary surface nanodroplets of VE and octanol, where VE component was a reactant for the formation of silver nanoparticles. The as-produced silver nanodroplets were distributed at the surface of the nanodroplets and acted as a SERS substrate. Then octanol, as an extractant, extracted the target chemical from the bulk. The extracted target chemicals were detected by SERS with super high sensitivity and a broad range of quantitative detection. Surface nanodroplets have the potential to further simplify the chemical detection process and even decrease the requirement for the instrument. Furthermore, the surface nanodroplets have been proposed to determine not a single compound from the bulk but diverse mixtures.

Therefore, based on this research foundation, the aim of this work is to understand the solvent exchange process for the formation of functional surface nanodroplets, to understand the extraction and reaction kinetics on a micro-scale and to broaden the application of the surface nanodroplets in chemical sensing and further broaden the applications of the surface nanodroplets. Furthermore, we expected that the surface nanodroplets could be used as a template for micro- or nano-structures fabrication. Thus, the specific objectives of this study were proposed as below.

1. To understand the process of functional (colored) surface nanodroplets formation

by solvent exchange and then apply them in distinguishing of mixtures with different acidic components.

2. To further understand (theoretically and experimentally) the coupled process of mass transfer and chemical reaction by using functional surface nanodroplets as a tool.
3. To develop the surface nanodroplets as a template for fabrication of surface-bound materials in a simple, cost-effective and green manner and then apply the as-produced materials in the photo-degradation area.
4. To further apply surface nanodroplets on the fabrication of metallic nano-structures and apply them in surface enhancement Raman scattering for chemical sensing.

## 1.8 Thesis Outline

Based on the motivation and aims of this PhD study, the research that has been conducted is outlined chapter by chapter.

### **Chapter 2. Integrated nanoextraction and colorimetric reactions in surface nanodroplets for combinative analysis**

*(Published paper: Wei, Z., Li, M., Zeng, H., & Zhang, X. (2020). Integrated nanoextraction and colorimetric reactions in surface nanodroplets for combinative analysis. Analytical Chemistry, 92(18), 12442-12450.)*

In this work, we formed surface aqueous nanodroplets containing pH indicator and then applied the droplet in combinative analysis of nanoextraction and colorimetric reactions for the determination of multicomponent mixtures. The acids from external phase were extracted into the droplet, leading to a color change of the droplet. The time scale of the droplet decoloration was based to evaluate the rate of extraction and reaction. We found that for acid mixtures, even they were in same pH value, the decolor times were specific for each mixture. We further apply this approach in

anti-counterfeiting of various alcoholic spirits by comparing decolor time of organic acid mixtures in the spirits.

### **Chapter 3. Interfacial partitioning enhances microextraction by multi-component nanodroplets**

*In press: Wei, Z., You, J., Zeng, H., & Zhang, X. Interfacial partitioning enhances microextraction by multicomponent nanodroplets. The Journal of Physical Chemistry C.)*

Sensitive and reliable in-droplet chemical analysis benefits from enhanced partition of an analyte into the droplets. In this work, we will show that chemical reactions in surface nanodroplets can shift the partition of acid analytes from a highly diluted solution to the droplets. As a result, acids appear to be more acidic in the droplets. In our experiments, seven types of organic acids with partition coefficients (LgP) ranging from -0.7 to 1.87 dissolved in an oil solution are extracted into aqueous nanodroplets on a substrate. The timescale of coupled extraction and colorimetric reaction in the droplets was revealed by the decoloration time of the droplets. Our results show that the effective distribution coefficient of the acid can be shifted by 3 to 11 times of the distribution coefficient in bulk. Such significantly shifted partition is attributed to enhanced transfer of the acid across the droplet surface from a highly diluted solution. The chemical reaction in the droplets enhances the partition of the analyte. Our results show that the interfacial activity of the analyte may be advantageous as it may also improve extraction and partition. Such enhanced extraction by chemical reaction in droplets may be leveraged for sensitive chemical detection using reactive droplets.

### **Chapter 4. In-situ fabrication of metal oxide nanocaps based on biphasic reactions with surface nanodroplets**

*(Published paper: Wei, Z., Dabodiya, T., Chen, J., Lu, Q., Qian, J., Meng, J., Zeng, H., Qian, H. & Zhang, X. (2021). In-situ fabrication of metal oxide nanocaps based on biphasic reactions with surface nanodroplets. Journal of Colloid and Interface Sci-*

*ence, 608(3), 2235-2245.*

Surface-bound nanomaterials are widely used in clean energy techniques from solar-driven evaporation in desalination to hydrogen production by photocatalytic electrolysis. Reactive surface nanodroplets may potentially streamline the process of fabrication of a range of surface-bound nanomaterials invoking biphasic reactions at interfaces. In this work, we demonstrate the feasibility of reactive surface nanodroplets for in-situ synthesis and anchoring of nanocaps of metal oxides with tailored porous structures. Spatial arrangement and surface coverage of nanocaps are predetermined during the formation of nanodroplets, while the crystalline structures of metal oxides can be controlled by thermal treatment of organometallic nanodroplets produced from the biphasic reactions. Notably, tuning the ratio of reactive and nonreactive components in surface nanodroplets enables the formation of porous nanocaps that can double photocatalytic efficiency in the degradation of organic contaminants in water, compared to smooth nanocaps. In total, we demonstrate in-situ fabrication of four types of metal oxides in the shape of nanocaps. Our work shows that reactive surface nanodroplets may open the door to a general, fast and tuneable route for preparing surface-bound materials. This fabrication approach may develop new nanomaterials needed for photocatalytic reactions, wastewater treatment, optical focusing, solar energy conversion and other clean energy techniques.

## **Chapter 5. Nanorings of silver nanoparticles for surface enhancement Raman scattering**

*(Under preparation: Wei, Z., Li, Y., Zeng, H., & Zhang, X. Nanorings of silver nanoparticles for surface enhancement Raman scattering)*

Surface enhancement Raman scattering (SERS) is a powerful and ultra-sensitive chemical sensing method in biomedical diagnosis, forensic, food safety, environment, control of illicit, drug use and among others. In this work, we fabricated highly ordered nanorings of silver nanoparticles by simple droplet-based approach for SERS. The biphasic reaction between Vitamin E in surface nanodroplets array and silver salt

in the surrounding produces a ring of silver nanoparticles. The reaction conditions (pH values and precursor concentrations) were tuned to optimize the nanoring array for high SERS activity in the detection of a model compound Rhodamine 6G in an aqueous solution. SERS signal from nanoring arrays were quantitatively correlated with the analyte concentration ranging from 10  $\mu$ M to 10 nM. Good reproducibility in SERS signal intensity enables quantification by using nanoring arrays of silver nanoparticles. In addition, nanorings fabricated on a transparent glass substrate further improve the SERS activity with LoD of 1 nM. Our droplet-based approach demonstrates a feasible, controllable and green (no toxic solvent) method to fabricate SERS substrate for quantitative analysis of chemicals.

## **Chapter 6. Conclusion and outlook**

This chapter summarizes the major contributions of this thesis and recommends future research on surface nanodroplets formation by solvent exchange process.

## Chapter 2

# Integrated nanoextraction and colorimetric reactions in surface nanodroplets for combinative analysis

### 2.1 Introduction

Surface nanodroplets are liquid droplets on a solid substrate in contact with an immiscible fluid medium. These droplets are tens to several hundreds nanometer in the apex and several hundred nanometer to tens of micrometer in the base diameter.[64] These droplets with femtoliter or even less in the volume are stable for a long time against evaporation or dissolution, due to an immiscible external liquid phase, possessing desirable characteristics that enable novel applications in the field of chemical analysis. As compounds with higher solubility in the droplet liquid can be extracted

and concentrated in surface nanodroplets, liquid-liquid nanoextraction can be employed for in-situ ultrafast analysis of liquid samples with very small volume (such as sneezing droplets) [90], and for automated determination of partition coefficient(LgP) of drug molecules in a continuous flow system.[74]

Thanks to the large surface-to-volume ratio, nanodroplets also provide a steady and well-controlled microcompartmentalized environment for biphasic reactions in need of reagents in the immiscible phases of droplets and an external solution in the flow. [87] Many chemical reactions in microdroplets are found to be faster and more efficient than their macroscopic counterparts in a bulk medium[91]. Even some reactions impossible in the bulk system without catalysts can occur spontaneously in microdroplets. Combining reactive component and non-reactive extractant in surface nanodroplets is especially powerful, as these binary droplets provide enhanced sensitivity from a high concentration of the analyte extracted into the droplets. The concept of integrating nanoextraction and chemical detection has been demonstrated in quantitative in-situ detection by surface-enhanced Raman spectroscopy[74].

Recent advance in nanodroplets generation by solvent exchange offers new opportunities for nanodroplets-based chemical analysis, as it is possible to produce multi-component droplets by this simple method.[74] The ratio of different components in the droplets is controlled by their respective oversaturation created by the solvent exchange.[74] Droplets can contain various types of solvents, their combinations or solid solutes, [85, 90] providing a general platform for droplet-based sensing. Up to now, what rarely explored is the characteristic time scale from integrated nanoextraction and chemical reactions in surface nanodroplets for chemical identification. For a given external concentration of the compound, the extraction rate of surface nanodroplets is not specific to the compound but is associated with its solubility difference in the droplet and in the surrounding liquid at equilibrium (i.e. partition coefficient). If the extracted analyte reacts with a chemical in the multicomponent droplets, the reaction rate will reflect the solubility of the analyte, allowing for categorizing compounds

based on the solubility. If other property of the analyte can also play a role in the reaction rate, the timescale of the product from the droplet reaction will be resulted from the synergistic effect from the solubility and other property, and hence more specific to the compound. With increasing the number of analytes extracted to the reactive droplets, the time scale for the product can be more complex from combined effects of all components in the solubility family, and be even unique for the mixture. To demonstrate this concept of combinative analysis by using reactive surface nanodroplets, we choose the detection of a mixture of organic acids in one-step.

Detection of acidic compounds is critically important in many areas, such as controlling the flavors and quality of food, and anti-corrosion of petroleum and gasoline products. [92–96]. In many cases, acidic compounds are presented in the oil phase, ranging from heavy oils, petroleum products to cooking oil, beverages and essential oils for well being and medical use [92–94].

Colorimetric detection of organic acids in an aqueous medium could contribute to eliminating the risks of using highly toxic organic solvents in analysis of acids in oil. However, there are challenges for detecting acidic compounds in oil by using the aqueous solution of the indicator, as the reaction requires access to the reagents in two immiscible liquids, oil and water. Intrinsic characteristics of biphasic reactions could be severely influenced by the inefficient mixing, due to the limited interface between oil and water in the bulk medium. Thus it often requires a long time for acidic compounds to achieve equilibrium within the oil-water system.[97]

Furthermore, as the colorimetric reaction occurred in aqueous solution reveals the acids that are transferred into the water, the acid concentration in the oil phase may be determined only when the oil-water partition coefficient ( $\lg P$ ) of the acid is known. [98, 99] In many cases,  $\lg P$  of the acid is not necessarily available for given detection conditions and the determination of  $\lg P$  is also time and equipment consuming. [87, 100–102] To overcome the above challenges, a detection process that can reduce the time for partition equilibrium and can minimize the chemical consumption becomes

highly valuable for detection of acidic compounds in oil.

In this work, we will show a nanodroplets-based combinative approach for colorimetric detection and identification of organic acid family in oils. The droplets containing pH indicators show visible and sensitive colorimetric response to organic acids extracted from the surrounding oil flow. The rate of the response is related to the type of acids, due to the effect of partition coefficient and dissociation constant of the acid on the transport into the droplets. The colorimetric reactions in the droplets are utilized to identify the profiles of acidic compounds in a mixture. The potential application of combinative analysis by nanodroplets is demonstrated in anti-counterfeiting of expensive alcohol drinks.

## **2.2 Experimental section**

### **2.2.1 Chemicals and materials**

1-octanol (95%, Fisher Scientific, Canada) was selected as a modeling oil because the partition coefficients of many chemicals in octanol and water are available in the literature. The halochromic compounds were Bromocresol green (BG, yellow to blue at pH 3.8 to 5.4), bromocresol purple (BP, yellow to purple at pH 5.2 to 6.8). All halochromic compounds were purchased from Fisher Scientific (Canada). Several different types of acids in oils were tested, including citric acid (99.5%), gallic acid (97.5%), 4-hydroxybenzoic acid (99%), benzoic acid (99.5%) and trimesic acid (99%), all purchased from Sigma-Aldrich (Canada). Acetic acid (99.7%) and heptanoic acid (98%) were purchased from Fisher Scientific (Canada). The LgP and dissociation constant (pKa) of each acid are shown in Table 2.1. Water was obtained from Milli-Q water purification unit (Millipore Corporation, Boston, MA, USA).

Table 2.1: Molar mass, pKa and LgP of each acid from literature

| Acids                 | Molar mass $/g \times mol^{-1}$ | pka[103–<br>109]     | LgP [104–108,<br>110, 111] |
|-----------------------|---------------------------------|----------------------|----------------------------|
| Citric acid           | 192.12                          | 3.13 <sub>pKa1</sub> | -1.64                      |
| Acetic acid           | 60.05                           | 4.76                 | -0.17                      |
| Heptanoic acid        | 130.18                          | 4.4                  | 2.42                       |
| Gallic acid           | 170.12                          | 4.4                  | 0.7                        |
| 4-Hydroxybenzoic acid | 138.12                          | 4.54                 | 1.58                       |
| Benzoic acid          | 122.12                          | 4.2                  | 1.87                       |
| Trimesic acid         | 210.14                          | 3.12 <sub>pKa1</sub> | -0.56                      |

### 2.2.2 Formation of pH sensitive femtoliter droplets

Formation of surface droplets was performed in a fluid chamber through the procedure of solvent exchange [66]. The setup of the fluid chamber is similar to the one used in our previous report [74], as shown in 2.1a. In brief, silicon substrate (University Wafer, USA) was coated by 3-aminopropyl triethoxysilane (APTES) [112]. The APTES-coated substrate was cut into a slab and placed on the bottom of the chamber. The top plate of the fluid chamber was a cover glass that was cleaned by Piranha solution (30%  $H_2O_2$  and 70%  $H_2SO_4$ ). The distance between the cover glass and substrate surface was 300  $\mu\text{m}$ . The length and width of the channel was 4.5 cm and 1.3 cm,

respectively.

Solution A was a solution containing water, 1-octanol, ethanol (95%, Fisher Scientific, Canada), and halochromic chemical compounds (BP or BG). The ratio of ethanol, water and 1-octanol in solution A was 60:26:14 by volume. Colored droplets were formed by solvent exchange using solution A containing BG or BP. When BP was used as the indicator in the droplets, 0.1g of BP and 0.1g of sodium acetate were added into 50 ml solution A. Here sodium acetate (buffer, 99%, Fisher Scientific, Canada) was used to adjust the initial pH of the droplets. When BG was the indicator in the droplets, 0.1g of BG was dissolved in 50 ml solution A.

Solution B was 1-octanol saturated by water. During the process of solvent exchange, the fluid chamber was filled with solution A that was then displaced by solution B at a controlled flow rate. Water droplets containing halochromic compounds were formed on the surface of the substrate after solvent exchange, as shown in Figure 2.1b.

### **2.2.3 Detection of acids in oil phase**

After formation of the surface droplets, solution C was injected into the fluid cell at constant flow rate. Here solution C refers to water-saturated 1-octanol containing different types and concentrations of organic acids (i.e. target analytes). Solution C was made by directly dissolving the different acids into water-saturated 1-octanol by molar concentration. An upright optical microscope (Nikon H600l) equipped with 10X lens and a camera was used to capture the process of the color change of the droplets when the acids partitioned into the droplets, as shown in Figure 2.1b and c. To quantitatively measure the concentration of the partitioned acid in droplets, the time required for droplet color change was recorded at different concentrations of the acid. The time of discolor refers to the time that the color intensity of the droplet

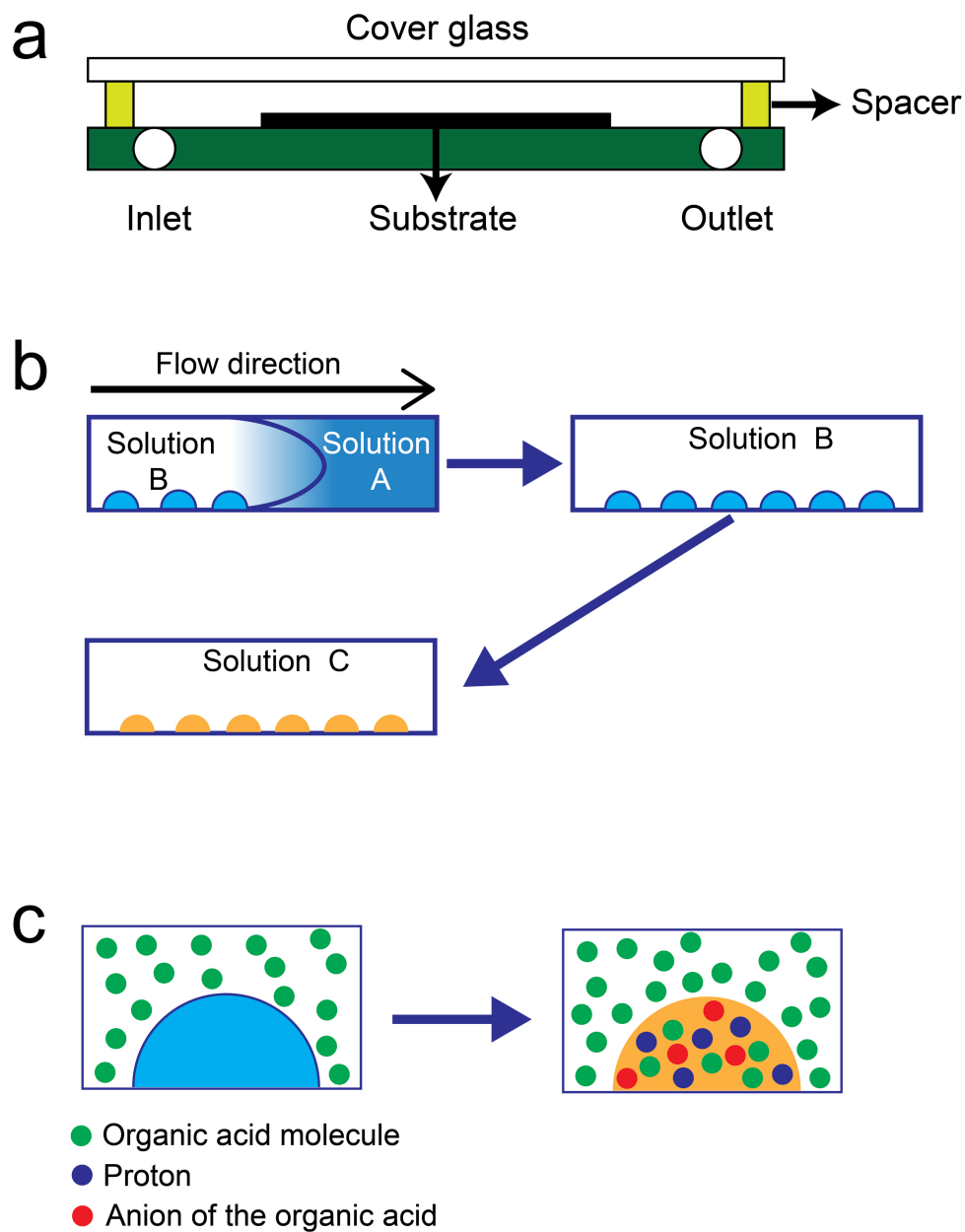


Figure 2.1: Schematic of preparing and applying surface droplets for the extraction and detection of acidic compounds in oil. (a) The sketch of the fluid chamber.(b) The formation process of the surface droplets containing pH indicator by solvent exchange and detection of the acid in oil (Solution C) by droplets contacting with the Oil flow.(c) Acid molecules in the oil phase are extracted into the aqueous droplets and react with halochromic compound in the droplets.

reached a fixed value from contacting with the acid in the oil. The color intensity, known as the color luminance, was directly measured by ImageJ.

#### **2.2.4 Detection of acids in an organic phase by bulk mixing**

To compare with the droplet-based approach, we performed bulk solution-based detection of acids in an oil phase by directly mixing the oil with an aqueous solution containing halochromic compounds. A cosolvent ethanol was used to facilitate the mixing process. The halochromic compound, BP or BG, was dissolved in water-ethanol solution (water: ethanol = 60:26 by volume ratio) at the concentration of 0.04% by mass ratio. Then 1-octanol containing acetic acid at different concentrations was added into the solution of the halochromic compound at 1:1 volume ratio, leading to formation of emulsion due to ouzo effect (oversaturation) [113, 114]. In another bulk mixing method, BP or BG was dissolved in water at the concentration of 0.04% by mass, and one volume of the prepared solution was added into a half volume of 1-octanol containing acetic acid at different concentrations.

#### **2.2.5 Colorimetric identification of acid mixtures and anti-counterfeiting of alcohol spirits by droplets**

Acid mixtures were prepared by directly dissolving three different acids (acetic acid, gallic acid and benzoic acid) into 1-octanol with three different concentrations, as shown in Table 2.2. Those ratios of acid mixtures have the same pH value in water. The pH values of the acid mixtures were measured by pH meter (Fisher, USA).

Four popular Chinese Liquors, Erguotou, Fenjiu, Fenjiu (30 years hoard time) and Maotai, were purchased from a local liquor store. To extract the acids from the liquor, 200  $\mu L$  of each spirit sample was added into 10 mL 1-octanol. The mixture was shaken for a few seconds and left standing for overnight. Afterward the mixture separated

into two phases. The top layer of octanol-rich phase was taken out (namely solution C) and injected into the flow chamber to interact with the indicating droplets for acid detection. The pH value of each spirit was shown in Table 2.3. All the pH values were measured by a pH meter(Fisher, USA). All the above experimental procedures were conducted at  $25^{\circ}C$ .

Table 2.2: Composition of different acid mixtures.

| Acid mixtures | acetic acid/M        | gallic acid/M        | benzoic acid/M       | pH   |
|---------------|----------------------|----------------------|----------------------|------|
| 1             | $2.6 \times 10^{-4}$ | $1.7 \times 10^{-3}$ | $2.0 \times 10^{-4}$ | 3.36 |
| 2             | $1.8 \times 10^{-5}$ | $3.3 \times 10^{-4}$ | $3.0 \times 10^{-3}$ | 3.36 |
| 3             | $5.6 \times 10^{-3}$ | $1.6 \times 10^{-4}$ | $1.2 \times 10^{-4}$ | 3.36 |

Table 2.3: pH value of Chinese spirit

| Spirits | Erguotou | Fenjiu | Fenjiu(30 years) | Maotai |
|---------|----------|--------|------------------|--------|
| pH      | 3.76     | 3.49   | 3.47             | 3.46   |

## 2.3 Results and discussion

### 2.3.1 Formation of colored droplets for acid extraction and detection

Following the process illustrated in Figure 2.1, droplets prepared by the solvent exchange[66] are few to tens  $\mu\text{m}$  in the lateral radius( $R$ ). For droplet sizes in this range, the color change of the droplets during the colorimetric reaction can be clearly detected by optical microscope. At the same time, the polydispersed droplets enable us to examine the effect from droplet size.

These droplets contain aqueous solution of halochromic compounds, exhibiting different colors to indicate the pH level inside droplets. The color of droplets containing two halochromic compounds used in this work, bromocresol green (BG) and bromocresol purple (BP), is shown in Figure 2.2. In an aqueous solution, the color of BG changes from blue to light yellow as pH decreases from 5.4 to 3.8 while BP changes from dark purple to light yellow as pH decreases from 6.8 to 5.2.

We have added sodium acetate into solution A to adjust the pH value above 7 in the formed BP droplets. The initial color of the droplets was purple, as shown in Figure 2.2a. Similarly, the initial color of BG droplets without sodium acetate was blue (Figure 2.2b). The formation of colored droplets demonstrates that incorporating halochromic compounds into droplets can be achieved by the simple process of solvent exchange.

The optical images in Figure 2.2 show the color change of droplet in contact with the flow of oil containing acetic acid after 5 minutes. The extracted acid from oil reacts with the halochromic compound in the droplets, leading to the loss of droplet color. The indicating formula of BP and BG with acid are presented in Figure 2.2. As control, the droplet color remained intact after the same period of time injection of pure 1-octanol.

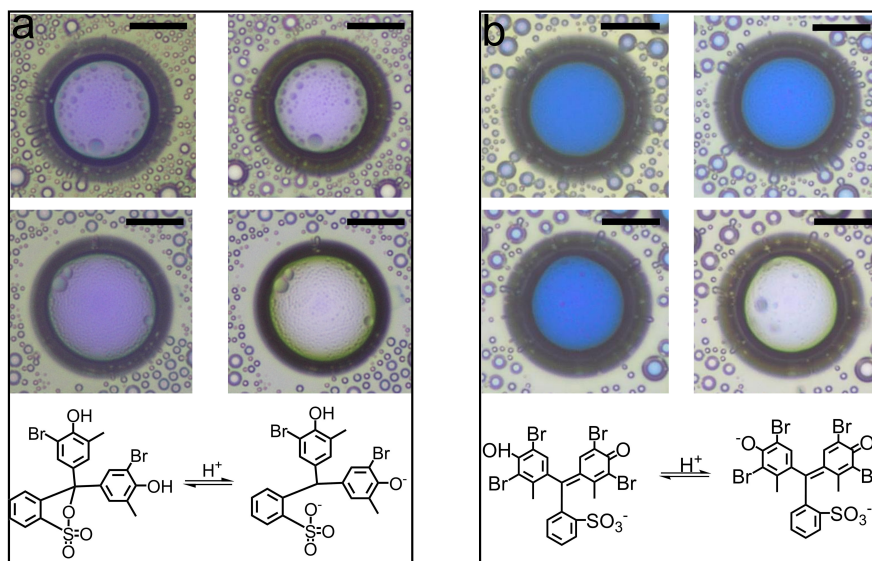


Figure 2.2: Color of a droplet containing halochromic compound before and after contact with acid. Molecular structures of BP and BG are shown on the bottom row. Top row: a droplet before (left) and after (right) in contact with 1-octanol for 5 minutes. Middle row: a droplet before (left) and after (right) contact with octanol containing  $1.7 \times 10^{-4} M$  acetic acid for BP droplet in (a) and  $1.0 \times 10^{-4} M$  acetic acid for BG droplet in (b). Length of the scale bar:  $25 \mu m$ .

### 2.3.2 Sensitivity of colorimetric reaction in droplets

The color of droplets is sensitive to the presence of acid in the oil. Figure 2.2a shows that BP droplets changed color after the injection of oil containing acetic acid at a concentration of  $0.17 \text{ mM}$ , suggesting such acid concentration in the droplets was high enough to shift the equilibrium of BP into colorless product. At an even lower concentration of the acid ( $0.1 \text{ mM}$ ) in oil, BG droplets changed from blue to colorless. Below these concentrations of acetic acid in oil, the amount of the extracted acid in

the droplets is so low that the droplets remain the original color. We simply refer this concentration of the acid in oil as the limit of detection (LoD) of the colorimetric reaction in droplets. The LoD of BP droplets for acetic acid in oil was around 0.17 *mM* and of BG droplets were even lower, around 0.1 *mM*.

We compared the LoD of droplets and two common shake-flask bulk methods shown in Figure 2.3. When the acid in oil was directly mixed with an aqueous solution of BP or BG, the dark blue color of the aqueous solution after oil-water phase separation changed to bright orange when the initial concentration of acetic acid in oil solution was above a certain level. The LoD was found to be 0.17 M for BP and 0.1 M for BG, three orders of magnitude higher than that of droplets. By the second method, acetic acid in oil was mixed with the solution of BG or BP in an ethanol aqueous solution (water: ethanol=60:26 by volume). Upon mixing, an emulsion formed due to the presence of the cosolvent ethanol through the well-known Ouzo effect [113]. The LoD was determined to around 0.17 M for BP mixture and is 0.01 M for BG mixture. We attributed the less sensitivity of BP due to the buffer sodium acetate existed in BP mixture, leading to a consumption of the acid component. Although the emulsion formation improves the sensitivity of the shake-flask bulk method, the LoD is still 2 orders of magnitude higher than that of droplets containing the same halochromic compound.

We attribute such sensitive response of colorimetric reactions in droplets to the preferable microcompartmentalized environment in the droplets. The partition of the acid from oil phase to water phase gives rise to a higher concentration of a water soluble acid in droplets. The limitation of droplet-based method is that acid has to be extracted into the droplets to react with the pH indicator in droplets, so the droplet color is less sensitive for those acids with long hydrophobic chains and much higher solubility in oil than in water. This droplet-based acid detection in oil is performed in a flow condition so it is fast, requiring a small amount of samples. Nontoxic solvent is involved in the entire process.

### 2.3.3 Acid specificity of colorimetric reaction rate in droplets

Apart from high sensitivity, an even more powerful feature of droplet-based detection is time-dependent response of droplet color. Figure 2.4a,c show the droplets of three representative sizes in contact with oil containing acetic acid of two different concentrations, 0.5  $mM$ (a) and 0.1  $mM$ (c). The plots showing the change of color intensity as a function of time within different sizes of droplets are presented in Figure 2.4b,d, respectively. For 0.5  $mM$  of acetic acid, the required time ( $t$ ) for droplet decolor (i.e., becoming colorless) was  $\sim 75$  s for a droplet diameter  $R$  of 8  $\mu m$ , and extended to  $\sim 185$  s for  $R$  of 43  $\mu m$  (Figure 2.4b). At given concentration of a specific acid, clearly the decolor time  $t$  increases with the increase in the droplet size. The faster color change suggests that the colorless product reaches a critical concentration faster in smaller droplets. When the concentration of acetic acid was reduced to 0.1  $mM$ ,  $t$  was 120 s for  $R$  of 9  $\mu m$  and extended to 259 s for  $R$  of 39  $\mu m$  (Figure 2.4d). The results suggest that for lower concentration of acid, the decolor time of droplets is longer. In addition, the dependence of the decolor time on the droplet size becomes increasingly pronounced at a lower concentration of acid.

The impact of droplet size on the colorimetric processing time was then systematically studied. Figure 2.5a shows the plot of the decolor time  $t$  against the droplet radius at different acid concentrations. Results reveal the dependence of decolor time on the droplet size is pronounced for larger droplets than smaller droplets. When the droplet radius is below 1  $\mu m$ , there is not much difference in decolor time, possibly due to similar transport rate of the acid into such small droplets and the limitation of the instrument to identify the slight difference. Moreover, the decolor time is dependent on the acid concentration. That is, at lower acid concentration, the dependence of decolor time on the droplet size is more pronounced. In addition to acetic acid, we

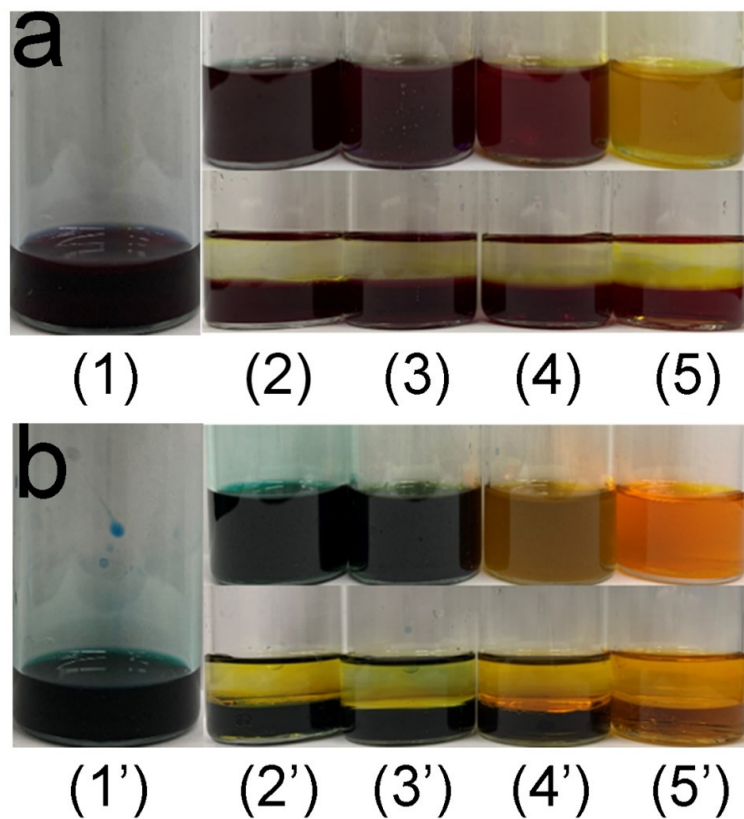


Figure 2.3: Test of two bulk mixing methods for detection of acetic acid in octanol by BP (a) and BG (b) aqueous solutions. 0.04% aqueous solutions of BP (1) and BG (1') were prepared by mass fraction. From (2) to (5), 1 mL (top row) and 2 mL (bottom row) of prepared BP solution were added into 1 mL 1-octanol containing acetic acid from the concentration of  $1.7 \times 10^{-4} M$  to  $1.7 \times 10^{-1} M$  with 10 times intervals. From (2') to (5'), 1 mL (top row) and 2 mL (bottom row) of prepared BG solutions were added into 1 mL 1-octanol containing acetic acid from the concentration of  $1.0 \times 10^{-4} M$  to  $1.0 \times 10^{-1} M$  with 10 times intervals.

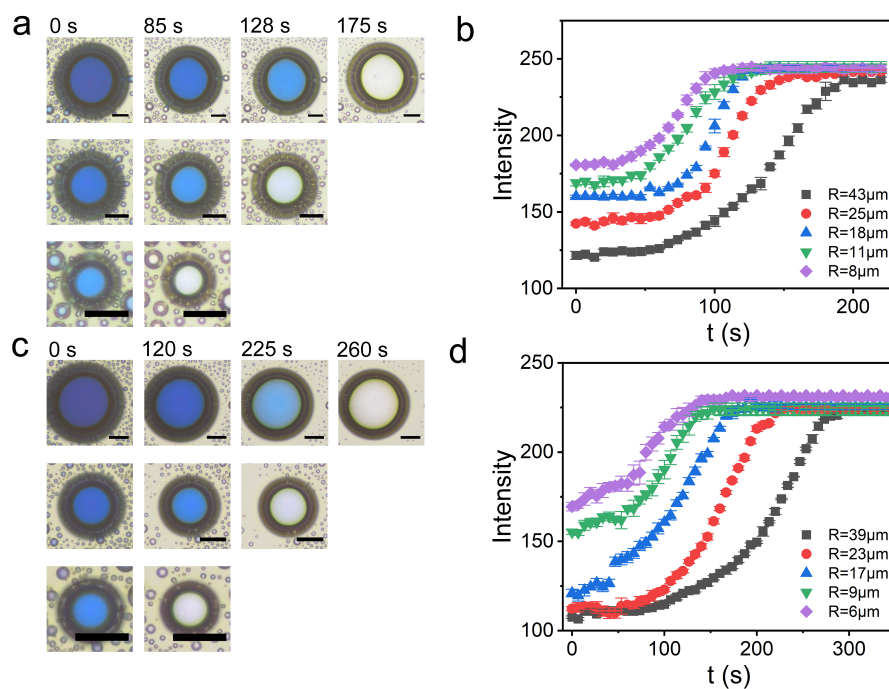


Figure 2.4: Detection of acetic acid in oil by surface droplets containing BG. (a) Time series images of droplet discoloration from  $5 \times 10^{-4}M$  acid in oil. The droplet size decreases from the top to the bottom row. Length of the scale bar:  $25 \mu m$ . (b) The color intensity at different time after the droplets in contact with oil containing  $5 \times 10^{-4}M$ . (c) Time series images of droplet discoloration from  $1 \times 10^{-4}M$  acid in oil. (d) The color intensity at different time after the droplets in contact with oil containing  $1 \times 10^{-4}M$ . The error bar is from three repeats of the measurement.

have also tested six other acids listed in Table 2.1. The results in Figure 2.5b show similar trends for all acids at the concentration of 5 *mM*. Comparing with a higher concentration of 50 *mM* (Figure 2.5c), the change of time is sharper at lower acid concentration.

Most importantly, the decolor time of droplets  $t$  exhibits specificity to the acid at

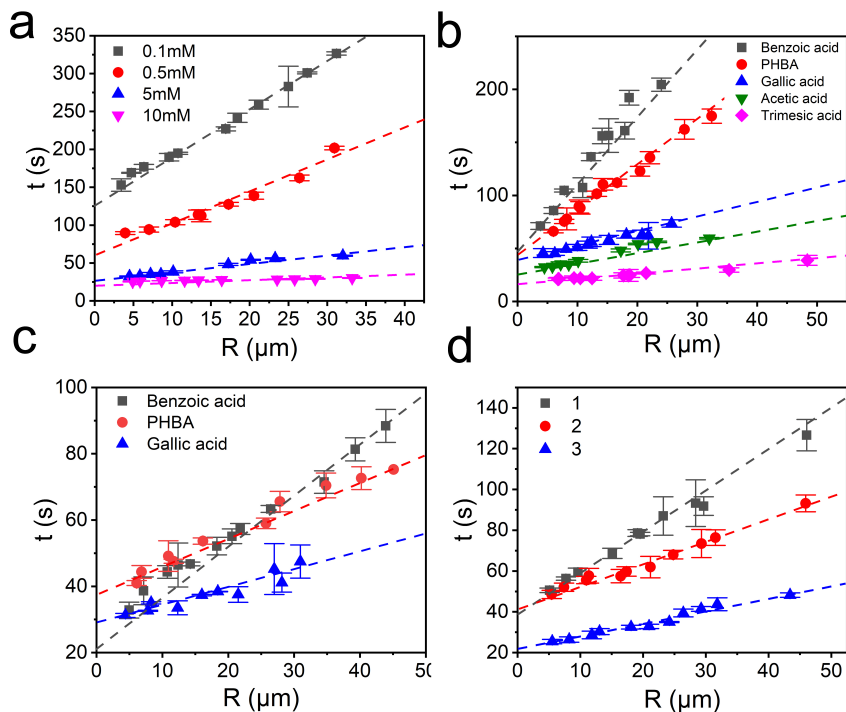


Figure 2.5: Detection of different acids and acid mixtures in oil by surface droplets containing BG. Time of the droplet discolor as a function of the droplet radius at different concentrations of acetic acid (a). The acid concentration is 5 *mM* in (b) and 50 *mM* in (c). (D) Detection of acid mixtures at different ratio in oil by surface droplets containing BG. Acetic acid, gallic acid and benzoic acid were mixed at different ratio, as shown in Table 2.2. Dotted lines are the linear fitting. The error bar is from two to three repeats of the measurement.

a low concentration, that is, the decolor time for the same-sized droplets depends on

the acid type. For instance, decolor time for a droplet of 20  $\mu\text{m}$  in radius is 200 s in response to 5  $mM$  benzoic acid in the solution, but is only 25 s to trimesic acid at the same concentration. With shorter decolor time for smaller droplets for all acids, the decolor time is around 100 s for benzoic acid and 20 s for trimesic acid. There is also a significant difference between benzoic acid and gallic acid at 5  $\mu\text{m}$ . As the acid concentration increases, the decolor time becomes so short that no clear difference can be measured for different types of acids. For instance at 50  $\mu\text{m}$ , the decolor time of the droplet at any size is close to 20 s for trimesic acid and the same-sized droplet is similar for both gallic acid and benzoic acid.

To explain the acid specificity in decolor time of droplets, we consider a simplified case where the transport of acid molecules from the oil into the droplet is a rate-determining step. Immediately after the intake into the droplets, acid molecules dissociate and react with pH indicator. The flow rate of the acid solution is constant in all measurements, so any influence of the external flow on the acid transport is expected to be the same for all experiments. The intake of the acid from the oil into the aqueous droplet is driven by the partition of acid in water. With time, the concentration of acid in water  $C$  with time  $t$  can be described by first-order reaction, as established in the early work on solvent extraction of a single droplet [115–118].

$$\frac{dC}{dt} = \frac{A}{V}D(pC_o - C_w) \quad (2.1)$$

Here the effective diffusion coefficient ( $D$ ) of the acid in the oil is on the same order of magnitude for different acids, considering that the effect from Taylor-Aris dispersion is same for all experiments at the same flow rate[68, 69, 119, 120] and the diffusion coefficients of all acids are similar in the oil solution.  $A$  is the surface area of the oil-water interface of the droplet where the intake of the acid takes place and  $V$  is the volume of the droplet.  $C_o$  and  $C_w$  are the concentrations of the acid in the oil phase and the water droplet at time  $t$ , respectively.  $p$  is the distribution coefficient  $p = \frac{C_o}{C_w}$  at equilibrium state. At decolor time  $t$ ,  $C$  reaches  $C^*$ (the critical concentration) so

that the proton from acid dissociation reaches the level that is sufficiently high for the color change of the pH indicator. After integration and transformation[115], Eq.2.1 can be re-written.

$$t \sim \frac{R}{D} \ln\left(1 - \frac{pC^*}{C_o}\right) \quad (2.2)$$

Where  $R$  is the radius of the droplets. Based on Eq. 2.2, it is clear that from the same type of acid at given acid concentration, the decolor time is longer for larger droplets and the time increases linearly with increase in the size of the droplets. For different acids, the decolor time depends on the distribution coefficient  $p$ , which influences  $C_w$  in the droplets. Both distribution coefficient and dissociation constant of the acid in the droplet contribute to the transfer rate of the acid into the droplets, giving rise to the acid specificity of the decolor time.

The timescale for the acid transport analyzed above is only one of the steps that can influence the decolor time. Other possible steps are dissociation of the acid to produce protons and eventually reaction kinetics of the acid with the pH indicator in the droplet.

For a weak acid with a long hydrophobic chain, the adsorption and desorption on the droplet surface may also play an important role in the decolor time. Future work is required to establish quantitative correlation between decolor time and all steps that contribute to the acid specificity.

Here we can also provide a good correlation between acid properties and their LoD in droplet. Considering the volume of droplets is very small, on an order of femtoliter, we can assume that the acid concentration in the droplets can reach an equilibrium with the oil phase. We estimate the concentration of  $H^+$  in the droplets from the concentration in oil, partition coefficient, the dissociation coefficient in water. For a polyprotic acid, such as citric acid, we only consider the first order of dissociation because the second and third dissociation are very weak (with each decreasing in the orders of magnitude). The partition coefficient  $lgP$  is defined by the equilibrium constant of the acid in water and oil.

$$LgP = Lg \frac{[HA]_O}{[HA]_W} \quad (2.3)$$

$$[H^+]_W = (K \times [HA]_W)^{1/2} \quad (2.4)$$

$[HA]_O$  and  $[HA]_W$  are the concentration of the acid in oil and the un-dissociated acid in water[121], respectively.  $K$  is the dissociation constant of the acid in water droplets.

To show the dependence of LoD on lgP in oil and water, we determined the LoD of four organic acids with the partition coefficient ranging from -1.6 to 2.48. As listed in Table 2.4, a lower partition coefficient of the acid in oil leads to a lower LoD and more sensitive detection by colorimetric reaction in droplets. Considering the same dissociation constant, the acid concentration in the droplets is expected to be higher for an acid with a higher partition coefficient at a given acid concentration in the oil phase.

The correlation among partition coefficient LgP, dissociation constant and LoD of acid in colorimetric reactions allows us to determine one parameter if the other two are known. For acetic acid, our measurements show that the minimum concentration in oil needed for the color change of droplets (i.e. LoD of acetic acid in oil) is  $1 \times 10^{-4}M$ . At the LoD, the corresponding concentration of acetic acid in water droplets  $[HA]_W$  is determined to be  $1.48 \times 10^{-4}M$  according to Eq.2.3 with LgP of -0.17 based on the literature[122]. The dissociation constant (pKa) of acetic acid in water is 4.76 in literature [103]. Therefore for  $1.48 \times 10^{-4}M$  of  $HA$  in droplets, the concentration of  $[H^+]$  from dissociation is  $5.07 \times 10^{-5}M$  (pH of 4.29), calculated from Eq.2.3 and 2.4. This calculated  $[H^+]$  in the droplets is in good agreement with the range of pH level for BG to change from yellow to blue at pH of 3.8 to 5.4. Similarly, if we know both the dissociation constant of the acid in water and the partition coefficient of the acid between water and oil, we can predict the LoD of the droplets in our measurements, which is the minimum concentration of a certain acid in the oil phase in equilibrium

Table 2.4: LOD of different acids by using BG droplets and the calculated LgP of each acid.

| Acids          | LoD from experiment | LgP from calculation | LoD from calculation |
|----------------|---------------------|----------------------|----------------------|
| Citric acid    | $0.001mM$           | -0.55                | $8 \times 10^{-5}mM$ |
| Acetic acid    | $0.1mM$             | -0.17                | $0.1mM$              |
| Gallic acid    | $0.5mM$             | 0.88                 | $0.32mM$             |
| Heptanoic acid | $50mM$              | 2.48                 | $16mM$               |

with the concentration of  $H^+$  in the droplets for color change.

Identically, for a given pH indicator( $H^+$  is known), when we know the LgP and pKa from the literature, the theoretical LoD( $HA_O$ ) can be calculated by using Eq. 3 and 4. The calculated LoD of acids are shown in Table 2.4. The calculated LoD of all acids, except citric acid, have good agreement with the experimental one, suggesting the important role of participation coefficient and dissociation constant in the colorimetric reactions in the droplets. The calculated LoD of citric acid is very low due to its low LgP. At very low concentration of citric acid, much longer time is needed for the completion of extraction process, as revealed by Eq. 2. In our experiments, the time window for decoloration is around 5 minutes to ensure the droplets cannot be dissolved by the continuous solution flow. This time window may not be sufficient for complete extraction of citric acid, which may lead to higher LoD from the experiment than that from calculation.

Although the dependence of decolor time on the type of acid is not as specific as fingerprints in molecular spectra, this specificity can be very useful when we compare acid matrix in a solution. We demonstrate this concept by using model mixtures of acids and then apply the concept for identifying alcoholic drinks of good and bad quality in anti-counterfeiting. Figure 2.5d shows the detection of acid mixtures with compositions listed in Table 2.2. With three different combinations of three acids, the pH value of all three mixtures is at 3.36 as determined from the measurements by using a pH meter. However, when BG droplets are in contact with oil containing the acid mixture, the decolor time  $t$  is different especially for larger droplets. It takes the longest for mixture 1 and the shortest for mixture 3. Therefore the decolor time of the droplets can be used for identifying whether the acid profile is the same when the total acid level is the same.

### **2.3.4 Colorimetric analysis of acid mixtures for anti-counterfeiting alcoholic drinks**

To demonstrate one possible application based on colorimetric reactions in droplets, we show an identification of a counterfeit alcohol spirit by evaluating the profile of organic acids in the alcoholic beverage. Counterfeit spirits are normally inferior spirits to replace upmarket spirits. For instance, a typical counterfeit Maotai may be a cheap spirit on the market or even a home-made one. Our droplet-based method is capable of distinguishing different types of spirits because each spirit has its characteristic acid profile. We expect such a complex acid matrix can give distinct decolor time for each spirit.

We tested four most popular Chinese spirits, Erguotou, Fenjiu (less expensive), Fenjiu (30 years) and Maotai. Erguotou and Fenjiu are the same type of Fen-flavor, while Maotai is soy sauce flavor. All of these four spirits contain over 27 types of organic acids from the brewing process with a high concentration (over 735 mg/L)[123, 124].

Figure 2.6a and b show the time series images of the droplets changing color in contact with oil containing the organic acids extracted from Fenjiu and Erguotou. At a similar droplet size, it takes 123 s for the droplets to decolor by interacting with Fenjiu, while a substantially longer time of 233 s, is required for the Erguotou samples prepared in the same way. The difference of  $t$  for Fenjiu and Erguotou samples demonstrates the potential application to distinguish different spirits by our method. Figure 2.6c shows decolor time  $t$  versus the droplet size  $R$  for Erguotou, Fenjiu, and Maotai. The time for the droplets to complete color change is longer for Erguotou than other spirits, indicating that the acid profiles of these two spirits are different, even they have a similar pH value.

A higher ratio of the hydrophilic acids in the spirits will lead to faster decoloration of the droplets. For Fen-flavor spirit, Fenjiu (30 years) is the most expensive and the cheapest one is Erguotou. Our method also can distinguish the spirit with different hoard time in the same brand (same feed stock and process). Figure 2.6d shows the time for the droplets to complete color change is shorter for Fenjiu (30 years) than common Fenjiu. Long hoard time of the spirit would help the long chain organic acid to break into short chain organic acid and help development of richer, more complex and more pleasant organic acid profile. The above results demonstrate that our surface droplet-based colorimetric detection can provide a fast reference to evaluate the organic acids profile, which is effective in distinguishing authentic spirit from the counterfeit samples.

Finally, we note that the droplet-based spirit detection can be possibly acquired by simply using the camera on a smart phone. Figure 2.6e and f show the images of the colored droplets with visually observed sizes are captured by a smartphone camera Huawei(P30 Pro). When the sample extracted from the Fenjiu was introduced into the detector, a distinct decolor of the droplets was observed within 180 s, as presented in Figure 2.6e. In contrast, the decolor of the droplets can not be completed within the same period when the detection of Erguotou was carried out, as presented in

Figure 2.6f. The fast and optical assessment to the acid level in beverages may be potentially applied to distinguish the spirits with different years of aging (e.g., 5 years versus 10 years), based on the difference in the acid profile in the drinks. The results demonstrate the low-cost and equipment-free potentials of the colorimetric detection based on surface droplets for broad applications.

## 2.4 Conclusions

In summary, we have demonstrated a novel approach for combinative analysis of mixtures based on functional surface nanodroplets. The model analysts are organic acid mixtures. The halochromic compound in aqueous nanodroplets changes color in response to the dissociation of extracted acids from the oil. The coupled effect of partition coefficient and dissociation constant determines the nanoextraction rate, giving rise to the specificity of decolor time on the acid type. Such specificity of the colorimetric reactions in the droplets provides a sensitive method to compare the acid profiles in multiple component mixtures without time-consuming and expensive equipment. We demonstrate the application of nanodroplets-based combinative analysis in identifying counterfeit spirits of different brands. The principle behind the combinative analysis is general, relying on nanoextraction and chemical reactions in femtoliter droplets. The detection is obviously not limited to simple organic acids in our model systems, but applicable to many compounds that are extractable from sample solutions.

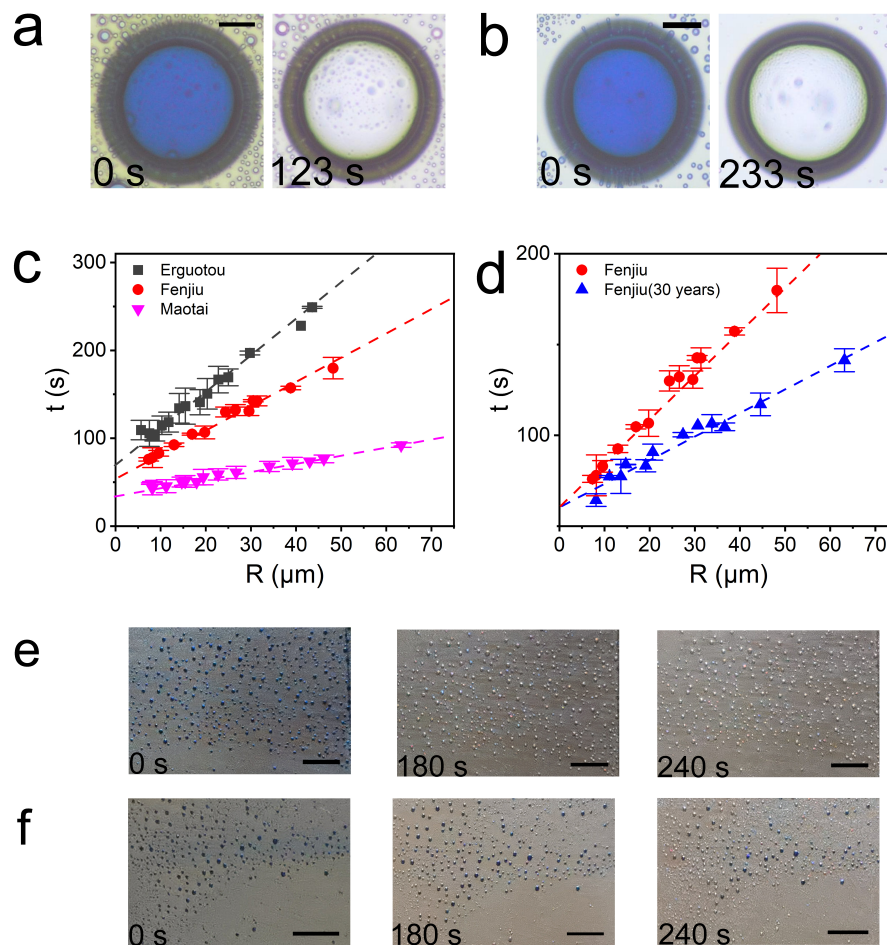


Figure 2.6: Determination of counterfeit Chinese spirit through surface droplet based nanodetector. (a) Time series pictures of the droplet discoloration from Fenjiu. (b) Time series pictures of the droplet discoloration from Erguotou. (c) Time of the droplet discolor versus the reciprocal of the droplet size from different spirit.(d) Time of the droplet discolor versus the reciprocal of the droplet size at two types of Fenjiu. Dotted lines are the linear fittings. The error bar is from three repeats of the measurement. The images of the droplet decoloration in contact with oil that contains compounds extracted from Fenjiu (e) and from Erguotou (f) at 0 s, 180 s and 240 s by using a commercial smartphone camera. (Length of scale bar:  $25 \mu\text{m}$  in a,b and  $2 \text{ mm}$  in e and f)

# Chapter 3

## Interfacial partitioning enhances microextraction by multicomponent nanodroplets

### 3.1 Introduction

Sample pretreatment plays a vital role in chemical identification and quantification with reliability and sensitivity. [8, 125–127] Many analytic techniques require the analytes to be separated from interfering substances in the sample or be transferred to a suitable medium for meaningful and high-quality measurements. Standard bulk protocols for separation of the analyte from a complex sample consume a large number of toxic solvents and therefore are regarded as one of the most polluting steps in chemical analysis. It is estimated that the solvent waste from liquid chromatography alone is about 34 million liters in a year.[128]

Integrating separation and detection of the analyte in small droplets is a way to mini-

mizing solvent use, automating and streamlining sample pretreatment and detection, and developing greener and cleaner analytic protocols. Transferring the analyst to small droplets can be fast and efficient across the interface of two immiscible phases due to the large surface area to volume ratio of the droplets. Moreover, the droplets may provide a discrete local environment where indicative reactions with the extracted analyte may take place to produce detectable signatures for in-droplet analysis. However, a fundamental question to be addressed for in-droplet chemical analysis is how the chemical reaction in droplets impacts the dynamics and the equilibrium of the analyst partition from the surrounding medium.

Liquid-liquid microextraction is based on the solubility difference to extract the compounds from the surrounding phase into microdroplets.[121] The concentration of the compound in microdroplet is related to the droplet size, the solubility of the compound and the extraction time.[115, 129] Assuming the droplet is water and the compound is dissolved in oil at the concentration of  $C_o$ ,  $C_w(t)$  is the concentration of the compound in the water droplet at time  $t$ .

$$\frac{dC_w(t)}{dt} = \frac{A}{V_w} \beta \left( \frac{C_o}{p} - C_w(t) \right) \quad (3.1)$$

Here  $V_w$  is the volume of the droplet and  $A$  is the interface area where the partition of the compound takes place.  $\beta$  is a coefficient that describes the interfacial transfer of the compound from the surrounding solution into the droplet. At thermodynamic equilibrium, the enrichment efficiency is limited by the partition coefficient  $p$  ( $\frac{C_o}{C_w(f)}$ ), defined as the ratio of the analyte solubility in the extractant liquid and the aqueous solution. Eq. 3.1 suggests that for a given concentration of the surrounding solution  $C_o$ , the concentration of the solute in extractant droplets increases faster for smaller droplets.

As separation and extraction of the analyte is coupled with chemical reaction, the rate of the entire process is determined by the slowest rate-limiting step. The dimensionless number Damköhler number (Da) relates the timescale of chemical reaction to

that of the mass transport in a system. [130] However, the reaction rate in droplets is a complicated topic that has not been fully addressed in the literature, even for some basic and well-known chemical reactions.

Many chemical reactions are reported to be usually much faster in smaller droplet than in the bulk [83, 131], such as acid-base reaction,[83] dehydration,[33] organometallic reactions[132], and among others. The reaction rate in microdroplets may be accelerated to a factor of one million, [29, 31] while other reactions that requires catalysts in the bulk may take place spontaneously in micro-sized droplets without a catalyst. [32] Accelerated chemical reactions in droplets are also confirmed under various configurations,[33, 35, 133, 134] including spray droplets[133, 135], colliding droplet [31, 136], or levitated droplets, [33, 137] and among others. [138, 139]

To date, the mechanism that leads to the accelerated chemical reaction in microdroplets remains elusive.[29]. The hypothesis is that the molecules are more energetic at the droplet surface, [38] analogous to the enhanced rate of reaction and product collection at the liquid-liquid or liquid-gas interfaces [29]. Perhaps the interface region of the droplets may also have a faster refresh rate than in bulk liquid. [40] Apart from the chemical reaction rate in the droplets, chemical species at the interface may also have a profound influence on the thermodynamic equilibrium of the partition of the compound in the droplets [40], especially for those amphiphilic molecules with a strong affinity to the interface. [140, 141].

Recently surface nanodroplets have emerged to be a well-controlled platform for integrated droplet extraction and chemical analysis. These nanodroplets are ultrasmall droplets on substrates submerged in an immiscible liquid surrounding [66]. Here nanoscale refers to the maximal height of droplets that are tens to several hundreds of nanometers, although the base diameter of the droplets ranges from several hundred nanometers to tens of micrometers. [85] Several characteristics of surface nanodroplets are advantageous for integrated extraction and analysis. With such small dimensions surface nanodroplets remain stationary for long time under a flow, complementary to

extracting microdroplets that flow in microfluidic devices. The concentration of the analyte in the surrounding that surface nanodroplets are exposed to can be easily mediated by the flow condition of the analyte solution. Furthermore, the concentration of the reactive components in surface nanodroplets can be tuned during a bottom-up nanodroplets production by the solvent exchange method. [7, 74, 142]

In our latest work [129], surface nanodroplets of an aqueous solution were applied to separate and quantify mixtures of organic acids from oil solutions. The originally blue droplets lost color due to the reaction between the extracted acid and the halochromic compound in the droplets. Interestingly, the timescale of the reaction as reflected by decoloration time was found to be specific to the acid type as well as the combination of acids in a mixture of the same pH level. Although the acid specificity of droplet decoloration time may be possibly related to the interfacial properties of individual acids, it remains unclear how interfacial phenomena are intertwined with microextraction and the reaction of the analyte in the droplets.

In this work, we try to address the role of interfacial partitioning in integrated extraction and chemical reaction in colorimetric detection by multicomponent nanodroplets. Our model compounds are organic acids that are extracted into surface nanodroplets and react with a pH indicator dissolved in the droplets. The timescale of the colorimetric reaction in the nanodroplets will be examined as the droplets are exposed to diluted and concentrated solutions of seven types of acids with a wide range of partition and solubility properties. Significant shifting in acid partitioning is revealed at low concentrations of acids in the surrounding solution. A unified theoretic model is proposed to rationalize the rate of integrated extraction and reaction in droplets and the enhanced partition of the acids. This work may contribute to better understanding of extraction efficiency of reacting droplets, in particular, on the coupling between interfacial transfer and chemical reaction with highly diluted analytes. The insights from this work may be valuable for downscaling the processes of separation in sensitive detection by using nanodroplets.

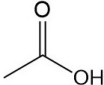
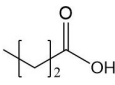
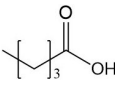
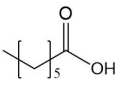
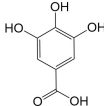
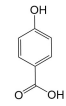
## 3.2 Experimental section

### 3.2.1 Chemicals and materials

Two groups of acids were tested for nanoextraction and colorimetric reaction. Group one consisted of alkyl acids, including acetic acid (99.7%), n-butyric acid (99.0%), valeric acid (98.0%) and heptanoic acid (98.0%). Group two consisted of aromatic acids, including gallic acid (97.5%), 4-hydroxybenzoic acid (PHBA, 99%), and benzoic acid (99.5%). Acetic acid and heptanoic acid were purchased from Fisher Scientific (Canada). Valeric acid, n-butyric acid, gallic acid, PHBA and benzoic acid were purchased from Sigma-Aldrich (Canada). Some relevant properties of these organic acids (dissociation constant (pKa) and partition coefficient(LgP) along with their chemical structures are listed in Table 3.1. When  $LgP > 0$ , the acid is unfavorable to the water, while  $LgP < 0$  is favorable to the water.

1-Octanol (95 %, Fisher scientific, Canada) was used as the solvent for droplet formation and for the analyte solution. Ethanol (90 %, Fisher scientific, Canada) was used as a co-solvent in our ternary liquid system (1-octanol, water and ethanol). The halochromic compound (pH indicator) was Bromocresol green (BG), which changes color from blue to yellow at a pH of 5.4 to 3.8. Water was obtained from the Milli-Q water purification unit (Millipore Corporation, Boston, MA, USA). Silicon wafer (University Wafer, USA) coated by APTES (3-aminopropyl triethoxysilane) was cut to 1.3 cm  $\times$  1.5 cm as the substrate in our fluid chamber. The procedure for preparing APTES coating was followed identically to the reported work [112]. A frame of silicon rubber was used as a spacer to control the channel height of the fluid chamber to 300  $\mu$ m. A transparent glass slide was cleaned by piranha solution (30%  $H_2O_2$  and 70%  $H_2SO_4$ )(caution: piranha solution is highly caustic!) and then used to seal the fluid chamber as cover.

Table 3.1: Dissociation constant (pKa), partition coefficient (LgP), critical concentration ( $C_w^*$ ) and molecular structure (MS) of the acids used in this work.

|       |  |  |  |  |  |  |  |
|-------|--|--|--|--|--|--|--|
| Acids | Acetic acid  | N-butyric acid   | Valeic acid  | Heptanoic acid   | Gallic acid  | PHBA   | Benzoic acid   |
| Pka   | 4.76   | 4.82   | 4.84   | 4.4  | 4.4  | 4.54   | 4.20   |
| LgP   | -0.7   | 0.79   | 1.39   | 2.42   | 0.7  | 1.58   | 1.87   |
| MS    |  |  |  |  |  |  |  |

### 3.2.2 Formation of functional surface nanodroplets

Following the process illustrated in Figure 3.1a, aqueous droplets containing BG are formed on a substrate in a microfluid chamber by solvent exchange. The protocol is the same as our previous report.[129]. Colored surface nanodroplets were preformed in a microchamber by the solvent exchange[85, 129], as sketched in Figure 3.1 (a). In the process of the solvent exchange, solution A was firstly injected into the fluid chamber to completely fill it. Due to the solubility difference of the 1-octanol in two solvents, the colored surface droplets were then formed during the process of replacing of solution A with solution B at a constant flow rate of 15 ml/hr. Solution A for solvent exchange was prepared by mixing 1-octanol, ethanol, and water at a volume ratio of 60:26:14. Then BG was added into solution A at the concentration of 0.002 g/ml. The other two concentrations of BG in solution A, 0.02 g/ml and 0.0004 g/ml, were also used to test the influence of BG concentration in the project.

Solution B was 1-octanol saturated with water.

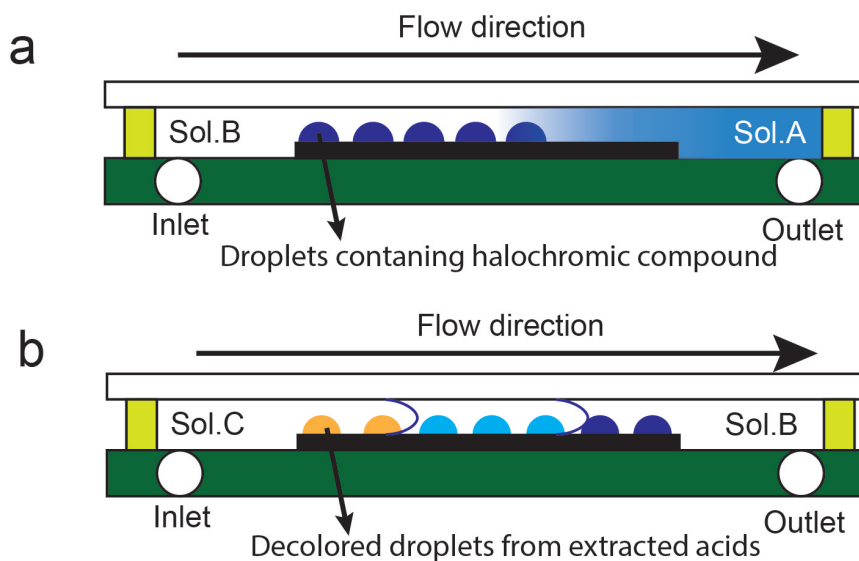


Figure 3.1: Sketch of forming droplets (a) and the acid extraction and the colorimetric reaction in the droplets (b).

### 3.2.3 Extraction of acid from the flow and colorimetric reaction in droplets

Once colored droplets were formed, acid extraction was from solution C, which had been prepared by dissolving a predetermined amount of various acids in 1-octanol. Solution C was injected into the fluid chamber at a constant flow rate of 50 ml/hr to replace solution B, as shown in Figure 3.1b. The acid concentration gradually increases at the mixing front of the solution B and C, due to the Taylor-Aris dispersion.[69, 119]. When the injected solution C was in contact with the droplets on the substrate, acid extraction and its reaction with BG in the droplets were triggered. The acid concentration in solution C was constant due to the large volume of solution C compared to the small volume of the droplets. The color of blue droplets gradually changed to yellow as a result that the acid concentration in the droplet reached the

critical concentration ( $C^*$ ). The process of the droplet decoloration with different concentrations of acids was recorded using an upright optical microscope equipped with a high-resolution camera (Nikon H6001). The recorded images and videos were analyzed by ImageJ for further evaluation.

### **3.2.4 Determination of temporal solute concentration in the flow**

A fluorescence dye, Rhodamine 6G (R6G), was used as the marker to trace the concentration of the solute in the flow at the mixing front of two solvents. R6G was directly dissolved in pure octanol as the tracer solution. The fluid chamber was firstly filled with pure octanol. Afterward, octanol was replaced by a flow of the tracer solution into the fluid at the flow rate of 50 ml/hr, the same as other experiments. The exposure time was 200 ms for each concentration. The fluorescence emission intensity of the tracer solution was detected and recorded by the microscope (Nikon H6001) equipped with a fluorescence filter. The recorded videos were analyzed by ImageJ. Three different concentrations of the R6G ( $1 \times 10^5$  g/L,  $5 \times 10^5$  g/L, and  $1 \times 10^4$  g/L) were tested with 3 repeats for each concentration to verify the reproducibility of the results. The exposure time was 200 ms for each concentration. The fluorescence emission intensity of the tracer solution was detected and recorded by the microscope (Nikon H6001) equipped with a fluorescence filter.

## 3.3 Results and discussion

### 3.3.1 Temporal concentration of the solute in the external flow

The temporal concentration of the analyte in a displacing flow supplied to surface nanodroplets is characterized by the fluorescence intensity of a dye solute in the solution. The plots in Figure 3.2 show that at given flow rates and chamber dimensions in our experiments, the analyte concentration increased from 0 to the maximum after a transient period. Here the time of 0 is defined to be the moment when the fluorescence intensity appeared in the field of view. At the completion of the flow displacement, the final fluorescence intensity corresponds well to the concentration of the dye in the solution (Figure 3.2(c)).

In the laminar flow regime, the temporal concentration of the analyte in the displacing flow is well-described by Taylor-Aris dispersion.[68] The real-time concentration of the analyte as represented by the fluorescence intensity can be fitted with an error function, as explained in our previous work[68].

$$C_o(t) = C_{ini} \times \text{Erf}\left(\frac{t}{\tau}\right) \quad (3.2)$$

Here,  $C_o(t)$  is the real-time compound concentration in the external solution in contact with the surface nanodroplets at time  $t$  (in second).  $C_{ini}$  is the organic acid concentration in solution, and is also the concentration when  $C_o(t)$  reaches the maximum.  $\tau$  is a characteristic timescale determined by the flow condition. From the fitting shown in Figure 3.2 (d) and Figure 3.8,  $\tau$  was determined to be around 12.87 seconds.

The temporal concentration of the model analytes of organic acids in our following experiments is expected to follow the same error functions for the dye concentration in the displacing flow. The acid concentration will increase initially from 0 to  $C_{ini}$

in the oil solution and afterward remained constant at  $C_{ini}$ . The acid concentration  $C_o(t)$  in the displacing flow will be determined by Eq.3.2 with the same  $\tau$  based on the dye concentration.

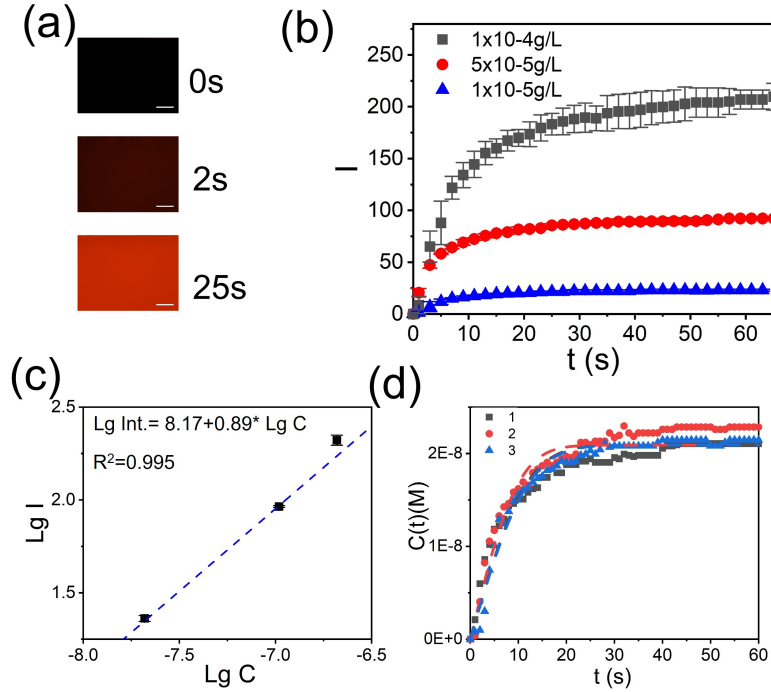


Figure 3.2: (a) Images of the fluorescence intensity changes during displacing pure octanol by the dye solution. (b) Fluorescence intensity (I) from the solution as a function of time. The dye concentration was  $1 \times 10^5$ ,  $5 \times 10^5$ , and  $1 \times 10^4 \text{g/L}$ , respectively. (c) Logarithmic plot of maximal fluorescence intensity versus the concentration of the dye in the solution. (d) Error function fitted (dashed line) dye concentration as a function of time at the dye concentration of  $1 \times 10^5 \text{g/L}$ .

### 3.3.2 Partition-dominated droplet decoloration at high concentration of acids

The organic acids used in our experiments can be defined as two groups, the alkyl acid group and the aromatic acid group. The molecule structure, partition coefficient (LgP in octanol and water) and the dissociation constant (pKa) of those acids in water are shown in Table 3.1. We first compared the decoloration time of the droplets at a given concentration of acids. A representative case in Figure 3.3a shows the color of droplets in contact with the flow of acid solution at  $C_o$  of 50 mM. The droplets were 25  $\mu\text{m}$  in radius. All the droplets changed from blue to colorless within 100 s. Figure 3.3b shows the plot of the droplet decoloration time as a function of the droplet size. The droplet decoloration is systematically slightly faster from valeric to gallic acid. There is no significant difference in decoloration time for other types of acids, except acetic acid. We attribute the fast decoloration of acetic acid to its low partition coefficient in water (LgP < 0). At an even higher concentration (100 mM) of PHBA and benzoic acid, the decoloration time of the droplets is also close to each other, as shown in Figure 3.9a.

Figure 3.3c shows the plot of the droplet decoloration time as a function of the droplet size for heptanoic acid at  $C_o$  of 50 mM to 2.5 M. Here, 50 mM is the lowest concentration of heptanoic acid that can lead to decoloration, defined as the limit of detection (LoD). Compared to others acids, it takes the longest time for the droplets to decolor at 50 mM. The slowest decoloration may be due to the highest partition coefficient of heptanoic acid (least soluble in water) among all acids. To determine the decoloration time, we need to consider the acid concentration in the droplet with time. In our experiments, the acid concentration was not constant in the initial 25 s. As the solution of acid in octanol solution was introduced into the chamber, the acid concentration changed from 0 to  $C_o$  at the mixing front, where the extraction already happened. The concentration of acid ( $HA$ ) in the oil solution  $C_o$  is a function of  $t$ ,

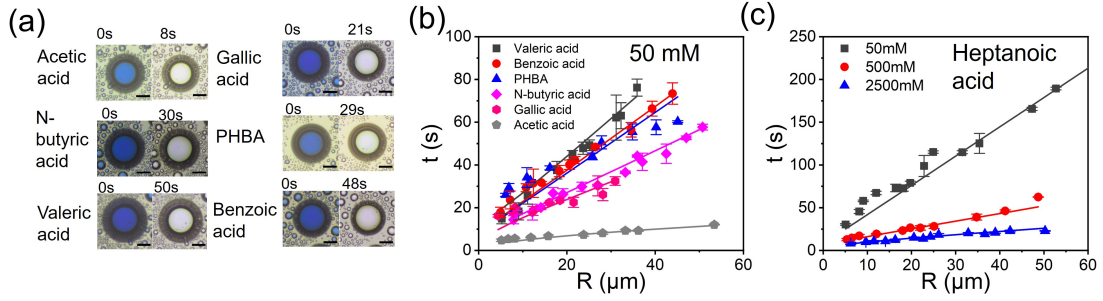


Figure 3.3: (a) Optical images and the time scale of the droplet decoloration in contact with the oil containing 50 mM of different acids. (b) The plot of droplet decolor time as a function of droplet size after injecting oil containing 50 mM of acids. (c) The plot of droplet decolor time as a function of droplet size after injecting oil containing 50 mM, 500 mM and 2500 mM of heptanoic acid.

determined by the flow rate of the acid solution. The flow rate was same in all of our experiments, giving the same profile of the acid concentration. Thus, we replace  $C_o$  by  $C_o(t)$  in Eq.3.1:

$$\frac{dC_w(t)}{dt} = \frac{3}{R}\beta\left(\frac{C_o(t)}{p} - C_w(t)\right) \quad (3.3)$$

Here,  $C_o(t)$  is represented in Eq.3.2. The extracted acid dissociates, producing protons that lead to the colorimetric reaction. The concentration of acid that is sufficient for droplet decoloration is defined as critical acid concentration  $C_w^*$ , calculated by pKa of a given acid and the pH value of the pH indicator.[129] When pH value is 3.8, the proton concentration is  $1.85 \times 10^{-4}\text{M}$ , the droplet finished the decoloration. Then, by using the simple acid dissociation equation,  $C_w^*$  can be obtained. The values of  $C_w^*$  for all the acids are listed in Table 3.2. LgP and pKa of a given acid were found from the data available in the literature, as listed in Table 3.1.  $C_o$  is known as our experimental condition, Eq.3.3 can be integrated to obtain the decoloration time  $t_{decoloration}$  for  $C_w(t)$  to increase from 0 to  $C_w^*$ . The interfacial transfer coefficient  $\beta$  is a fitting parameter.

The solid lines in Figure 3.3b and c are fitted by the theoretical model analysis of Eq.3.3. The predicted  $t_{decoloration}$  from Eq.3.3 is in good agreement with the experiment results. The difference in decoloration time of different acids is attributed to the variation in the partition coefficient of the acid in water and octanol.

At the acid concentration from 50 mM and above, the solid lines shown in the plots (Figure 3.4b, c and Figure 3.9a) fit all well with the theoretical model analysis based on Eq.3.3. The results show that the dependence of the decoloration time on droplet size can be described well simply based on the mass transfer from the displacing flow into the droplets through the partition. Coupled with the temporal concentration profiles of the solute in the displacing flow, the established partition mechanism for microextraction of droplets is sufficient to predict the timescale required for droplet decoloration. Any possible effect of chemical reaction in the droplets can be neglected at a high concentration of acids. At a high concentration of the solute in the surrounding phase, the chemical reaction inside the droplets does not show a significant impact on the extraction rate of the acid.

### 3.3.3 Enhanced partition at low concentration of acids

Interesting phenomena of enhanced extraction are discovered at low concentrations of acids. As shown in Table 3.1 and 3.2 for 5 mM acid solution, the concentration of acids in water droplets ( $C_w$ ) was calculated from the partition coefficient of the acids and the dissociation constant of the acids at the equilibrium state.  $C_w^*$  was estimated from pKa of the indicator in water. At low acid concentration, the extracted acid in a droplet would not reach critical concentration  $C_w^*$  if the only partition is responsible for the extraction. At the concentration of extracted acid in water ( $C_w$ ) that was lower than the predicted critical concentration of the acid ( $C_w^*$ ) for droplet decoloration, we found that the droplets can still lose color. For the least water-soluble

acid (heptanoic acid), the decoloration at low acid concentration was found at 50 mM. The extracted acid was expected to be  $2 \times 10^{-4}M$  according to the partition, lower than  $C^*(6 \times 10^{-4}M)$ . The results suggest that the pure partition is not sufficient to produce enough acids in the droplets for decoloration. An additional pathway must exist to provide more protons in the droplets for color change.

Table 3.2: Decoloration time of 5  $\mu m$  droplets from 5 mM of acid and the acid concentration ( $C_w$ ) in the droplets calculated from partition coefficient LgP.

| Acid         | Acetic | N-<br>butyric | Valeric | Gallic | PHBA | Benzoic |
|--------------|--------|---------------|---------|--------|------|---------|
| Time (s)     | 12.7   | 41            | 42.8    | 30.7   | 48   | 63      |
| $C_w$ (mM)   | 6.25   | 0.81          | 0.2     | 0.54   | 0.13 | 0.07    |
| $C_w^*$ (mM) | 1.44   | 1.66          | 0.6     | 0.7    | 0.9  | 0.4     |

Apart from the droplet decoloration at unexpectedly low concentrations of acids, reducing the concentration of acid in the displacing flow slows down droplet decoloration. For example, a 5- $\mu m$  droplet became colorless at 63 s from 5 mM benzoic acid, in contrast to the decolor time of 18 s from 50 mM acid in the flow. As  $C_o(t)$  reached the plateau, it is expected that partition equilibrium can be reached in a few seconds at most due to the small dimension of the droplets. However, the decoloration time as listed in Table 3.2 is much later than the moment when the acid concentration reaches equilibrium in the surrounding.

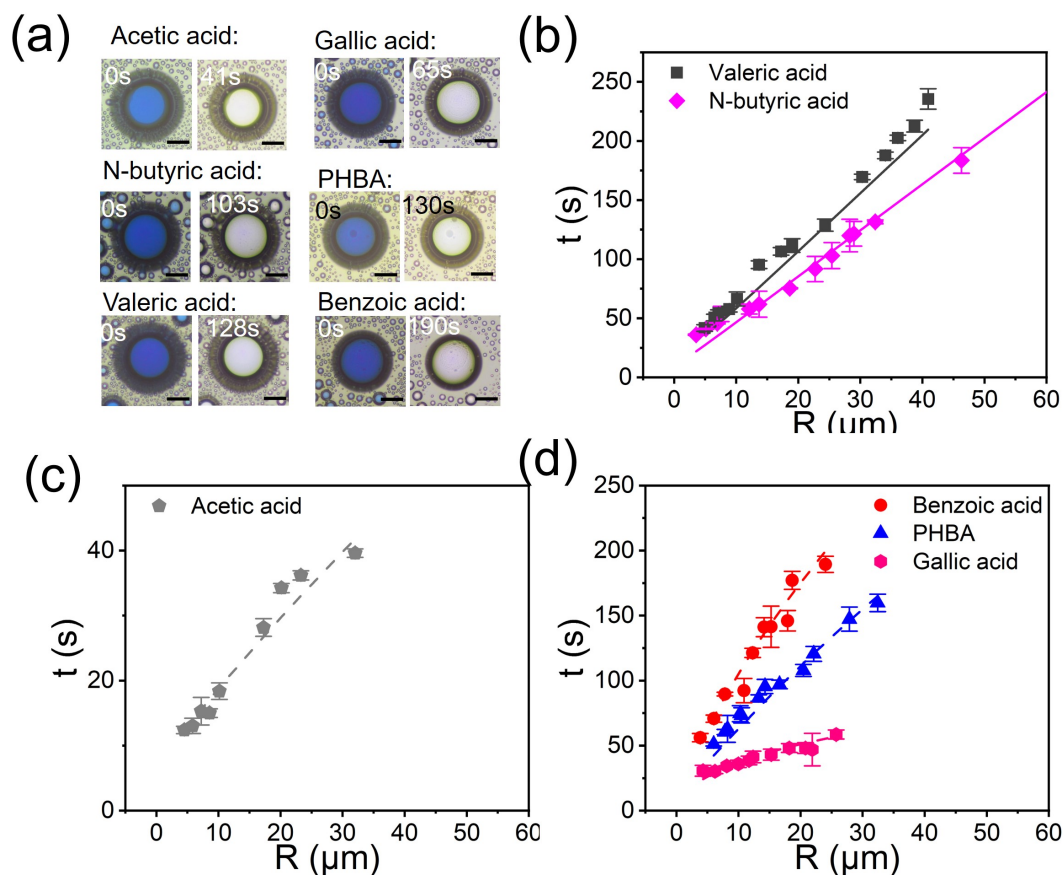


Figure 3.4: (a) Optical images of the same sized droplets ( $R=25 \mu\text{m}$ ) that change color at 5mM of acid in oil. Scale bar:  $25 \mu\text{m}$ . (b) The plot of droplet decolor time as a function of droplet size after injecting oil containing 5 mM of n-butyric acid and valeric acid. (c) and (d) are the plots of droplet decolor time as a function of droplet size after injecting oil containing 5 mM of acetic acid and aromatic acids, respectively. Solid lines in (b) were fitted from Eq.3.3. Dashed lines in (c) and (d) were fitted from Eq.3.7.

### 3.3.4 Interfacial partition enhanced by nanodroplets reaction

To rationalize the extraction in droplets at low concentration of acids, we propose interfacial partition enhanced by nanodroplets reaction as below. The droplet decoration process is decoupled into several steps as depicted in Figure 3.5. (1) Partition

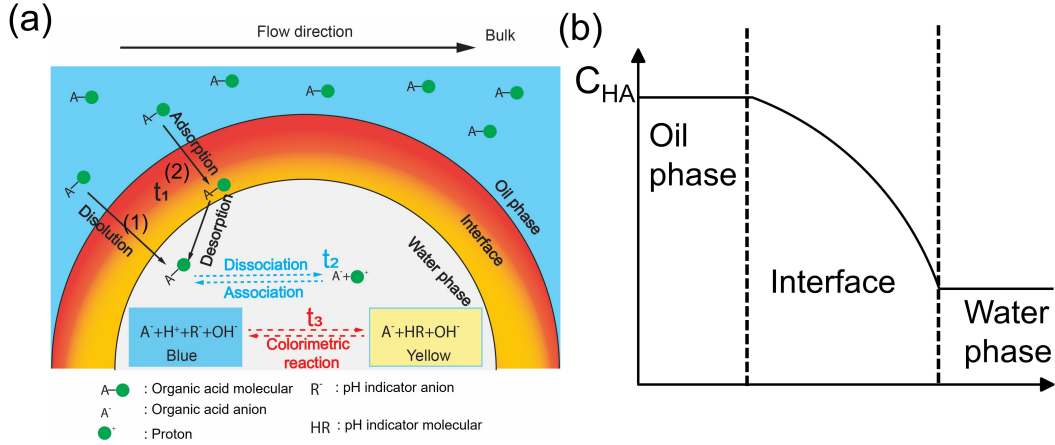
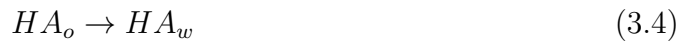


Figure 3.5: (a) Sketch of four steps in nanoextraction and colorimetric reaction in droplets. Acid molecules penetrated the oil-water interface by direct dissolution and surface adsorption-desorption (step 1:  $t_1$ ). Acid dissociated to release protons (step 2:  $t_2$ ). The protons react with the BG, leading to a color change (step 3:  $t_3$ ). The total time scale of the colorimetric reaction is the combination of those four processes ( $1/t=1/t_1+1/t_2+1/t_3$ ). (b) The concentration gradient of the acid at the interface.

at the rate of  $1/t_1$ : A fraction of acid ( $HA$ ) molecules dissolve into the aqueous droplets through partition. Those amphiphilic acid molecules may preferentially stay at the interface due to the interfacial adsorption. The mass transfer process can be expressed as:



(2) Dissociation at the rate of  $1/t_2$ : The acids adsorbed at the interface or dissolved in the droplets dissociate and form  $H^+$  and  $A^-$ . The dissociation rate is determined

by the intrinsic dissociation constant( $r_1$ ) of the acids at the droplet surface, which is a very fast. Here, the dissociation rate  $1/t_2$  can be expressed as  $\frac{d[H^+]}{dt}$ .



(3) Colorimetric reaction at the rate of  $1/t_3$ : In aqueous droplets, the pH indicator  $R^-$  in the droplets combines with  $H^+$  and converts to a product of HR. Here, the reaction rate  $r_2$  can be expressed as  $\frac{d[HR]}{dt}$ .



The influence from  $1/t_2$  and  $1/t_3$  is not evident at the high concentration of the solute in the surrounding phase, because the time is short for the acid concentration of the solute in the droplets to reach a level for decoloration. However,  $1/t_1$ ,  $1/t_2$  and  $1/t_3$  can not attribute to the rate-limiting step for decoloration at a low concentration of acid, because the decoloration is also much slower than the partition, as shown in Table 3.2. Once acid are extracted in water droplets, the dissociation and the protonization of the indicator can be completed on a timescale of less than 1 ms. The proposed interfacial enrichment of acids may explain both the long duration of decoloration and the high sensitivity of droplet decoloration to the acid at low concentrations. We noticed that the long duration of decoloration occurs for acids with a positive partition coefficient which is more concentrated in the surrounding octanol than in water droplets. There is a boundary layer with a concentration gradient of acids that is lower in water droplets, and higher in the oil phase in the external solution, as sketched in Figure 3.5b.

The concentration inside the droplet is regulated by the acid dissociation and reaction between protons and the indicator. The colorimetric reaction consumes the extracted acid, driving a net influx of the acid into the droplet. Such influx is slow, because the transfer through the interface of the droplets remains quasi-equilibrium. Therefore, step 1 is the rate-limiting step.

The above partition shifting of acids to the droplets could happen, as the liquid-liquid interface is permeable and dynamic. In the absence of chemical reactions (step 2 and 3) in droplets, the amount of molecules into the droplet is same as that of molecules out of the droplets at the equilibrium of partition. However, for reacting droplets, the fast chemical reaction through step 2 and then 3 cleans up the captured molecules quickly from the interface, so the droplets surface is adsorbed and reset to accommodate more acid molecules from the outside solution. The droplet decoloration can take place even if the concentration of acid in bulk is below the level predicted by pure partition, based on the solubilities in two phases.

Although not required, the interfacial activity of the acids may also contribute to the enhanced microextraction of the droplets. Several acids are like surfactants, accumulating at the droplet interface. Those amphiphilic acid molecules may preferentially stay at the interface, due to the interfacial adsorption. The transfer through the oil-water interface of the droplets remains at adsorption-desorption equilibrium.

### 3.3.5 Theoretical decoloration rate coupling interfacial partition and chemical reaction in droplets

At low concentration of acids, the reaction rate may not be simply neglected for acids. As discussed above, the chemical reaction may drive the extraction of the acid to the droplets.  $C_w(t)$  is expressed as:

$$\frac{dC_w(t)}{dt} = \frac{3}{R}\beta\left(\frac{C_o(t)}{p} - C_w(t)\right) + rC_w(t) \quad (3.7)$$

The first term on the right determines acid transfer (partition and interfacial transfer). The second term determines reaction in the droplets (acid dissociation and pH indicator protonation).

A reaction rate  $r$  of ( $r=r_1 \times r_2$ ) accounts for the effects from acid dissociation and chemical reaction in the droplets. Here,  $r_1$  represents the acid dissociation rate and

$r_2$  represents the reaction rates of acid and the indicator in droplet. Both  $r_1$  and  $r_2$  defined in Eq.3.5 and 3.6 are given by the acid dissociation and by the reactant in the droplets, respectively. Eq. 3.7 can be integrated to obtain the decoloration time  $t_{decoloration}$ , that is, the time for  $C_w(t)$  to increase from 0 to  $C_w^*$ . The fitting parameters are the apparent partition coefficient  $p^*$ , the reaction rate  $r$  and mass transfer coefficient  $\beta$ . The shift of distribution coefficient from  $p$  to  $p^*$  accounts for more acids extracted into the droplet to the level of  $C_w^*$ .

### 3.3.6 Rate-limiting step in droplet decoloration at low acid concentration

Eq.3.7 show good agreement with our measured decoloration time for all types of acids, although decoloration time varies clearly with the properties of acids. As shown in Figure 3.4a, the droplet decoloration becomes faster for more hydrophilic acid. For a given size of the droplet ( $R$  of  $25 \mu m$ ), the order of decoloration is acetic acid, gallic acid, n-butyric acid, PHBA, valeric acid and benzoic acids.

At the low acid concentration of 5 mM in Figure 3.4(b-d), the decolor time from the two long-chain alkyl acids (n-butyric acid and valeric acid) can be described by Eq. 3.7, as shown in Figure 3.6c. Here, the value of the fitting parameter apparent partition  $p^*$  is much lower than the intrinsic coefficient of the acid in octanol and water in the absence of chemical reactions. The other fitting parameter  $r$  is 0 from these two alkyl acids. Similar to surfactant, the hydrophilic part (carboxylic acid group) of these acids can penetrate the oil-water interface and stay in the water phase, while the hydrophobic component remains in the oil phase. The rates of acid dissociation (step 2) and colorimetric reaction (step 3) in the droplets are fast compared to interfacial transfer. So the second term on the left side of Eq. 3.7 can be neglected ( $r=0$ ). As for acetic acid, its solubility in water is much higher than in the surrounding.

Compared to water-less soluble valeric acid and butyric acid, aromatic acids have the less surface activities. Droplet decoloration from acetic acid and aromatic acid show good agreement with the prediction from Eq. 3.7. Different from  $r=0$  for valeric acid and butyric acid, a positive value of  $r$  was obtained in Eq. 3.7, as shown in Figure 3.6d. Park et al. demonstrated that the dissociation of acetic acid is a very fast process, completed in few picoseconds.[143] However, the effect from the reaction rate  $r$  on the decoloration time can be revealed in decoloration rate, possibly due to the fast partition process of acetic acid and aromatic acids in droplets. We also found that  $r$  decreases with  $C_o$ , as shown in Table 3.3, 3.4 and 3.5, suggesting less influence from chemical reaction in droplets and more solubility-dominated partition at higher  $C_o$ . The partition shifting happens to the droplets at low concentrations specific of acids. The apparent distribution  $p^*$  obtained at all concentrations, is shown in Figure 3.6 a and b. The revers of  $p^*$  represents the concentration in droplets over that in the surrounding. As the acid concentration decreases, the partition shifting ( $p/p^*$ ) becomes more significant. Up to 11 times larger  $p^*$  was found for butyric acid at  $C_o=1$  mM in Figure 3.6.  $p$  and  $p^*$  become the same at high concentrations of acids, for example, at 2.5 M for heptanoic, and 100 mM for benzoic acid and PHBA, 50 mM for other acids.

### 3.3.7 Acid specificity of mass transfer coefficient $\beta$

The mass transfer coefficient ( $\beta$ ) shown in Figure 3.6c mainly reflects the rate of the acid crossing the interface. We found that  $\beta$  is independent of the concentration in the oil phase ( $C_o$ ) for a given acid. But for different acids, expect heptanoic acid,  $\beta$  increases with the distribution coefficient  $p$ . As shown in Figure 3.6c, possibly acids with a lower distribution coefficient ( $p$ ) established as lower the acid concentration gradient between the droplet and the surrounding for a slow transfer of the acid. The interfacial activity of the acid also influences the transfer coefficient  $\beta$ . At the

Table 3.3: Mass transfer coefficient ( $\beta$ ), reaction coefficient (r) and apparent distribution constant ( $p^*$ ) of acetic acid and aromatic acid at the concentration ( $C_o$ ) of 0.5 mM to 5mM in the octanol solution.

| $C_o$ (mM) | Parameters | Acetic acid | Gallic acid | PHBA  | Benzoic acid |
|------------|------------|-------------|-------------|-------|--------------|
| 0.5        | $\beta$    | 0.55        |             |       |              |
|            | r          | 0.005       |             |       |              |
|            | $p^*$      | 0.3         |             |       |              |
| 1          | $\beta$    |             | 0.45        |       |              |
|            | r          |             | 0.01        |       |              |
|            | $p^*$      |             | 1.2         |       |              |
| 5          | $\beta$    | 0.55        | 0.45        | 1.2   | 1.3          |
|            | r          | 0.01        | 0.03        | 0.001 | 0.001        |
|            | $p^*$      | 0.67        | 4.5         | 5.2   | 12           |

Table 3.4: Mass transfer coefficient ( $\beta$ ), reaction coefficient (r) and apparent distribution constant ( $p^*$ ) of acetic acid and aromatic acid at the concentration ( $C_o$ ) of 50 mM to 100 mM in the octanol solution.

| $C_o$ (mM) | Parameters | Acetic acid | Gallic acid | PHBA | Benzoic acid |
|------------|------------|-------------|-------------|------|--------------|
| 50         | $\beta$    | 0.55        | 0.45        | 1.2  | 1.3          |
|            | r          |             |             |      |              |
|            | $p^*$      | 0.67        | 5.01        | 25   | 60           |
| 100        | $\beta$    |             |             | 1.2  | 1.3          |
|            | r          |             |             |      |              |
|            | $p^*$      |             |             | 38   | 74           |

Table 3.5: Mass transfer coefficient ( $\beta$ ), reaction coefficient (r) and apprent distribution constant ( $p^*$ ) of long-chain alkyl acid at the concentration ( $C_o$ ) in octanol solution.

| $C_o$ (mM) | Parameters | N-butyric acid | Valeric acid | Heptanoic acid |
|------------|------------|----------------|--------------|----------------|
| 1          | $\beta$    | 0.7            |              |                |
|            | $p^*$      | 0.54           |              |                |
| 5          | $\beta$    | 0.7            | 3            |                |
|            | $p^*$      | 1.8            | 2.9          |                |
| 50         | $\beta$    | 0.7            | 3            | 0.55           |
|            | $p^*$      | 6.2            | 24.5         | 37             |
| 500        | $\beta$    |                |              | 0.55           |
|            | $p^*$      |                |              | 120            |
| 2500       | $\beta$    |                |              | 0.55           |
|            | $p^*$      |                |              | 243            |

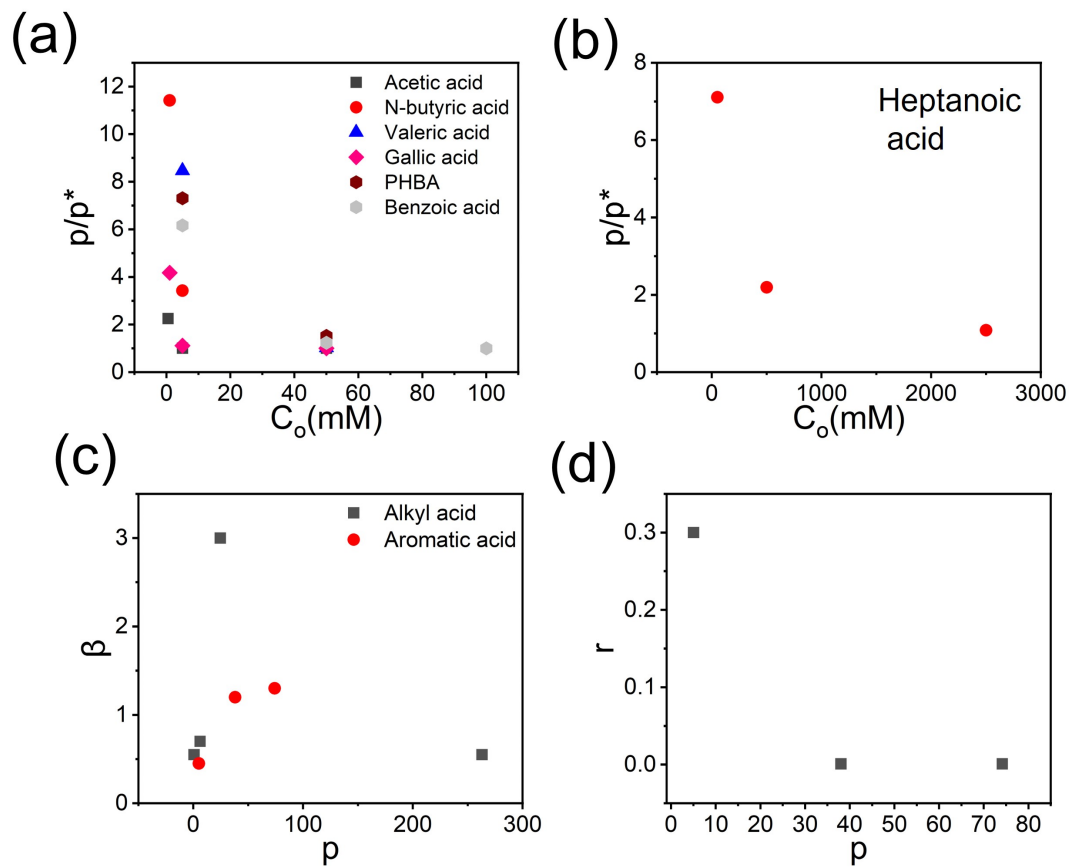


Figure 3.6: Distribution coefficient shift down with the decrease in the acid concentration in oil ( $C_o$ ) for heptanoic acid (b) and other acids(a), respectively. (c)  $\beta$  from the fitting of Eq.3.1 at high concentration as a function of  $p$  for alkyl and aromatic acids. (d)  $r$  from the fitting of Eq.3.7 at 5 mM as a function of apparent distribution coefficient ( $p^*$ ) for aromatic acids.

same  $p$ , the coefficient  $\beta$  of aromatic acids with lower interfacial activity is lower than that of alkyl acids. On the other hand, the long hydrophobic chain in the heptanoic acid molecule makes it much more likely to stay on the oil phase than in water droplets. Hence, transferring heptanoic acid into water droplets becomes energetically unfavorable, leading to a very low  $\beta$ .

### 3.3.8 Effects of reactant concentration in droplets on reaction rates

In the above, the concentration of the BG in the droplets was the same in all of the experiments (0.02 g/ml in solution A). Considering the crucial role of chemical reactions in the droplets for acid detection, another important parameter to influence the detection sensitivity is the concentration of BG in the droplets. We varied the pH indicator concentrations by changing the concentration of BG in solution A. After the formation of the droplets by solvent exchange, a higher concentration of BG showed a darker color (lower color intensity), as shown in Figure 3.7a. We used benzoic acid as the model analyte to measure the LoD under different BG concentrations in solution A. The results in Figure 3.7b demonstrates that a higher concentration of BG had a higher LoD.

Higher sensitivity (lower LoD) in a lower concentration of BG in the droplets is attributed to a shorter time to reach the critical concentration. The decoloration of the droplets is determined by the ratio of the concentration of  $HR$  and  $R^-$  ( $\frac{[HR]}{[R^-]}$ ), as shown in the Eq.3.6. As the  $[R^-]$  increased when the BG concentration increased in the droplets, the amount of the  $HA$  for droplets to accomplish the decoloration is also increased.

More  $HA$  molecules need a longer time to reach the critical concentration. When the concentration of the  $HA$  increases, the reaction rate ( $r_2$ ) also increases. However, compared to the reaction rate, the acid dissociation rate ( $r_1$ ) is faster.[143] Considered

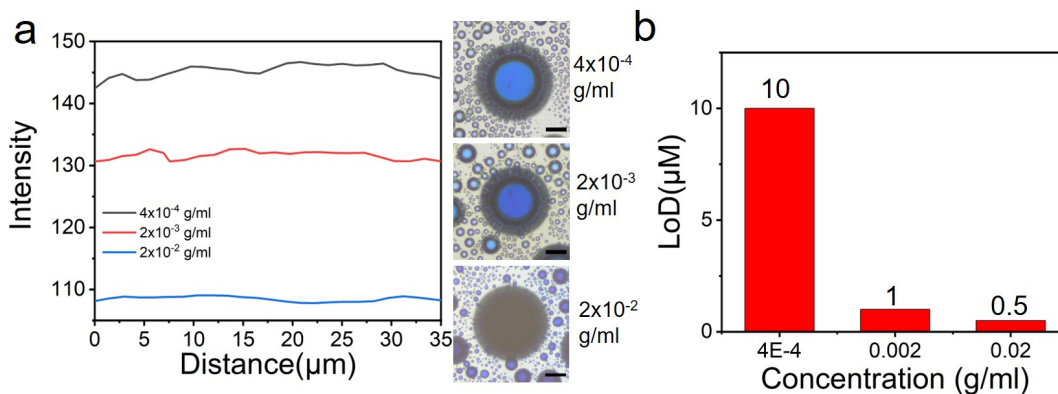


Figure 3.7: The initial color intensity along droplet diameter and the images (a) and the limit of detection (LoD) (b) for benzoic acid. The droplets were formed by solution A containing BG at the concentration of 0.02 g/ml, 0.002 g/ml and 0.0004 g/ml. Scale bar: 25  $\mu m$ . Here the distance of 0 means the edge of the droplets.

the organic acids used in this work are weak acid and thus the acid dissociation is partial, more acid molecules accumulated in the droplet. Those redundant HA molecules slow down the mass transfer rate due to the decreases of the driven force ( $C_o - C_w$ ).

### 3.4 Conclusions

This work experimentally and theoretically investigates the rate and efficiency of integrated extraction and detection of analytes in surface nanodroplets. Seven acids were used as the model analytes, and the extraction of the acid was coupled with a colorimetric reaction in surface nanodroplets. We found a significant shift in the partition of the acids into the reacting droplets at a low concentration of acid in the external solution. The interfacial partitioning of the acids was proposed to be the rate-limiting step in integrated extraction and detection, and meanwhile contribute to the highly sensitive detection from the shifted partition of the acids. The pro-

posed theoretical model for the extraction process that takes the partition shift into consideration is in good agreement with experimental results. This work provides a comprehensive analysis for the enhance of extraction and sensitive colorimetric detection in nanodroplets.

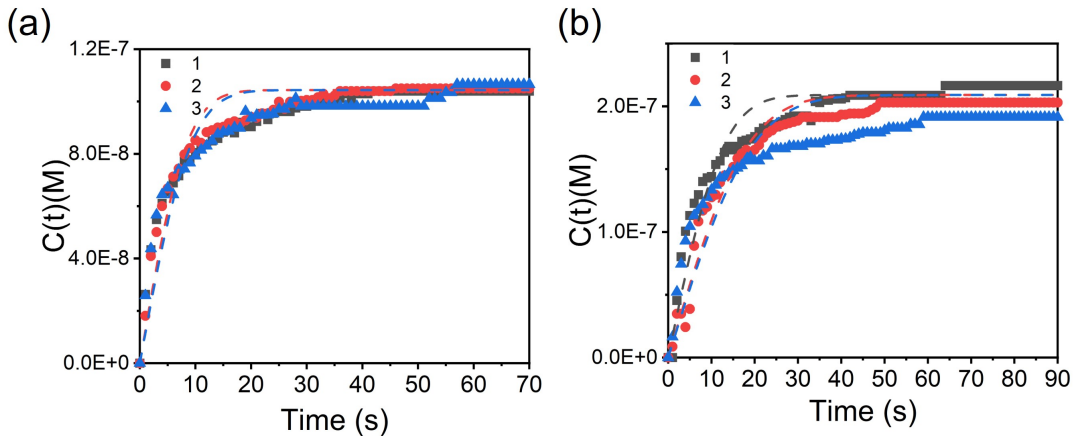


Figure 3.8: Error function fitting (dotted line) of the fluorescence intensity that increases from time 0 at the dye concentration of  $5 \times 10^5 g/L$  (a) and  $1 \times 10^4 g/L$  (b).

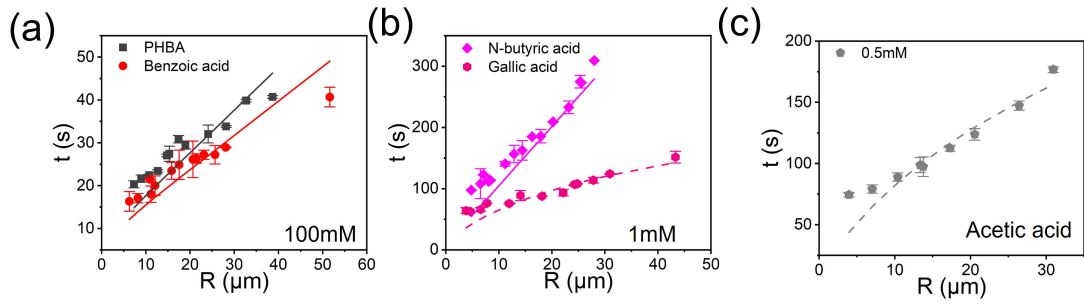


Figure 3.9: The plot of droplet decolor time as a function of droplet size after injecting oil containing 100 mM of PHBA and benzoic acid (a), 1 mM of n-butyric acid and gallic acid (b) and 0.5 mM of acetic acid (c). The solid line is fitted from Eq.3.3. The dash line is fitted from Eq.3.7.

# Chapter 4

## In-situ fabrication of metal oxide nanocaps based on biphasic reactions with surface nanodroplets

### 4.1 Introduction

Surface-bound nanomaterials are key components in many clean energy techniques from lithium batteries, solar absorber,[144] solar-driven interfacial evaporation in desalination [145–147], photocatalytic reactions,[148, 149] to wastewater treatment and environment remediation by photolysis [150, 151]. Maximizing the performance and functionalities of the materials requires control of spatial distribution and coverage of nanomaterials deposited on a supporting substrate. Exploration of small reactive droplets on surfaces represents a novel strategy for the fabrication of surface-bound nanomaterials. Reactions with droplets on surfaces potentially streamline the process of synthesis and immobilization of surface-bound nanomaterials to obtained desired

spatial arrangement, surface coverage and materials nanostructures. Recent research has demonstrated the high reactivity of small droplets with possible 1-million time enhancement in reaction rates, compared to the bulk counterpart [29]. However, it remains to be explored how to mediate the reactions between droplets and the bulk surrounding and to establish simple and effective routes for the fabrication of surface-bound nanomaterials.

Small-sized droplets allow the reactant to be compartmentalized at high concentration and fast mass transfer rate from the surrounding phase [29, 40]. The large surface area of the droplets provides more space for the chemical reaction that needs access to reactants in both droplets and the surrounding phase. The asymmetric local environment on the droplet surface provides active sites for biphasic chemical reaction [29, 83], or nucleation and growth of new phases [131, 152]. The asymmetric local environment refers to the interface between the droplet and the surrounding environment. Compared to current techniques developed for selective deposition of metal oxide nanomaterials including direct growth, chemical bonding, electrostatic adherence, or seeding on selectively activated areas [153–156], droplet reactions are especially effective for material synthesis from chemical reactions between reactants dissolved in immiscible organic and inorganic phases [29].

Droplet-based synthesis approaches are endorsed by controlled formation of surface nanodroplets that are liquid droplets on a solid surface in contact with an immiscible surrounding liquid [83, 152, 157]. Here *nano* refers to the height of these droplets that range from tens to a few hundred nanometers. Specifically, the solvent exchange is the fast and straightforward solution-based process for forming surface nanodroplets. [66] Without complex dynamics in evaporating droplets [158–160], the formation of surface nanodroplets can be tuned by the solution, flow and surface conditions. [66, 142] Solvent exchange is flexible for the types of substrates, applicable for droplet formation on planar substrates with or without micropatterns, microfibers and even curved wall of microcapillary tubes [81, 161].

Complementary to those droplets flowing in microfluidic channels, surface nanodroplets are stabilized by the substrate. Hence a reactant solution in a flow can be introduced to react with nanodroplets without leading to the uncontrolled collision, coalescence or Ostwald ripening. Reactions between nanodroplets and the reactants in the flow can be leveraged to synthesize surface-bound materials through sequential reactions. As a demonstration, silver nanoparticles were synthesized on droplet surface for fast extraction and sensitive chemical detection.[85]

Up to now, limited studies are available on surface nanodroplets for the synthesis of surface-bound metal oxide. As a common and low-cost photocatalyst with various potential polymorphic characteristics,  $\alpha\text{-Fe}_2\text{O}_3$  has been widely used in photocatalytic reactions, [162] with advantages in narrow band-gap and high efficiency of absorption up to 40% of the solar spectrum in the visible range.[163, 164] In established protocols, iron oxide-based nanomaterials can be adjusted by varying bottom-up synthesis approaches such as hydrothermal, solvothermal, co-precipitation and many others.[165–168] Iron salt of organic acid, especially iron oleate, is prominently used as precursors in synthesizing nanocrystalline iron oxide-based nanoparticles.[169–172] The external conditions, such as temperature, pressure and among others, are responsible for the secondary noncrystalline phase during the thermal decomposition.[168, 173]

In this work, we will take iron oxide as a typical example to demonstrate a simple approach for the in-situ fabrication of surface-bound nanocaps of a range of metal oxides. By our method, oleic acid nanodroplets with desired number density and location are preformed over a solid substrate inside a flow chamber. A flow of iron salt solution is introduced to react with nanodroplets and produce nanocaps of certain spatial arrangement and surface coverage. Moreover, we will show that the composition of nanodroplets can be varied to mediate the nanostructures of the caps and create nanopores along the cap surface. Beyond iron oxide nanocaps, our approach can also be applied to the synthesis of other metal oxides including copper oxide, zinc oxide and yttrium oxide. Our work demonstrates the feasibility of reactive sur-

face nanodroplets as a novel route for in-situ synthesis of surface-bound metal oxides. The prepared nanocaps may be optimized for photodegradation of organic materials in water as demonstrated in this work, and also for optical focusing, plasmonic resonance and among other applications.

## 4.2 Experimental section

### 4.2.1 Chemicals and materials

Ethanol (90 %), octadecyl trichlorosilane (OTS, 98.9 %), oleic acid (90 %), 1-octanol (95 %) and decane (99 %) were purchased from Fisher Scientific (Canada). While iron (III) chloride (97 %), copper acetate (98 %), yttrium acetate (99 %) and zinc oxide (98 %) was purchased from Sigma-Aldrich (Canada). Water was obtained from a Milli-Q water purification system (MA, USA). OTS-coated cover glass (Fisher scientific) and silicon wafer (University wafer, USA) were used as the substrate. The coating of OTS was prepared by following the protocol reported in the literature.[64]

### 4.2.2 Preparation of metal oxide nanocaps on a substrate

Nanodroplets of oleic acid were produced on a substrate placed in a narrow fluid chamber. The detailed procedure of solvent exchange, as shown in Figure 4.1a, has been introduced in earlier work.[83]. The fabrication methodology of these surface nanocaps is sketched in Figure 4.1a and b. In the beginning, a ternary solution (Solution A) with volume ratio as ethanol: water: oleic acid (70:30:3.5) filled the chamber. Oleic acid droplets formed on the OTS-coated surface after injecting water (solution B) at a flow rate of 20 ml/hr in step 1. Subsequently, in step 2, Solution C of 0.04 M iron chloride aqueous solution flowed into the fluid chamber at 15 ml/hr. The droplets of oleic acid react with the iron cation in the flow, forming iron oleate

and the complexes droplets over the substrate, as shown in Figure 4.1b. The reaction for the formation of iron oleate is shown in Eq.4.1. Finally, in step 3, water at a flow rate of 40 ml/hr flowed into the chamber for 5 minutes to remove excessive unreacted precursors. The substrate was taken out from the fluid chamber after the reaction and then annealed in an oven at different temperatures and environmental conditions as listed in Table 4.1.



The preparation process for copper oxide, yttrium oxide and zinc oxide is similar to that of iron oxide nanocaps. The only difference is that solution C (precursor solution) changes to 0.04 M copper acetate, 0.04 M yttrium acetate or 0.04 M zinc acetate, respectively.

### **4.2.3 Preparation of porous iron oxide nanocaps from binary droplets**

For the preparation of the porous iron oxide nanocaps, 1-octanol and decane were used as the secondary oil phase, respectively. The ratio of water, ethanol and oil in solution A is the same as above. However, the oil phase here is a mixture of oleic acid and another oil. In the mixture of oleic acid and the secondary oil, the volume ratio is 2:1.5 for oleic acid and octanol and 2.2:0.3 for the oleic acid and decane. The ternary phase diagram of three oils is shown in Figure 4.1c and d. The ratio of the oils in surface droplets after the solvent exchange is based on the integrated area between the dilution path and the binodal curve in the Ouzo region, as explained in previous work.[74]

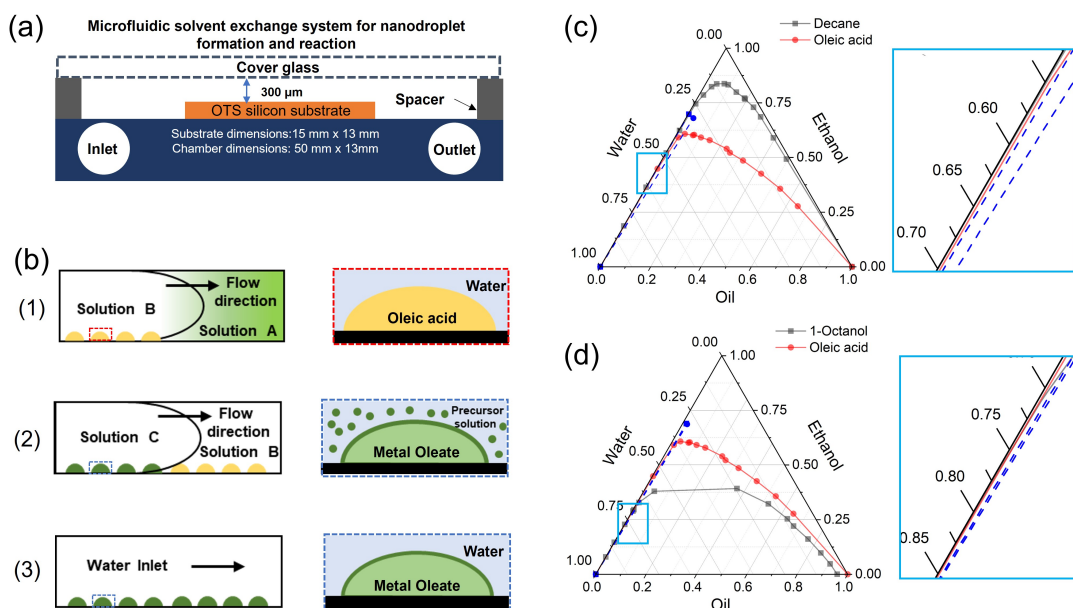


Figure 4.1: Brief sketch of the fluid chamber (a) and surface nanodroplets formation and reaction in the fabrication of nanocaps of iron oleate (b). Solution A: ternary solution of ethanol, water and oleic acid. Solution B: water. Solution C: precursor solution. (c) and (d) are ternary phase diagrams of ethanol, water and oil mixtures and the enlarge images of the ouzo region. Here, the red lines represent oleic acid. While gray lines represent decane (a) and 1-octanol (b), respectively. The blue lines represent the dilution path during the solvent exchange process as the dilution path penetrates the solubility line of the oil. oil droplets form due to the over-saturation.[66] Ternary diagram of oleic acid is reproduced from [Li et al. *J. Phys. Chem. C*. 125, 28, 2021, 15324–15334.]. Copyright [2021] American Chemical Society. Ternary diagram of 1-Octanol is reproduced from [Arce et al. *J. Chem. Eng. Data*. 39 (2), 1994, 378-380.]. Copyright [1994] American Chemical Society. Ternary diagram of decane is reproduced from the IUPAC-NIST solubility database.

#### 4.2.4 Characterization of size and structures of metal oxide nanocaps

Optical images were obtained using an upright optical microscope (NIKON H6001) coupled with a 10X and 100X lens. A scanning electron microscope (SEM, HITACHI S4800) and atomic force microscope (AFM, Bruker) were used to characterize the surface morphology of the samples. The cross-section of the samples was characterized by a helium ion microscope (Zeiss Orion NanoFAB with Ga FIB). X-ray photoelectron spectroscopy (XPS, Kratos AXIS Ultra) was used to analyze the element and the crystalline state of the samples. The peaks in XPS spectra were analyzed by OriginLab. The TEM characterization was performed by using Hitachi H-9500 Environmental Transmission Electron Microscope (ETEM). An accelerating voltage of 300 kV was applied for the characterization. The selected area electron beam diffraction (SAED) technique was employed for phase identification. The simulation of the SAED pattern was carried out by using Desktop Microscopist (DM). The simulation of high resolution TEM image was then performed by using MacTempasX (Total Resolution).

The nanocaps were prepared on a SiN window (Norcada, Canada) for the imaging of TEM. The dimension of the SiN was 0.05 mm  $\times$  0.05 mm. The SiN window was directly used as the substrate in our fluid chamber, where the surface nanodroplets of oleic acid surface nanodroplets were formed and then reacted with the iron precursor. Iron oleate droplets on the SiN window were heated in air at 500 ° for 2 hr, respectively. After the samples were cooled down to room temperature, the samples were put into a TEM chamber.

The cross-section images of iron oxide nanocap that was heated at 500°C in air for 2 hr were obtained by FIB-HIM (Zeiss Orion NanoFAB with Ga FIB). A high-energy beam of Ga ion that is perpendicular to the substrate was used to mill the nanocap. Half of the nanocap was milled and from the top view, semicircular of the naoncap

Table 4.1: Experimental conditions for fabrication of metal oxide nanocaps.

| Metal   | Precursor       | Heating temperature | Heating time | Mark |
|---------|-----------------|---------------------|--------------|------|
| Iron    | $FeCl_3$        | 75 °C               | 0.5 hr       | I    |
|         |                 | 300 °C              | 0.5 hr       | II   |
|         |                 |                     | 2 hr         | III  |
|         |                 | 500 °C              | 0.5 hr       | IV   |
|         |                 |                     | 2 hr         | V    |
| Copper  | $Cu(CH_3COO)_2$ | 300 °C              | 2 hr         | NA   |
| Yttrium | $Y(CH_3COO)_3$  | 500 °C              | 2 hr         | NA   |
| Zinc    | $Zn(CH_3COO)_2$ | 300 °C              | 2 hr         | NA   |

remains on the substrate. Then the cross-section of the nanocap appears after the milling by FIB. In order to obtain the thickness of the nanocap, the stage was tilted by 57° from the top view, leading to an elliptical view of the spherical shape. The sketch of the FIB process is shown in Figure 4.9.

#### 4.2.5 Photodegradation catalyzed by iron oxide nanocaps

Photodegradation of model compounds methyl orange (MO) was performed in a flow chamber, similar to our chamber for performing solvent exchange process. The

chemical structure of the model compounds and the degradation path are shown in Figure 4.10. Glass substrate decorated with iron oxide nanocaps was used as the top plate. The channel height of the fluid chamber was kept at  $150 \mu m$ . The solution of MO (5 mg/l) was continuously injected into the chamber, controlled by a syringe pump at a constant flow rate of 1 ml/hr. It took 45 minutes for injected MO solution to pass the fluid chamber. The fluid chamber was exposed to  $21.6 W/m^2$  intensity of the simulated solar light. The exposure time of the solution was also 45 minutes. To avoid the adsorption of the dye molecule by the porous structure, we discarded the first 1 ml of the photo-illuminated liquid. The treated solution was collected and characterized by a UV-vis spectrometer (Varian Cary 50). The efficiency of the photodegradation is defined as:

$$E = \frac{(Abs_{before}) - (Abs_{after})}{Abs_{before}} \quad (4.2)$$

Here, E is the efficiency of degradation.  $Abs_{before}$  and  $Abs_{after}$  are the UV absorbance of MO solution at the peak of 464 nm before and after the photodegradation, respectively.

In order to evaluate the efficacy of the different nanocaps, we normalized the efficiency by the surface coverage of nanocaps:

$$E_n = \frac{(E_{cap}) - (E_{glass})}{S} \quad (4.3)$$

Here,  $E_{cap}$  refers to the degradation efficiency by using the nanocaps-decorated top plate. While  $E_{glass}$  refers to the degradation efficiency by using bare glass as the top plate. S is the surface coverage of the nanocaps.

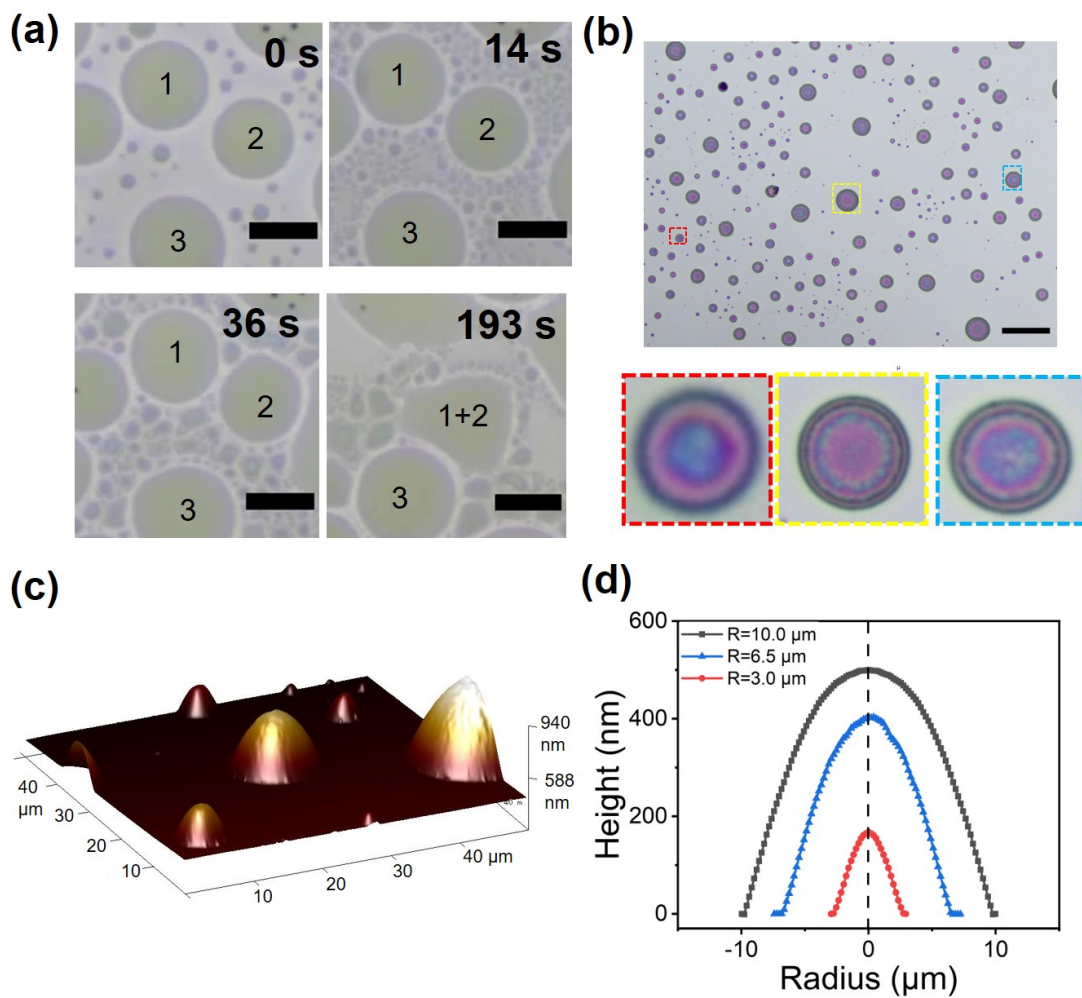


Figure 4.2: (a) Optical images of surface nanodroplets during the reaction at 0 s, 14 s, 36 s and 193 s. (b) Iron oxide nanocaps on the substrate. (c) Morphology of the nanocaps obtained by AFM after heating at 500°C for 2 hours in air. (d) The height profiles of the nanocaps from AFM reveal that the contact angle of the nanocaps around 7°. Length of scale bare: 20  $\mu m$  in (a) and 50  $\mu m$  in (b).

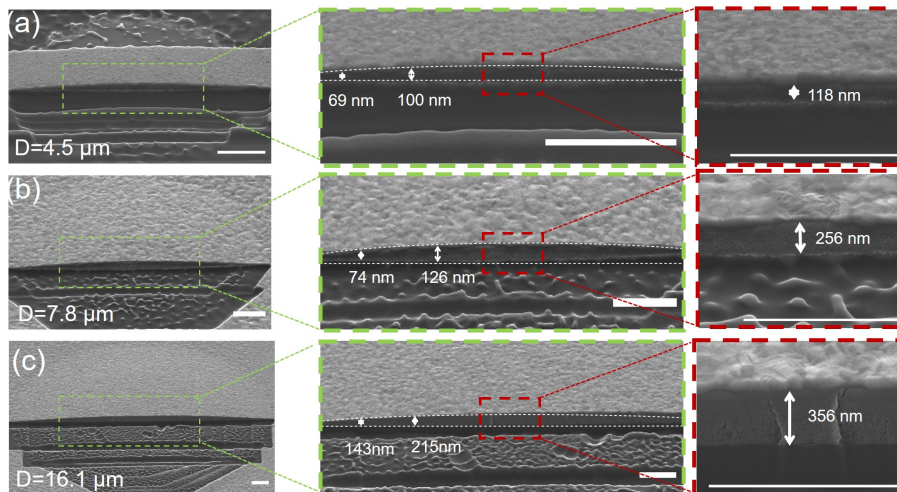


Figure 4.3: Images of three nanocaps milled by focused ion beam at diameter of (a)  $4.5 \mu m$ , (b)  $7.8 \mu m$  and (c)  $16.1 \mu m$ . The images on the left were taken at  $57^\circ$  from the normal plan to the substrate. Length of the scale bar:  $1 \mu m$ .

## 4.3 Results and discussion

### 4.3.1 Formation and morphology of iron oxide nanocaps

Surface nanodroplets of oleic acid were produced by using the solvent exchange process. The droplet size was controlled from a few to tens of  $\mu m$  in lateral radius ( $R$ ). The flow of iron chloride aqueous solution was injected into the chamber to react with surface nanodroplets.

Droplets change the shape during reaction with iron cation as shown in Figure 4.2a. Initially, at  $t=0$  s just after the injection of iron chloride solution, oleic droplets have no significant change. Further proceedings of the reaction at  $t=14$ s, a boundary rim was developed around the bigger surface droplets and some small droplets were formed on the space area. Splitting of the reactive droplets may be due to interfacial tension stress induced by heterogeneous distribution of chemical species on the droplet surface.[174] After a specific time interval, the tiny droplets expanded and

merged into larger droplets. Finally, at 193 s, some adjacent droplets merged while other droplets still remained as individuals, but all droplets assumed spherical cap shape eventually.

At the completion of the droplet reaction, the substrate with iron oleate droplets was taken out from the chamber and heated at elevated temperatures. The final products appear to be semitransparent with colorful Newton rings clearly visible in optical images, as shown in Figure 4.2b. The semitransparent suggests the ultra-thin structure of the product after heating. Cross-sectional profiles of three structures were obtained from the AFM images in Figure 4.2c and d. These structures have the shape of spherical caps with an apex less than  $1 \mu\text{m}$  even for the exceptionally large one. The height of the structure in Figure 4.2 ranges from 164 to 500 nm and the lateral diameter from 5.4 to  $19.6 \mu\text{m}$ , with a contact angle around  $7^\circ$ . Following the naming convention of surface nanodroplets, we refer to these structures as nanocaps. The surface coverage of oleic acid droplets was 40% before the reaction and decreased to 11% after heating. The shrinkage at elevated temperature is due to decomposition of iron oleate ( $Fe(C_{18}H_{33}O_2)_3$ ) to iron oxide ( $Fe_2O_3$ ). The mass loss from thermal decomposition is around 91% based on simple elemental analysis. The size distribution of surface droplets also changed after the heating process, as shown in Figure 4.11. The surface nanodroplets are dominated at the diameter of 1 to  $2 \mu\text{m}$ . The nanocaps are most at the diameter of 3 to  $4 \mu\text{m}$  with a thickness of 180 to 270 nm. When the surface oleic acid reacts with the iron precursor, the droplets are expanded, as shown in Figure 4.2a. Some small droplets merge together to form a larger droplet. While other small droplets disappear during the heating due to the shrinkage. This phenomenon is why the most probable size of the nanocaps is larger than that of oleic acid droplets.

The surface coverage of nanocaps can be varied by conditions from the formation of surface nanodroplets. Larger surface nanodroplets with a large interval of each other formed larger nanocaps with low surface coverage after reaction and heating,

as shown in Figure 4.12.

The inner structure of the nanocap was analyzed by using FIB that can mill half of the nanostructures. The cross-section of the nanocap is exposed along the central line. As shown in Figure 4.3, the nanocaps of all sizes have a homogeneous filled inner structure. Such internal structure indicates that the reaction was not limited to the droplet surface. Oleic acid inside the droplet was also converted to oleate by reacting with an iron precursor in the solution. Meanwhile, the nanocaps with the diameter from 4.5  $\mu\text{m}$  to 16.1  $\mu\text{m}$  are from 118 nm to 356 nm in height, which is consistent with the previous AFM profiles showing the contact angle of the nanocaps.

The morphology of the nanocap suggests that the reaction between iron precursors and oleic acid droplets is not only happened at the interface but within the whole droplet. Specifically, the carboxyl group of oleic acid reacts with the iron cation at the droplet surface, which results in the formation of iron oleate,  $Fe(C_{18}H_{33}O_2)_3$ . During the reaction process, the -OH group of the oleic acid was replaced by O-Fe. The formed iron oleate may diffuse inside of the droplet. The fresh oleic acid molecules move to the interface, leading to a continuous reaction. The reaction occurs from the water-oil interface and then extends to the whole droplet within a few minutes when the droplets stopped deformation.

### 4.3.2 Effect of time and temperature of heating

Figure 4.4 shows the XPS spectra of oleate droplets and nanocaps treated at different heating temperatures and times. Iron oleate remains in the liquid state until 80°C without decomposition.[183–185]. The peaks of Fe 2p, O 1s and C 1s listed in Table 4.2 and 4.3 are compared to distinguish the chemical states of the products.

The deconvolution of  $Fe2p$  spectra resolves the peaks at 715.6 eV, 726.6 eV and 734.3 eV due to the presence of  $Fe^{3+}$  states within the iron oleate complex. The presence of

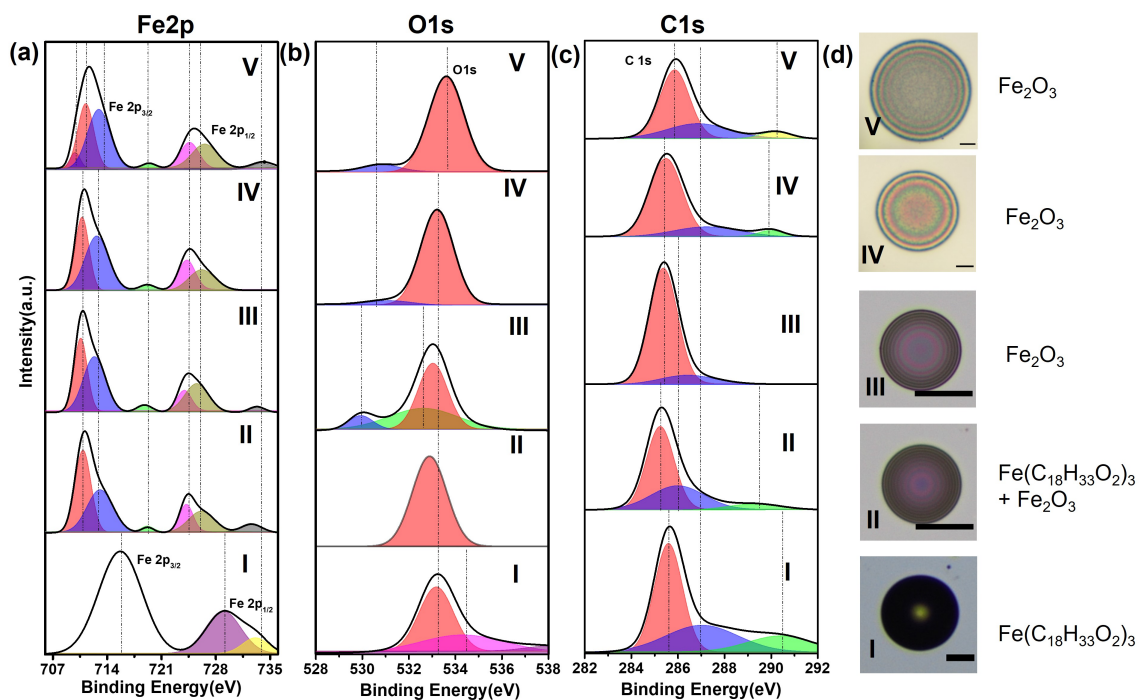


Figure 4.4: XPS spectra of the surface droplets after various heating process. (a) Iron *Fe2p* spectra (b) Oxygen *O1s* spectra (c) Carbon *C1s* spectra. Black solid line is cumulative observed values of binding energy for each element. Filled area under different colours denotes deconvoluted peaks during peak fittings. (d) Optical images of nanocaps after different heating process. Treatment conditions I-V are listed in Table 4.1. Length of scale bar: 15  $\mu m$ .

Table 4.2: XPS peaks of Fe2p

| Peak location(eV)   | Indicated component                  | Treatment conditions |
|---------------------|--------------------------------------|----------------------|
| 715.6               | $Fe^{3+}2p_{3/2}$ [175]              | I                    |
| 726.6               | $Fe^{3+}2p_{1/2}$ [176]              | I                    |
| 734.3               | $Fe^{3+}2p_{1/2}$ satellite[176]     | I-V                  |
| 710.9, 713.2        | $Fe^{3+}$ octahedral[177]            | II, III              |
| 724.5               | $Fe^{3+}2p_{1/2}$ in $Fe_2O_3$ [177] | II-V                 |
| 709.9, 711.3, 713.0 | $\alpha - Fe_2O_3$ [175]             | IV, V                |
| 719                 | $Fe_2O_3$ [177, 178]                 | II-V                 |

Table 4.3: XPS peaks of O1s and C1s

| Peak location(eV) | Indicated component | Treatment conditions |
|-------------------|---------------------|----------------------|
| 533.3-533.8       | $SiO_2$ [179]       | I-V                  |
| 530.8             | Oxide species[180]  | IV, V                |
| 285.1             | Alkyl chains[177]   | I, II                |
| 287.0             | C-O bound[181]      | I, II                |
| 290.5             | C (carboxyl)[182]   | I                    |

$Fe^{3+}$  in the complexes is attributed to the reaction between  $FeCl_3$  and the droplets of oleic acid. [186, 187].

The binding energy of oxygen for  $O1s$  at the peak of 533.3 eV is assigned to  $SiO_2$  of the substrate.[179] XPS peak for carbon ( $C_{1s}$ ) at  $\sim 285.1$  eV indicates the existence of alkyl chain in oleate,[177] while the peak of 287.0 eV is attributed to C-O bond[181] from the oleate. The peak at 290.5 eV is assigned to carboxyl carbon in organic acid.[182] Single carbon-oxygen (C-O) and carboxyl carbon are present in both oleic acid and iron oleate complex.

As the heating temperature increased to 300°C at 0.5 hr and 2 hr, iron oleate droplets solidified as shown in Figure 4.4d-II and III. XPS analysis of heated droplets at 300°C shows that presence of  $Fe_2O_3$  instead of  $Fe_3O_4$  [177, 178]. The peaks of 285.1 eV and 287.0 eV, as explained above, originate from the iron oleate, possibly due to the incomplete decomposition of the iron oleate during heating to 300°C at both 0.5hr and 2 hr.[186, 188]

The XPS analysis above suggests that the decomposition of iron oleate started at 300 °C.



when the heating temperature increased to 500 ° at 0.5 hr and 2 hr, we observed the formation of iron oxide ( $\alpha - Fe_2O_3$ ) phase nanocaps after 2 hr, as shown in Figure 4.4d-IV and V. XPS analysis of the heated substrate at 500° for 2 hr confirms the appearance of  $\alpha - Fe_2O_3$  phase. Here the analysis of XPS spectra shows that heating at 500°C provides sufficient temperature for the formation of iron oxide from the iron oleate complex. The formation of the  $\alpha - Fe_2O_3$  can be further confirmed by TEM and simulation.

To further confirm the formation of  $\alpha - Fe_2O_3$  after heating at 500°C for 2 hr. TEM and its simulation were used. Regions with deep contrast are emerged in the nanocap, as shown in Figure 4.5a. The corresponding SAED exhibits a spot-like feature of the typical crystalline phase, as shown in Figure 4.5b. The simulation of the SAED pattern in Figure 4.5b suggests that  $\alpha - Fe_2O_3$  formed. The reflection spots circled are related corresponding to the labeled dots in the SAED simulating pattern. Close check the diffraction pattern finds that instead of a sharp, well-defined circular shape, the reflection spots are stretched into the curved shape. This depicts the formed  $\alpha - Fe_2O_3$  possesses a certain extent of texture.

Usually, the driving force for crystallization is mainly due to dislocation, grain boundary energy, surface energy and strain energy or their combinations. During the crystallization process, a texture structure can form. It is well known that surface energy plays an important role in the formation of texture structures. In the study of Stirner et al about the surface energy of  $\alpha - Fe_2O_3$ [189], they found that the surface energy decreased in a sequence of  $\{01\bar{1}2\} < \{0001\} < \{11\bar{2}0\} < \{10\bar{1}0\} \approx \{10\bar{1}1\} < \{11\bar{2}6\} < \{10\bar{1}2\}$ . The  $\{10\bar{1}1\}$  shown in the current study (see Figure 4.5b) is at a position of high surface energy in the sequence. We postulate that the surface energy does not play the main role in the texture formation mechanism; rather, strain energy has

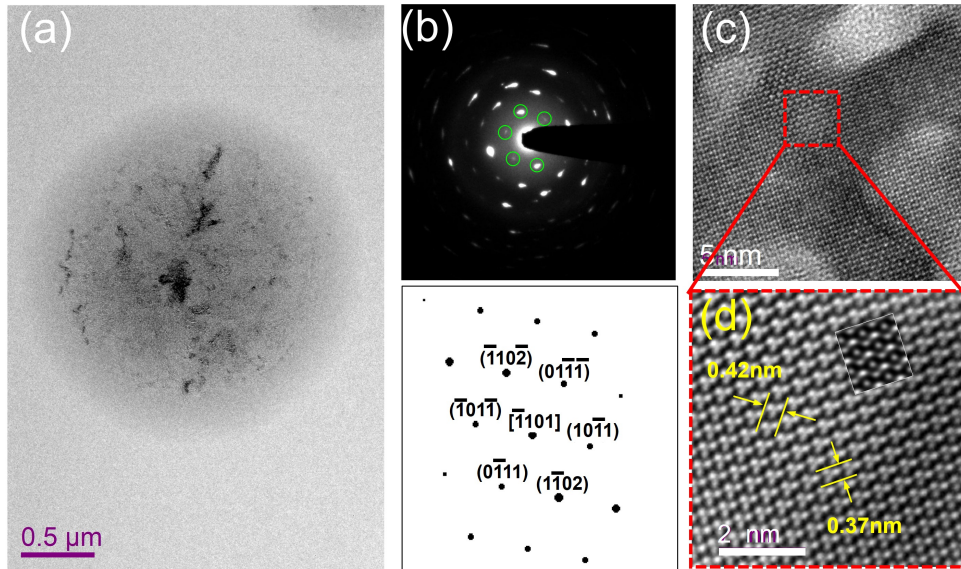


Figure 4.5: (a) TEM images of nanocaps heated at 500° for 2 hrs. (b) The corresponding selected-area electron beam diffraction (SAED) pattern image together with its simulation. (c) The high-resolution TEM (HRTEM) image of (a). (d) HRTEM of a higher magnification for the area indicated by a square in (c) and the simulation of the HRTEM image illustrated by a rectangle inset with white profile. The lattice-spacings belong to  $\{10\bar{1}\bar{1}\}$  (d-spacing 0.42 nm) and  $\{1\bar{1}02\}$  (d-spacing 0.37 nm)

more impact on the texture structure arrangement.

The high resolution TEM (HRTEM) image indicates that  $\alpha - Fe_2O_3$  possesses a well-defined crystal structure (Figure 4.5c). This suggests that crystalline  $\alpha - Fe_2O_3$  has already formed before 500°C. Heating at 500°C for 2 hr gives  $\alpha - Fe_2O_3$  enough energy and time to grow into a complete structure. Because dislocation is an important reason for the formation of texture structure, the rare existence of dislocation in the TEM observation for  $\alpha - Fe_2O_3$  treated at 500°C indicates that a well-defined crystal structure does form. As shown in Figure 4.5d, the simulated HRTEM image is overlapped with the experimental one. It is seen that they match very well. This is, from an alternative way, to confirm the formation of 500°C phase.

Hematite nanocrystals ( $\alpha - Fe_2O_3$ ) were synthesized previously using oleic acid as precursor solution or surfactant.[190]. The development of crystalline phase of  $\alpha - Fe_2O_3$  for iron oxide material was largely synthesized by using various conditions such as time-dependent (1-72 hr), different temperature ranges and change in precursors.[163, 191] Here, we coined a simple, straight and facile approach to develop  $\alpha - Fe_2O_3$  phase via solvent approach without using any post surfactant and precursor solution modification.

### 4.3.3 Formation of porous nanocaps from binary surface nanodroplets

The morphology and structure of the nanocaps can be modulated by doping nonreactive liquid in nanodroplets. As shown in Figure 4.6a and b, when the droplets consist of a mixture of oleic acid and octanol, the produced nanocaps exhibit many crevices on the surface. In contrast, the surface of the nanocaps synthesized from pure oleic acid shows a rough but uncracked surface, as shown in Figure 4.6d. Those crevices on the nanocaps are around 40 nm in width. When the droplets are a mixture of oleic acid and decane, the structure that is synthesized from binary droplets of oleic

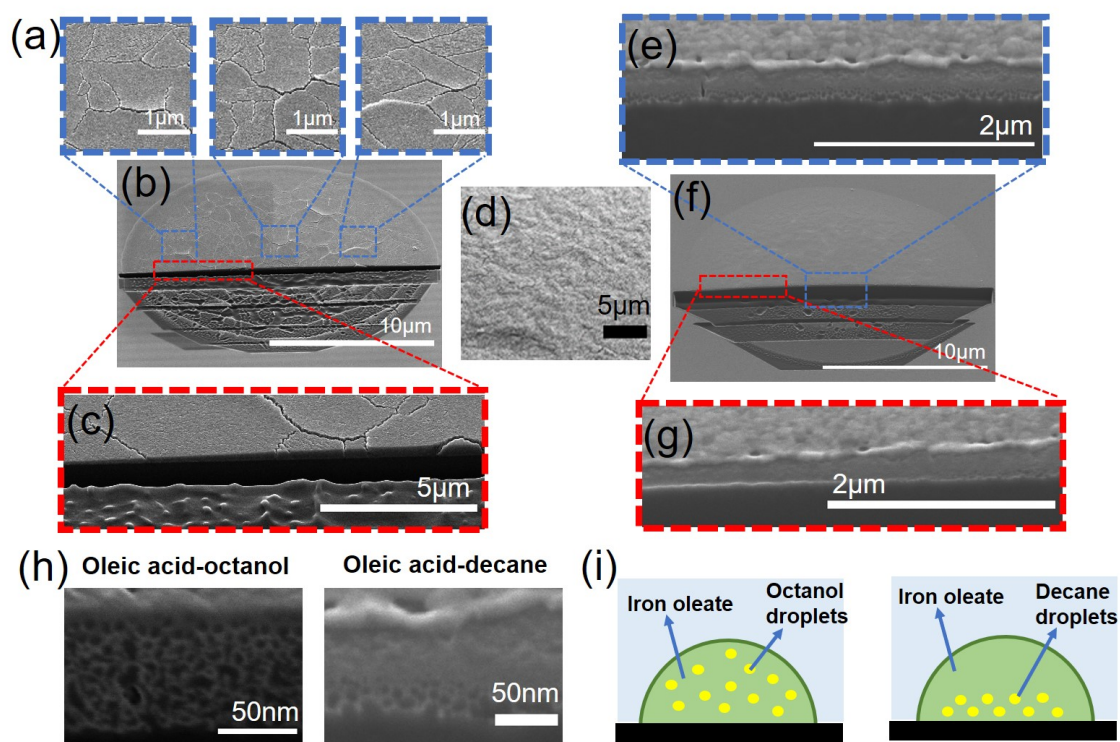


Figure 4.6: Surface and inner structures of iron oxide nanocaps fabricated from binary surface nanodroplets. (a) shows the creviced surface of the nanocap from oleic acid-octanol binary surface droplets. (b) The FIB-milled nanocap was fabricated from oleic acid-octanol binary surface droplets. (c) shows the inner structure of (b), indicating that the height of the nanocap increases toward to the center. (d) The rough but uncracked surface of the nanocap from pure oleic acid droplets. (e) and (g) show the inner structure of the nanocap synthesized from oleic acid-decane binary surface droplets (f), similar to the shape of (c). (h) High resolution images of the porous structure of the nanocaps synthesized from oleic acid-octanol binary surface droplets and oleic acid-decane binary surface droplets, respectively. (i) The sketch of the reaction process of binary surface nanodroplets with iron precursor.

acid-decane also have the shape of a thin and solidified spherical cap with a similar aspect ratio as the nanocaps from a single droplet, as shown in Figure 4.6(e-g).

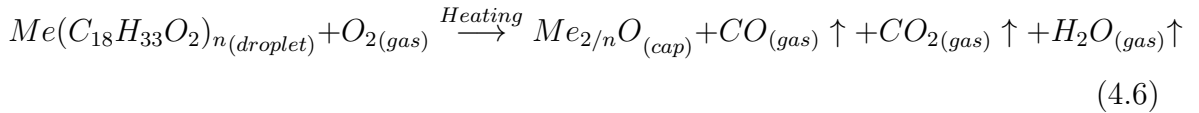
A distinct feature of the nanocaps formed from binary droplets of oleic acid and octanol is the highly porous inner structure, as shown in Figure 4.6h. In contrast, the nanocaps synthesized from the binary droplets of oleic acid and decane are more porous in the segment near the supporting substrate (Figure 4.6h).

It is interesting why the porous inner structure of nanocaps is formed from binary droplets. Based on the ratio of oleic acid and the solubility diagram in Figure 4.1c and d, the binary droplets mainly consist of oleic acid.[74] The appearance of the porous inner structure of nanocaps is most likely caused by the formation of the daughter droplets from the nonreactive liquid (1-octanol and decane) inside the droplets as well as the produced liquid from the reaction of oleic acid and iron precursor. The secondary oil small droplets may template the porous inner structure of the final nanocaps.

There is a difference in the surface activity of octanol and decane. Octanol is amphiphilic similar to oleic acid, while the later molecules are non-polar. Thus, during the reaction with the iron precursor, decane may reside inside the droplets. As oleic acid is converted to oleate, decane is pushed away from the droplet surface. As decane is oversaturated, forming daughter droplets located near the substrate base, as sketched in Figure 4.6i. In contrast, octanol uniformly distributes in the droplet due to its amphiphilic property. During heating, octanol or decane droplets evaporates, leading to permanent pores inside of the nanocaps. Same as the nanocaps prepared from pure acid droplets, the nanocaps fabricated from binary droplets (both acid-octanol and acid-decane) exhibit the crystalline structure of  $\alpha Fe_3O_3$ , as shown in Figure 4.15 and Figure 4.16.

### 4.3.4 Formation of other metal oxide nanocaps

The droplets of oleic acid are able to react with many metal precursors; hence the surface nanodroplets template method is effective for the synthesis of a wide range of metal oxide nanocaps. As a demonstration, we have expanded the approach for the synthesis of copper oxide, yttrium oxide and zinc oxide nanocaps on the substrate, as shown in Figure 4.7. The reaction for the formation of metal oleates and the subsequent thermal decomposition process is shown below.



Here,  $Me$  represents metal elements. The mass loss in the production of CuO,  $Y_2O_3$  and ZnO from the thermal decomposition is estimated to be 87.3%, 87.6% and 87.0%, respectively, leading to a significant reduction in surface coverage compared to that of initial droplets. Optical microscope images show that yttrium oxide nanocaps are yellow in the center and blue around the rim, while zinc oxide nanocaps show a light blue color all over the caps, as shown in Figure 4.7b and c. As for copper oxide, the optical image shows a dark and imperfectly spherical cap shape, as shown in Figure 4.7a. The color difference in nanocaps of copper oxide, yttrium oxide and zinc oxide and the iron oxide may be attributed to the refractive index of these two metal oxides. SEM images in Figure 4.7 show that the morphology of yttrium oxide is similar to iron oxide with a smooth surface. In contrast, copper oxide has a rough surface caused by the aggregation of the copper oxide nanoparticles. While zinc oxide shows a close texture of aggregation of non-spherical nanoparticles.

The successful synthesis of nanocaps of copper oxide, yttrium oxide and zinc oxide demonstrates that our method is general for forming diverse metal oxide nano/microstructures on a substrate. The universality of this method has the potential for developing surface-bound nanomaterials in many areas, including plasmonic effect,

photo-illumination enhancement, catalytic reaction and among others.

The as-produced nanocaps show strong adhesion to the substrate. The stability of

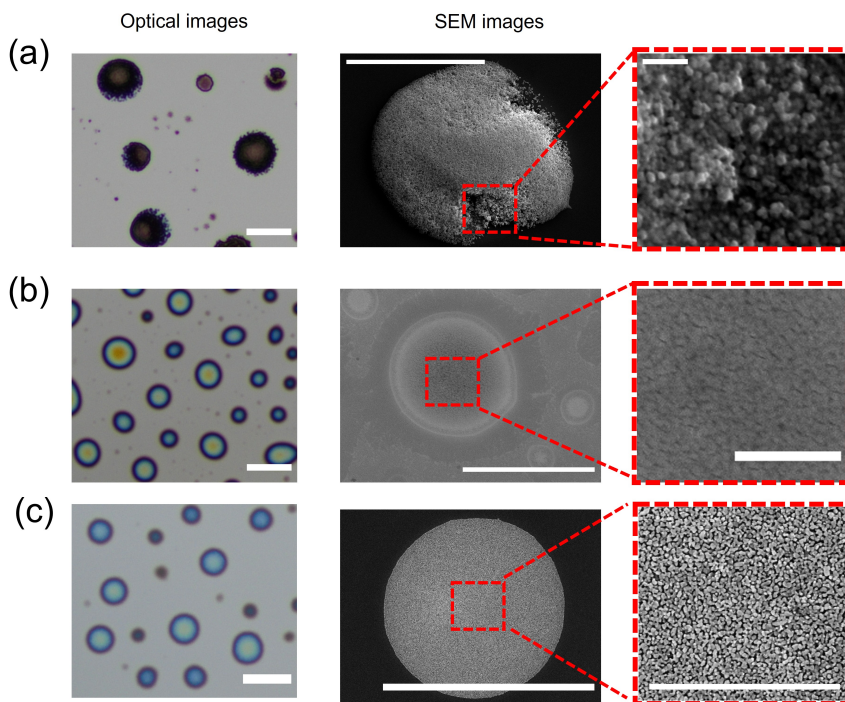


Figure 4.7: Optical (first column) and SEM images (second and third columns) of nanocaps of copper oxide (a), yttrium oxide (b) and Zinc oxide (c). Length of scale bare:  $25 \mu m$  (first column),  $15 \mu m$  (second column) and  $2 \mu m$  (third column).

the surface-bound nanocaps of iron oxide has been tested by sonication. After sonication for 60 minutes, the small nanocaps remained intact on the surface (SI-5a), while some of the large nanocaps were removed from the substrate. The surface coverage reduction by sonication treatment is more obvious for large nanocaps than for small nanocaps (Figure 4.13c).

We attribute the particularly strong adhesion between the caps and the substrate to the intimate contact between the iron oxide and the supporting substrate formed during the in-situ fabrication process and their strong van der Waal's interaction.[192]. Small nanocaps are even more resilient to sonication due to less probability of collid-

ing the cavitation bubbles.

### 4.3.5 Porous nanocaps for photodegradation

Nanocaps prepared in this work have the direct application potential for photocatalytic reactions in a flow-in chamber, demonstrated by photodegradation of methyl orange (MO) in the flow. As a demonstration, the iron oxide nanocaps of three different porosities were fabricated on a hydrophobized glass substrate and then was heated at 500 °C in air for 2 hours. The products have been proven to be  $\alpha - Fe_2O_3$  from the characterization in Figure 4.4. Nanocap (1) was prepared from pure oleic acid droplets. Nanocap (2) was from oleic acid-decane binary droplets and Nanocap (3) was from oleic acid-octanol binary droplets. As shown in Figure 4.8b and c, the surface coverage of those three nanocaps are 25%, 22% and 10%, respectively. The relative low photodegradation efficiency from the low surface coverage allowed us to identify the enhancement from porous structures.

The photo-catalytical reaction was performed in a micro-fluid chamber under visible light. The model compound was a dye (MO). As shown in Figure 4.8a, the nanocaps of iron oxide on the top glass plate headed down to the inner chamber as the dye solution flow through before being collected into a vial from the outlet.

The spectra of the UV-vis of the dye solution show a peak of absorbance around 464 nm. The efficiency of the degradation was evaluated by the intensity of the peak, as shown in Figure 4.14. The existence of the iron oxide nanocap can improve the efficiency at least more than 7 times of the bare glass slide. The improvement in degradation efficiency is attributed to the catalytic activity of iron oxide nanocaps. As shown in Figure 4.2c, 4.4b and 4.8a, the as-prepared nanocaps are ultra-thin and semitransparent. The light can pass the nanocaps into the solution phase. Herein, they are suitable for photocatalytic reactions.

The nanocaps with porous structures have obviously higher degradation efficiency. In Figure 4.8, the degradation efficiencies from three porosities are normalized by the surface coverage of the nanocaps. The normal efficiency for the most porous Nanocaps (No. 3) is more than twice of the efficiency for smooth nanocaps (No. 1). Nanocaps (1) without pores are the least effective for photodegradation. Clearly, the porous structure enhances the photodegradation due to the more surface area available for catalysis. The degradation efficiency may be further improved by optimizing the exposure time and, more effectively, by increasing the surface coverage of iron oxide nanocaps.

## 4.4 Conclusions

In conclusion, we firstly demonstrate an approach based on reactive surface nanodroplets for in-situ fabrication of metal oxide nanocaps with the controlled spatial arrangement and surface coverage on a solid surface. Compared to the published work on fabrication of the surface-bound materials or iron oxide nano materials,[153, 154, 156, 186, 193] our method shows a low chemical consuming, fast process in reaction, highly tunable on the morphology and inner structures. The crystalline structure of nanocaps can be conveniently varied in the post-synthesis process of the droplet reaction via thermal treatment. Notably, nanocaps with nanoporous structures can be produced by doping nonreactive liquid in reactive surface droplets. As applied to catalyze photodegradation of organic compounds in water, the porous nanocaps exhibit better performance as compared to smooth nanocaps. Reactive surface nanodroplets may open the window to the in-situ synthesis of a range of surface-bound nanomaterials. We expect that, in future work, the formation condition of nanocaps maybe further improved for optimal efficiency. The approach of surface nanodroplets reaction may be extended to other materials catalytic reaction, optical focusing and solar energy conversion.

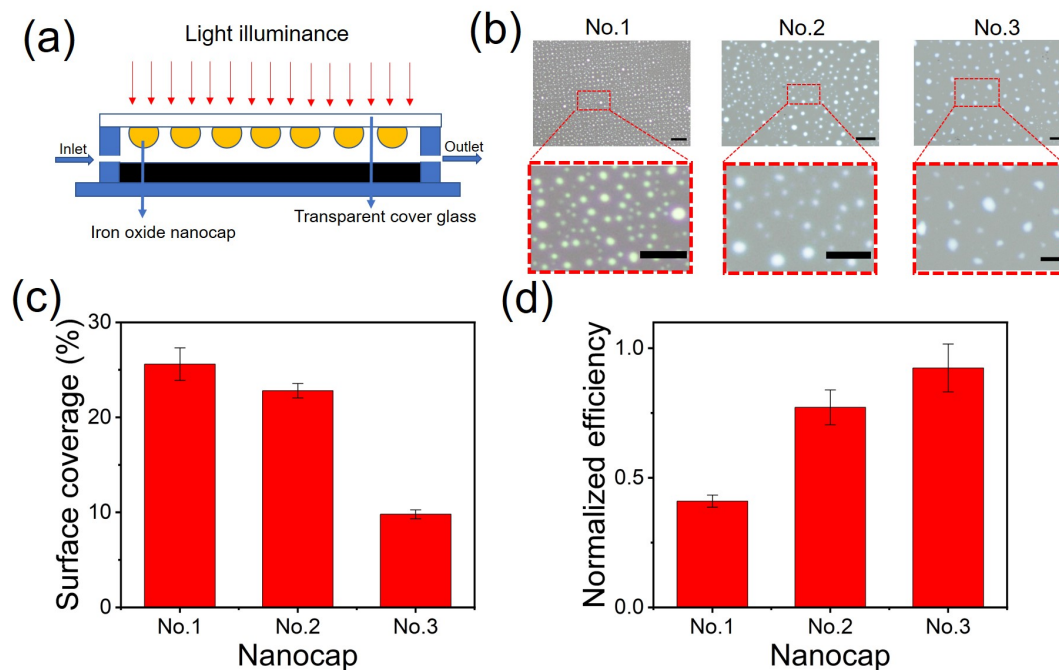


Figure 4.8: (a) Sketch of the fluid chamber for photo-degradation test. (b) Optical images of non-porous nanocaps (No.1), moderately porous nanocaps (No.2) and highly porous nanocaps (No.3) on the glass slide. (c) The surface coverage of the nanocaps corresponding to (b). (d) Normalized efficiency of photodegradation by nanocaps. The efficiencies are normalized by dividing the net efficiency of  $(E_{cap} - E_{glass})$  by surface coverage (S). Length of scale bar in (b):  $25 \mu m$  (top row) and  $15 \mu m$  (bottom row). Error bars in (c) and (d) were obtained from 3 repeats of the experiment.

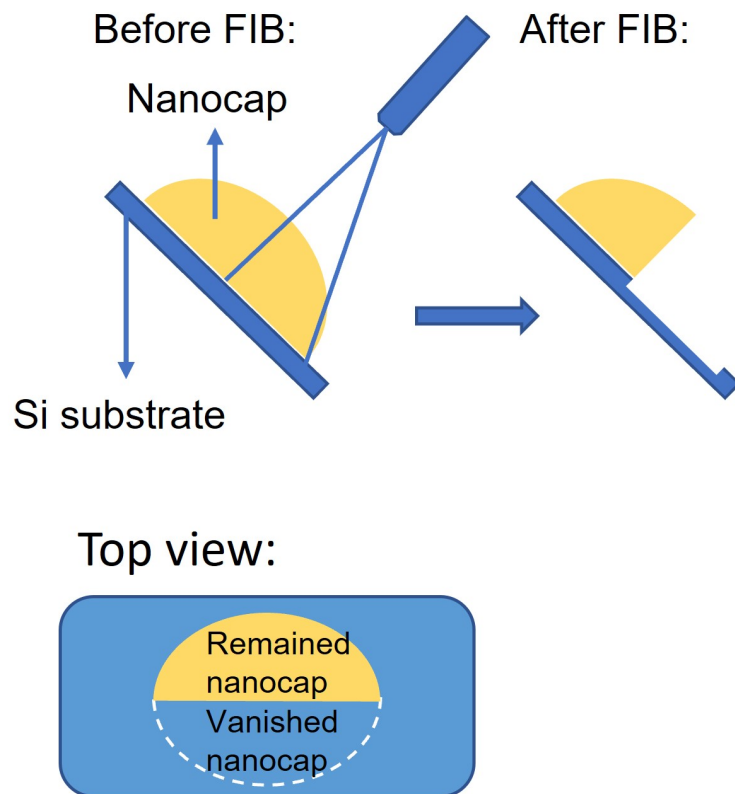


Figure 4.9: Sketch of the milling process by FIB..

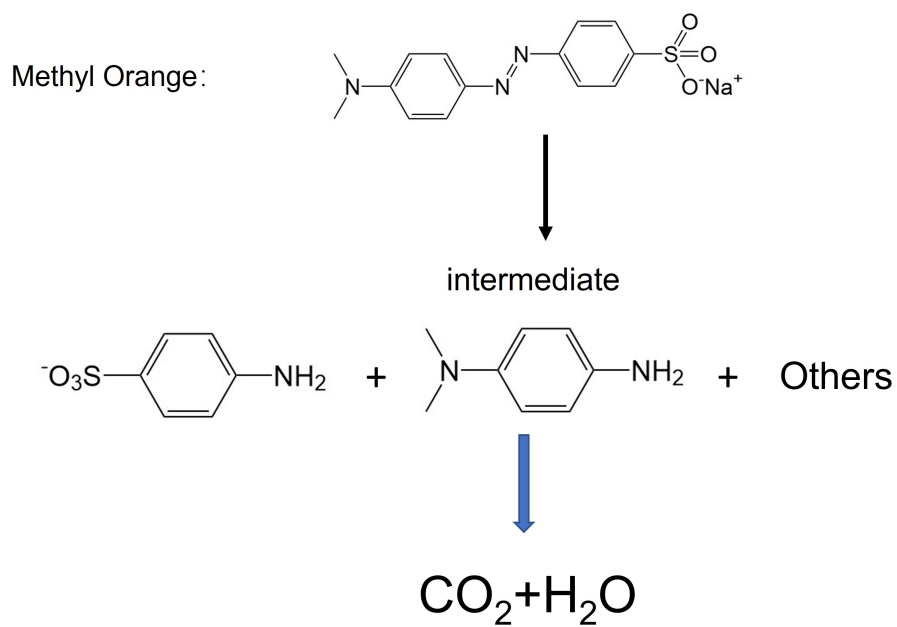


Figure 4.10: The chemical structure of the methyl orange and the degradation path.

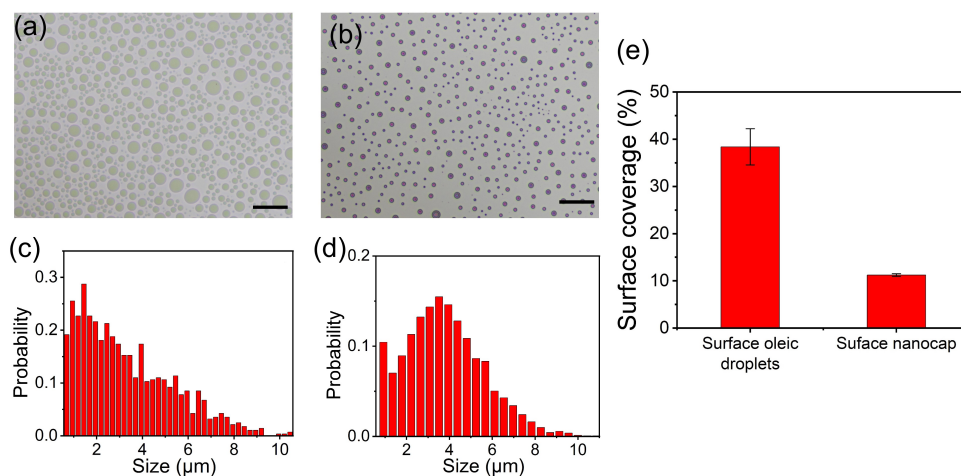


Figure 4.11: Optical images of surface oleic acid nanodroplets(a) and the iron oxide nanocaps after heating at 500°C (b). Probability density function (PDF) of the surface droplets (c) and nanocaps (d), corresponding to (a) and (b), respectively. (e) The surface coverage decreases after formation of nanocaps, indicating the significant mass loss during this process. Scale bar: 50  $\mu m$ .

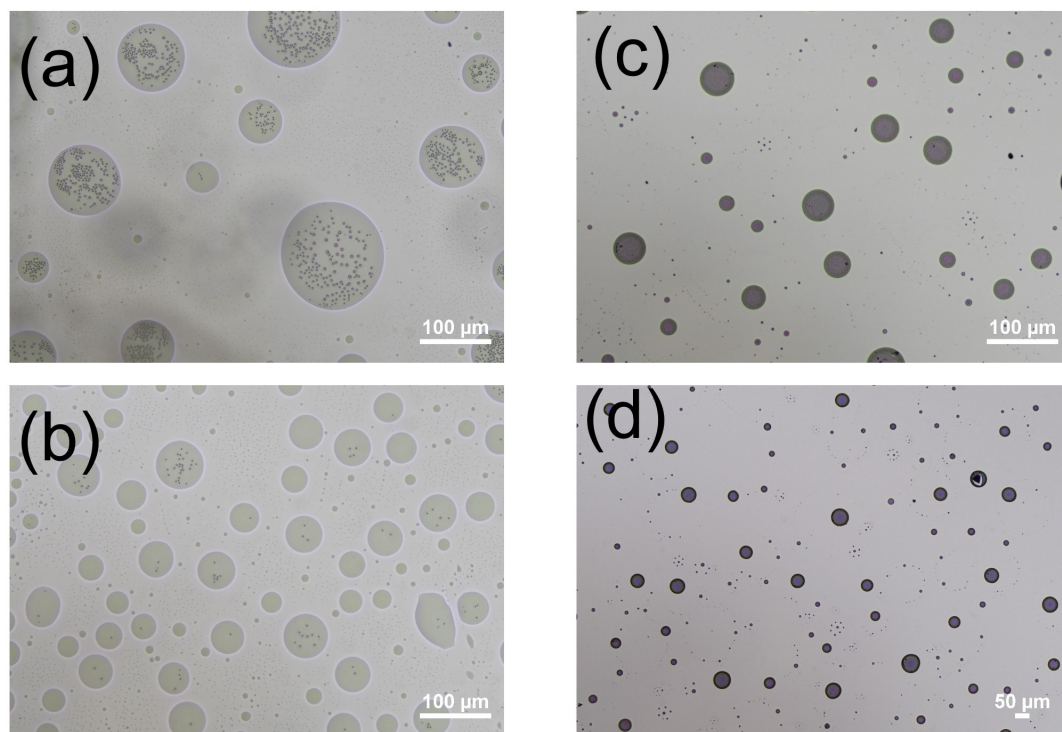


Figure 4.12: (a) and (b) are surface oleic acid droplets at larger size and intervals. (c) and (d) are the nanocaps after heating, corresponding to (a) and (b), respectively.

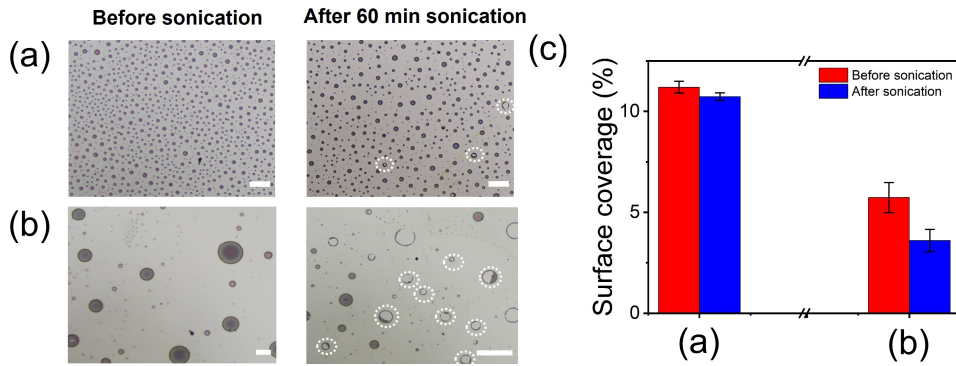


Figure 4.13: Optical Images of nanocaps at high surface coverage (a) and low surface coverage (b), before and after 60 min sonication and (b) at 25 ml/hr, before and after 60 min sonication. White circles represent the broken nanocap after sonication. (c) The surface coverage of the nanocaps on the surface before and after 60 minutes sonication. Scale bar: 100  $\mu m$ .

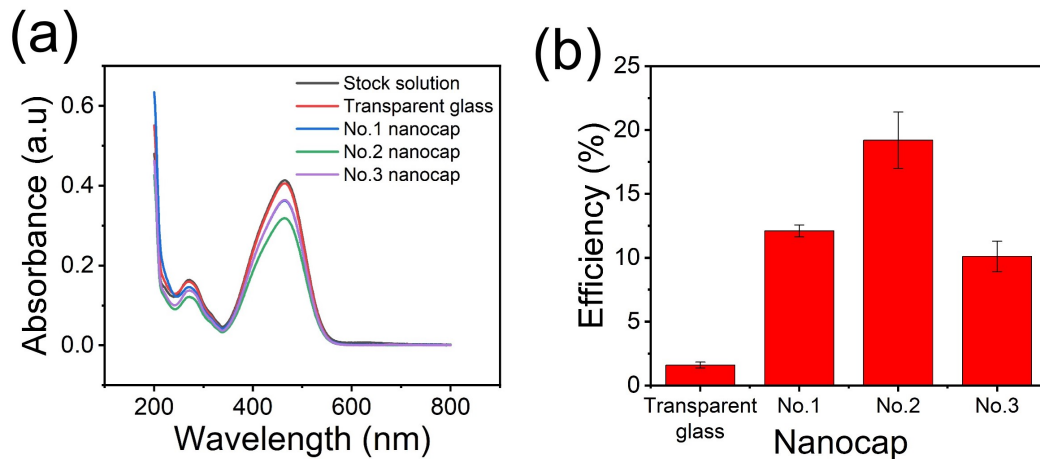


Figure 4.14: (a) The UV-vis spectra of the MO before and after degradation. The degradation efficiencies by using transparent cover glass and the cover glass with non-porous nanocap (No.1), moderately porous nanocap (No.2) and highly porous nanocap (No.3), respectively.

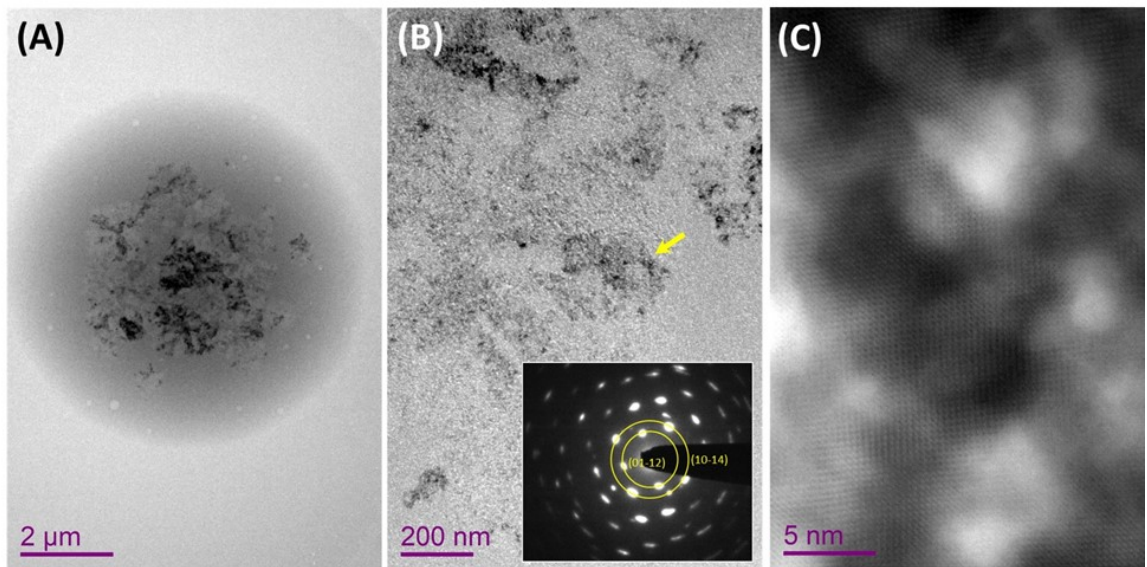


Figure 4.15: (A) Low magnification TEM images of the nanocaps from acid-octanol binary droplets. The SAED pattern shown as an inset is high magnification TEM images of the nanocaps (B). The marked rings assigned to (01-12) and (10-14) of  $\alpha - Fe_2O_3$ , respectively. (C) HRTEM image obtained from marked area in (B) displays a similar crystalline feature as the nanocaps from pure acid droplets.

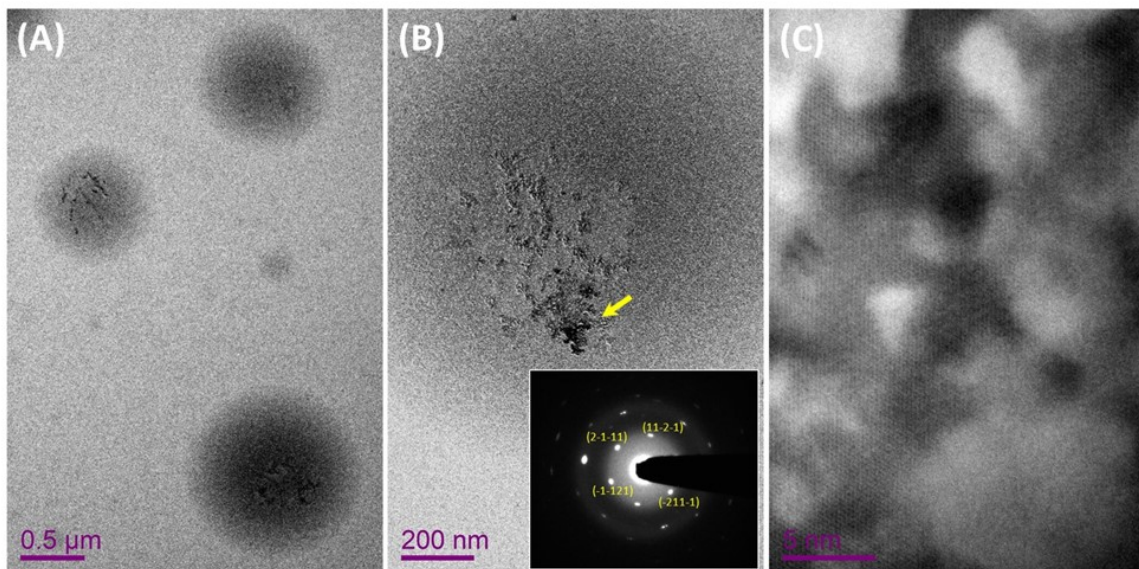


Figure 4.16: (A) Low magnification TEM images of the nanocaps from acid-decane binary droplets. The SAED pattern shown as an inset is high magnification TEM images of the nanocaps (B). The indexation on the SAED pattern suggests it be  $\alpha\text{-Fe}_2\text{O}_3$ . (C) The HRTEM image obtained from marked area in (B) displays a similar crystalline feature as the nanocaps from pure acid droplets.

## Chapter 5

# Nanorings of silver nanoparticles for surface enhancement Raman scattering (SERS)

### 5.1 Introduction

Surface enhancement Raman scattering (SERS) is a widely used strategy to enhance the Raman spectra signal by using metallic materials, especially metallic nanostructures[194]. When a laser irradiates to metallic nano-structure, the free electrons on the metallic nano-structure surface would oscillate, leading to an enhancement of the electric field on the surface. This electric field can enhance the intensity of the Raman signal, giving a lower detection limit. This enhancement of Raman signal by the surface electric field is known as SERS. The SERS is mostly used in ultra-sensitive chemical sensing field[195–198]. SERS is feasible to combine with some pre-concentrate method to increase the sensitivity, such as extraction[85], evapora-

tion[199] and among others. SERS can even reach the single-molecule level of detection[195, 199]. The principle of SERS is based on the electric field from the surface plasma resonance of the metallic nano-structures[197]. Such high sensitivity of SERS reduces the reproducibility of the chemical detection, which limits the practical application of SERS in chemical quantification[200–203].

The main reason for the low reproducibility of SERS is that the uncertain hotspots give unstable Raman signals during the measurement.[204, 205]. To overcome this uncertainty, highly ordered structures have been used to improve the reproducibility of SERS by fixing certain hotspots of each scan[206–212]. Some approaches, such as self-assembly[198, 213], template[214, 215] and electron beam lithography[216], have been applied to fabricate highly ordered structures, including film[217], nanorod[211], nanodot[209] and among others, to improve the SERS reproducibility. The current approach to fabricate SERS substrate with good performance needs to use a large amount of highly toxic chemicals. For example, Xu et al. fabricated an ordered SERS substrate that can achieve the detection of Rhodamine 6g (R6G) with LoD of  $10^{-11}M$  and a quantification range from  $10^{-8}M$  to  $10^{-11}M$ [218]. The LoD and the concentration correlation range of some reported work is summarized in Table 5.1. However, Fabrication of nanostructures with high precision dimensions require expensive equipment and dedicated clean room. Thus, simple, cost-effective, and solution-based methods on the fabrication of highly ordered substrates are valuable to widely spread applications of SERS.

Surface nanodroplets show the potential to micro-fabrication of highly ordered nano- or micro-structures bound on a substrate. Surface nanodroplets are the nano-scale (in height) droplets immobilized on a solid surface with an immiscible liquid surrounding[65]. Apart from advantages of bulk microdroplets in reaction and extraction enhancement[7, 18, 21, 27, 30, 31, 33]. surface nanodroplets are stable in an external flow. Recently, Li et al. combined the nanoextraction and surface enhancement Raman scattering (SERS) by using surface nanodroplets to achieve highly sensitive

chemical sensing with LoD of  $10^{-9}M$  and a quantitative range from  $10^{-6}M$  to  $10^{-9}M$  in the detection of R6G. Binary surface nanodroplets of VE and octanol were produced on a homogeneous substrate to achieve the extraction and detection of the chemicals by SERS.[85] This method enables a one-step of chemical extraction and sensing, which is much simplified compared to the traditional dispersive liquid-liquid microextraction (DLLME)[140]. However, the dispersed distribution of the droplets and the requirement for storing them in the liquid phase still limit the practical application.

In our previous work, surface-bound metal oxide with tunable size and porous fabricated from surface nanodroplets via biphasic reaction of droplet liquid and metal salts precursor solution[219]. This approach shows a simple, feasible and green method on fabrication surface nano- or micro-structures.

In addition, Bao et al. formed a highly ordered surface nanodroplets array by using chemically heterogeneous substrate[77]. Thus, we expected that the surface nanodroplets array would show excellent potential on the fabrication of highly ordered metallic micro-structures act as SERS substrate.

In this work, we formed the highly ordered silver micro-structures array from the biphasic reaction of the highly ordered surface nanodroplets array. The as-produced silver micro-structures show a ring structure corresponding to the surface nanodroplets. We explored the pH value and concentration of precursor solution effect on the fabrication of the silver micro-structures and found the optimized condition for detection of rhodamine 6G by SERS in a fluid chamber. This substrate shows a low LoD and broad d quantitative detection range. A further increase of SERS activity can be done by fabricating the highly ordered silver micro-structure on a transparent glass plate. Our approach shows a simple, cost-effective, and green method on the fabrication of SERS substrate.

Table 5.1: List of the reported LoD on highly ordered substrate for SERS.

| Work           | Materials               | Model compounds | LoD/M      | Quantitative range/M                       |
|----------------|-------------------------|-----------------|------------|--|
| Chu,2015[208]  | Ag nanocomplex          | 4-ATP           | $10^{-8}$  | NA   |
| Xu,2015[209]   | Ag nanodot              | R6G             | $10^{-11}$ | NA   |
| Chen,2015[211] | Au/Ag nanorod           | R6G             | $10^{-8}$  | NA   |
| Xu,2017[218]   | Ag nanoparticle         | R6G             | $10^{-11}$ | $10^{-8}$ to $10^{-11}$                    |
| Wang,2020[217] | Au film                 | R6G             | $10^{-13}$ | $10^{-9}$ to $10^{-5}$                     |
| Cai,2021[210]  | Ag array                | R6G             | $10^{-14}$ | $0.6 \times 10^{-8}$ to $1 \times 10^{-9}$ |
| Lu,2021[212]   | metallic glass nanotube | Crystal violet  | $10^{-11}$ | NA   |

## 5.2 Experimental section

### 5.2.1 Chemicals and materials

Ethanol (90%, Fisher Scientific) was used as a co-solvent to dissolve water and  $\alpha$ -tocopherol (Vitamin E, 97%, Alfa Aesar). Water was obtained from the Milli-Q water purification unit (Millipore Corporation, Boston, MA, USA). Silver nitrate solution (0.1 M, Fisher Scientific) was dissolved in water at concentration of 0.1 mM and 0.5 mM used as precursor solution. Sodium hydroxide (NaOH, 98%, Fisher Scientific) was used to adjust pH value. Rhodamine 6G (R6G, pure, Fisher Scientific) was used as the model analyst.

The silicon wafer (University wafer, USA) and borofloat glass (University wafer, USA) were hydrophobized and used as the substrate in this work. The substrate was firstly hydrophobized by coating of octadecyltrichlorosilane (OTS, 95%, Acros Organics) by following the same procedure as reported in previous work[64]. Then photolithography method was applied to remove some part of the OTS layer, exposing the hydrophilic background. Similar method of fabricating patterned substrate was reported in previous work[77]. Finally, hydrophobic domains created on the substrates were 5  $\mu m$  in the diameter with 2  $\mu m$  spacing among each other.

### 5.2.2 Formation of highly order array of surface nanodroplets array

Surface nanodroplets were formed in a fluid chamber via the solvent exchange process.[66] The sketch of the solvent exchange is shown in Figure 5.1a, where solution A is a ternary solution of water, ethanol and Vitamin E (VE) at volume ratio of 10:90:2.2 and solution B is pure water. Solution A was firstly filled in the fluid cham-

ber and then replaced by solution B at a constant flow rate of 5 ml/hr that was controlled by a syringe pump. After the solvent exchange, pure VE droplets were produced and formed on the hydrophobic microdomains of the substrate.

### 5.2.3 Fabrication of ring array of silver nanoparticles

The pH level of the silver nitrate solution was adjusted  $> 7$  using NaOH. After the array of surface nanodroplets was formed by solvent exchange, the precursor solution of basic silver nitrate was injected for 8 hours. The salt reacted with VE droplets in dark at a slow flow rate of 1.5 ml/hr. The product of the reaction between VE nanodroplets and silver ions were silver nanoparticles and  $\alpha$ -tocopherolquinone (VEq)[220], as shown in Figure 5.1b. VEq is liquid insoluble in water. Thus the droplet shape still remains on the surface after the reaction, while the produced silver nanoparticles stay at the surface of droplets, as shown in Figure 5.1b. The pH values and the precursor concentrations tested in this work are listed in Table.5.2. After the reaction of producing nanoparticles, ethanol is injected to dissolve and remove VEq from the substrate, as shown in Figure 5.1c. Finally, the substrate was ready for SERS detection.

### 5.2.4 Detection of model compounds by SERS

The SERS activity of the nanorings was evaluated by detection of R6G in an aqueous solution filled in the fluid chamber that could be same from the one for solvent exchange process above, as sketched in the Figure 5.1d. The aqueous solution of R6G was injected into the chamber. Confocal Raman microscope was used and focused at the ring pattern to obtain the Raman spectra.

When using the transparent glass substrate with silver ring, the side with silver rings

Table 5.2: The conditions (pH value and concentrations) of the precursor solution and the corresponding LoD and quantification range

| Substrate | Precursor solution |                  | LoD/M      |           | Quantificaiton Range/M |                       |
|-----------|--------------------|------------------|------------|-----------|------------------------|-----------------------|
|           | pH value           | Concentration/mM | 50X        | 5X        | 50X                    | 5X                    |
| Si        | 10                 | 0.1              | $10^{-7}$  |           |                        |                       |
|           | 10                 | 0.5              | $10^{-8}$  | $10^{-7}$ | $10^{-8}$ - $10^{-6}$  | $10^{-7}$ - $10^{-5}$ |
|           | 9                  | 0.5              | $>10^{-5}$ |           |                        |                       |
|           | 11                 | 0.5              | $10^{-7}$  |           |                        |                       |
| Glass     | 10                 | 0.5              | $10^{-9}$  | $10^{-8}$ | $10^{-8}$ - $10^{-5}$  | $10^{-8}$ - $10^{-5}$ |

faced into the flow of the analyte solution. The light in the Raman measurements transmitted through the glass and focused on the silver ring pattern.

### 5.2.5 Characterization

Optical images were obtained from Nikon eclipse optical microscope coupled with 10X lens. Field emission scanning electro microscope (FESEM, Zeiss Sigman) coupled with Energy Dispersive X-Ray Analysis (EDX, Oxford) was used to get the high resolution of the silver nanoparticles and confirm the product of the silver. The Raman spectra was obtained from confocal Raman microscope (Renishaw) coupled with 633 nm laser

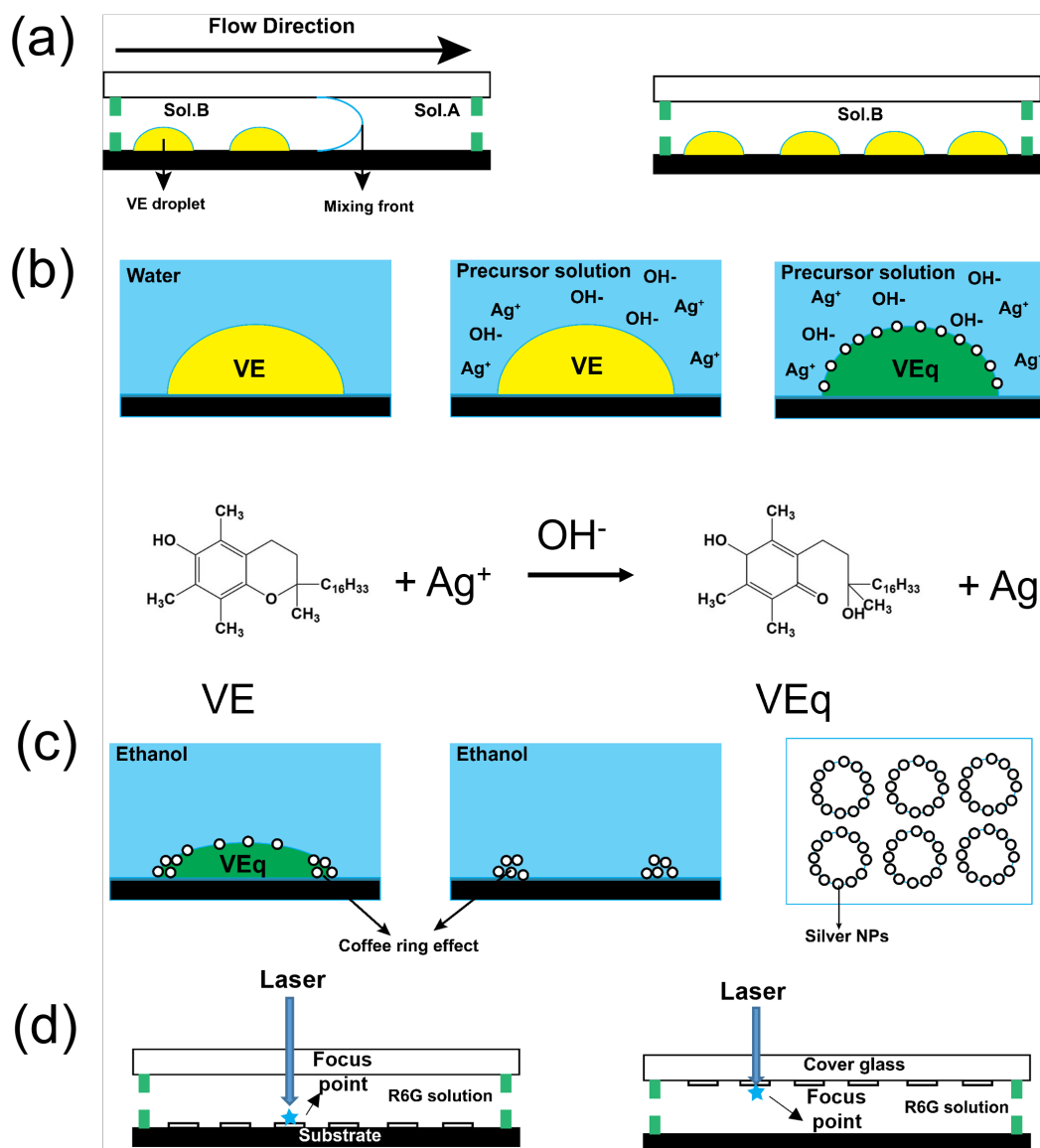


Figure 5.1: Sketch of the solvent exchange process for formation of surface nanodroplets (a), formation of the silver nanoparticles around the surface droplet interface (b), and fabrication of the ordered silver nanoparticles ring (c). Sol.A: ternary solution of water, ethanol and VE. Sol.B: pure water. Sol.C (precursor solution): base solution of silver nitrate solution. (d) Sketch of SERS detection of R6G solution in a chamber by using ordered silver nanorings as substrate (left) or cover glass (right).

at a power of 0.5 W. The magnification of the lens were 50x lens and 5x. Here, the 50x lens could focus on one entire domain of one silver nano-particle ring, while 5x lens can focus on many domains. Each Raman spectrum was collected from 5 seconds of acquisition time and 5 times accumulation to minimize the noise. The peaks and the corresponding vibration modes specific to R6G are listed in Table 5.3.

Table 5.3: Assignment for the peaks in Raman spectra of R6G molecule[221]

|                        |                               |                       |                   |                   |                     |
|------------------------|-------------------------------|-----------------------|-------------------|-------------------|---------------------|
| Raman shift/ $cm^{-1}$ | 610                           | 770                   | 1180              | 1310              | 1360, 1510 and 1650 |
| Vibration mode         | C-C-C ring in-plane vibration | C-H out-of-plane bend | C-H in-plane bend | N-H in-plane bend | C-C stretching      |

## 5.3 Results and discussion

### 5.3.1 Fabrication of array of nanorings

Pure VE surface nanodroplets were formed on pre-patterned substrate (chemically heterogeneous) from the solvent exchange. As shown in Figure 5.2a, the as-formed VE droplet array followed the pattern of the hydrophobic domains on the substrate. The diameter of  $5 \mu m$  and the spacing of  $2 \mu m$  were predetermined by the hydrophobic domain.

The silver micro-structures of different conditions are shown in Figure 5.2b. Rings of the nanoparticles formed around the rim of the domain (Figure 5.2b). More dense structure around the rim at a higher precursor concentration of 0.5 mM. For the same concentration of 0.5 mM, much less silver nanoparticles were found at lower pH value of 9.

The silver nanoparticles at above conditions were analyzed and shown in Figure 5.2c. The largest silver nanoparticles were obtained from 0.5 mM precursor solution with pH of 9. The clusters were in the center of the domain. Other conditions show a similar size of the silver nanoparticles ranging from 20 nm to 40 nm in radius. The element analysis was done by EDX in Figure 5.2d, indicating the formation of the silver. Absence of oxygen spectrum suggests that nanoparticles were silver instead of silver oxide.

We attributed the ring structure of the formation to the coffee ring effect during the dissolving of the VEq droplet[222]. The biphasic reaction between VE droplet and precursor solution happened at the interface of the droplet, leading to a formation of silver nanoparticles at the interface. With the consumption by the reaction, the final product of the droplet liquid is VEq armored with silver nanoparticles at the interface. The following process is the injecting of ethanol. During this process, the VEq droplet dissolved continuously. Since the edge of the droplet has a faster dissolving flux, the internal Marangoni flow happened due to the concentration difference. The silver nanodroplets thus accumulated at the edge and formed a ring structure[222]. When the pH was low, the  $OH^-$  limited the reaction rate in producing silver nanoparticles. Thus, one site of an already formed silver nanoparticle can act as a trigger to further growth and create a cluster. A dense cluster could submergence merge into the droplet and then settle down to the substrate, leading to a formation as shown in Figure 5.2b-3. At a high pH value of 11, since the silver nitrate can react with  $OH^-$  to form  $Ag_2O$ , the large amount of  $Ag_2O$  nanoparticles suspended in bulk and then precipitate on the substrate during the reaction process, leading to an unordered

substrate, as shown in Figure 5.2b-4.

### 5.3.2 SERS detection by using nanorings of silver nanoparticles

R6G was used as the model analyte. The limit of detection (LoD) by using the silver nanoring substrate fabricated by different conditions are listed in Table.5.2. The results show that sample 1 and 4 have the same LoD at  $10^{-7}M$ , while sample 3 has one magnitude lower LoD, possibly due to the further enhanced Raman signal by the dense silver sheet. However, no enhancement of the detection was found by the substrate fabricated by sample 3, possibly due to the small quantity of silver nanoparticles formed and their non-uniform distribution.

The Raman spectra of the R6G enhanced by the sample 1, 2 and 4 at their LoD were collected, as shown in Figure 5.3. The intensity of sample 2 is a little lower than sample 1 and 4, due to the lower LoD of sample 2. Compared to the control experiment, all of sample 1, 2 and 4 show specific peaks for R6G, as listed in Table.5.3, consistent with the reported work[85].

The above results suggest that the silver nanoparticle ring fabricated from condition of pH=9 and  $C_{sn}=0.5$  mM is the optimized one for SERS detection. To data, some researchers can fabricate the SERS substrate with the LoD of  $10^{-13}M$ [217, 223], which is much lower than our substrate. However, the main purpose of the highly ordered structure as SERS substrate is to improve the reproducibility and thus used to quantitatively determine the chemicals.

Quantification is one of the most critical parameters in chemical analysis to determine the concentration of the analyte. When we used a 50x objective lens to focus one domain of the silver nanoparticles, the LoD of the R6G detection is  $10^{-8}M$ , as listed in Table.5.2. As shown in Figure 5.4b, the spectra of three repeats experi-

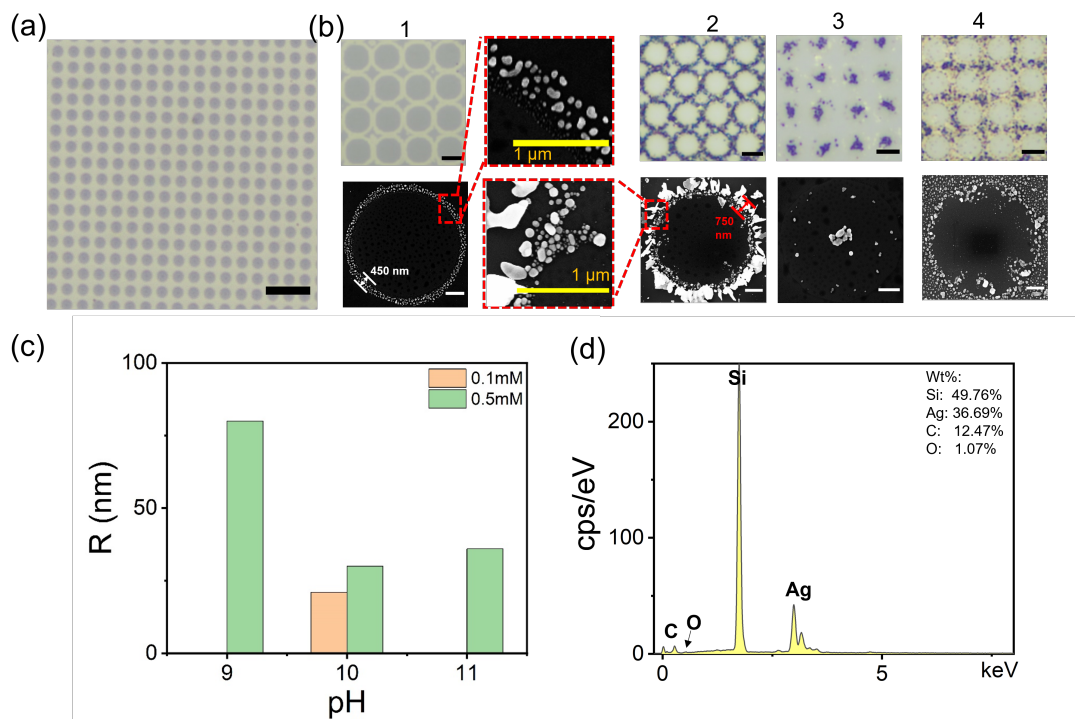


Figure 5.2: (a) Optical images of surface VE nanodroplets in an array on a pre-patterned substrate. (b) Optical images (top row) and SEM images (bottom row) of the ordered ring of silver nanoparticles fabricated from surface nanodroplets. At 1) pH=10, silver nitrate concentration ( $C_{sn}$ )=0.1 mM, 2) pH=10, silver nitrate concentration ( $C_{sn}$ )=0.5 mM, 3) pH=9, silver nitrate concentration ( $C_{sn}$ )=0.5 mM and 4) pH=11, silver nitrate concentration ( $C_{sn}$ )=0.5 mM. (c) Average size of the silver nanoparticles at reaction conditions corresponding to b. (d) EDX result indicated the formation of silver. The scale bar is  $50 \mu m$  for (a),  $5 \mu m$  for top row of (b) and  $1 \mu m$  for bottom row of (b).

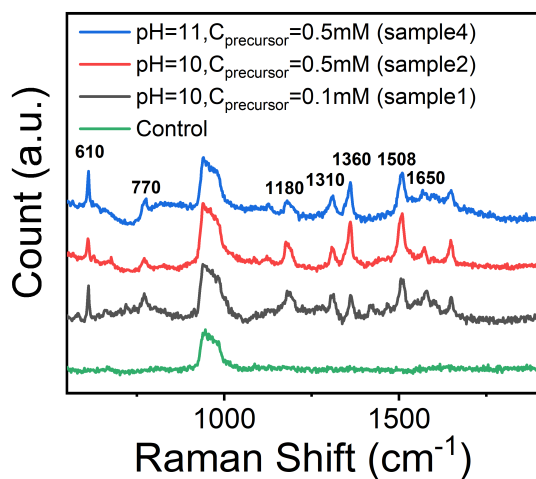


Figure 5.3: Raman spectra of R6G at the LoD of different substrates ( $10^{-7}M$  for sample 1 and 3,  $10^{-8}M$  for sample 2).

ment on detection of R6G at  $10^{-8}M$  prove the high reproducibility of this substrate. Two higher concentrations ( $10^{-7}M$  and  $10^{-6}M$ ) also have been tested and the Raman spectra were collected as shown in Figure 5.4a. When the R6G concentration is above  $10^{-6}M$ , at the default laser power, the signal is over the measuring range of the instrument due to the highly focused beam by 50x lens. Thus, to keep the result constant, we only collect the concentration from  $10^{-6}M$  to  $10^{-8}M$ .

Then, we used the peak at  $1508\text{ cm}^{-1}$  to quantitatively analysis the correlation between intensity and R6G concentration. In the lg-lg plot, the concentration of the R6G shows an excellent linear relationship ( $R^2 = 0.99$ ) to the Raman intensity from  $10^{-6}M$  to  $10^{-8}M$ , as shown in Figure 5.4b. This good linear relationship can be used to determine the analyte concentration in this range quantitatively.

A lower objective lens of 5x also has been tested at the same condition as the 50x lens to demonstrate that our substrate can also work well in a low objective lens. Compared to the high objective lens, the 5x lens can focus on a large area of the substrate instead of the single domain. The result shows that by using a 5x lens, the LoD of

R6G detection is  $10^{-7}M$ , which is one magnitude lower than by 50x lens. However, 5x lens shows a detection range from  $10^{-4}M$  to  $10^{-7}M$ , which is same broad but one magnitude lower than 50x lens, possible due to the lower focusing of 5x lens and thus lower intensity of the Raman signal. In addition, at low objective lens, the substrate also showed a high reproducibility, as shown in Figure 5.4e.

A good linear correlation ( $R^2 = 0.98$ ) by 5x lens was found from  $10^{-5}M$  to  $10^{-7}M$  in the lg-lg plot of the R6G concentration and peak intensity at  $1508\text{ cm}^{-1}$ , as shown in Figure 5.4d. The highly ordered silver structures show good stability of the Raman signal due to the same number of hotspots in a given area, providing the same response everywhere. By coupling with 50x lens and 5x lens, the quantification range of our substrate is  $10^{-5}M$  to  $10^{-8}M$ . Li et al. used the coupled nanoextraction and SERS detection by using surface nanodroplets can achieve the quantification range from  $10^{-6}M$  to  $10^{-9}M$ . [85] A more recent work done by Wang et al. shows that by using Au film, the quantification SERS detection of R6G can range from  $10^{-5}M$  to  $10^{-9}M$ . [217] Compared to the above works, our substrate show a competitive quantification range. In addition, Our substrate shows a good LoD of R6G detection in an aqueous solution without any extraction or pre-treatment procedures, which is significantly simplifies the detection process.

### 5.3.3 Enhanced detection by SERS substrate

We used the same procedure but changed the Si substrate to borofloat glass to fabricate the ordered silver nanoparticles ring pattern and apply this to R6G detection. The borofloat glass with silver nanoparticles ring pattern replaced the cover-glass in the fluid chamber and the face with silver nanoparticles towards the liquid, as sketched in Figure 5.1d. At this set-up, the laser will not penetrate the liquid phase and will just focus on the top plate. We found that by using a 50x lens, the LoD of

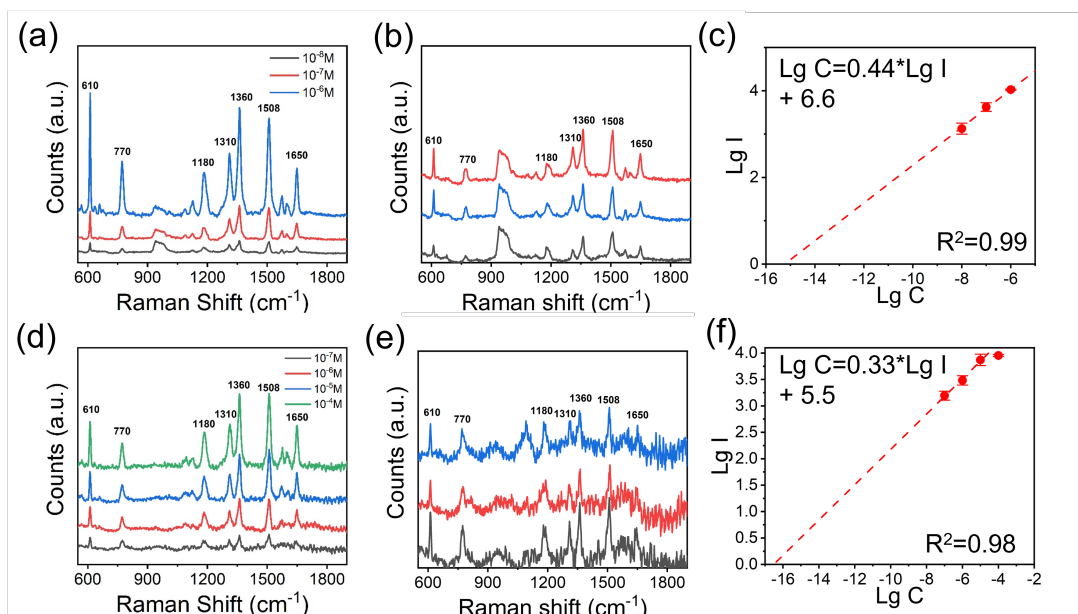


Figure 5.4: Surface enhancement Raman spectra of R6G at different concentrations by using 50x lens (a) and 5x lens (d). Three repeats in the experiments at the LoD by using 50x lens (b) and 5x lens (e) demonstrate high reproducibility. The correlation of R6G concentration and the peak intensity of  $1508\text{ cm}^{-1}$  in lg-lg plot show linear relation by using 50x lens (c) and 5x lens (f). Error bars are from 3 repeats of the experiment to ensure the reproducibility.

R6G detection is  $10^{-9}M$ , as listed in Table.5.2, which is one magnitude lower than using the substrate. The Raman spectra of R6G at different concentrations was shown in Figure 5.5a. Here, when the concentration is  $10^{-9}M$ , the Raman signal is very weak, as shown in Figure 5.5b. However still, there are some specific peaks that can be recognized. By using the cover-glass, the quantitative detection range was found from  $10^{-8}M$  to  $10^{-5}M$ , which is broader than using the substrate.

When we used the 5x lens, the LoD of R6G detection is  $10^{-8}M$ , which is also one magnitude lower than using the substrate. As shown in Figure 5.5e, the spectra of three repeats experiment on detection of R6G at  $10^{-8}M$  prove the high reproducibility of this substrate. The Raman spectra of R6G at different concentrations was shown in Figure 5.5d, showing an increase of the peak intensity with the concentration. By using the cover-glass, the quantitative detection range was found from  $10^{-5}M$  to  $10^{-8}M$  (Figure 5.5f), same as the 50x lens.

We attribute this better LoD and the quantitative detection range by using cover-glass to less interference from the liquid layer. When the substrate setup was used, the laser needed to penetrate the aqueous solution first and then reach the substrate of the surface as shown in Figure 5.1d. During this penetration, the power of the laser was consumed, leading to a less collection of the signal. While, when we used the cover-glass setup, the consumption of the laser by the aqueous solution can be eliminated, possibly leading to a stronger light intensity than on bottom Si substrate.

## 5.4 Conclusions

In summary, we reported an approach to fabricate the highly ordered silver microstructure based on the biphasic reaction of the surface nanodroplets array. The synthesis process parameter of pH value and precursor solution concentration have been tested to find the best condition for SERS application. The SERS property was

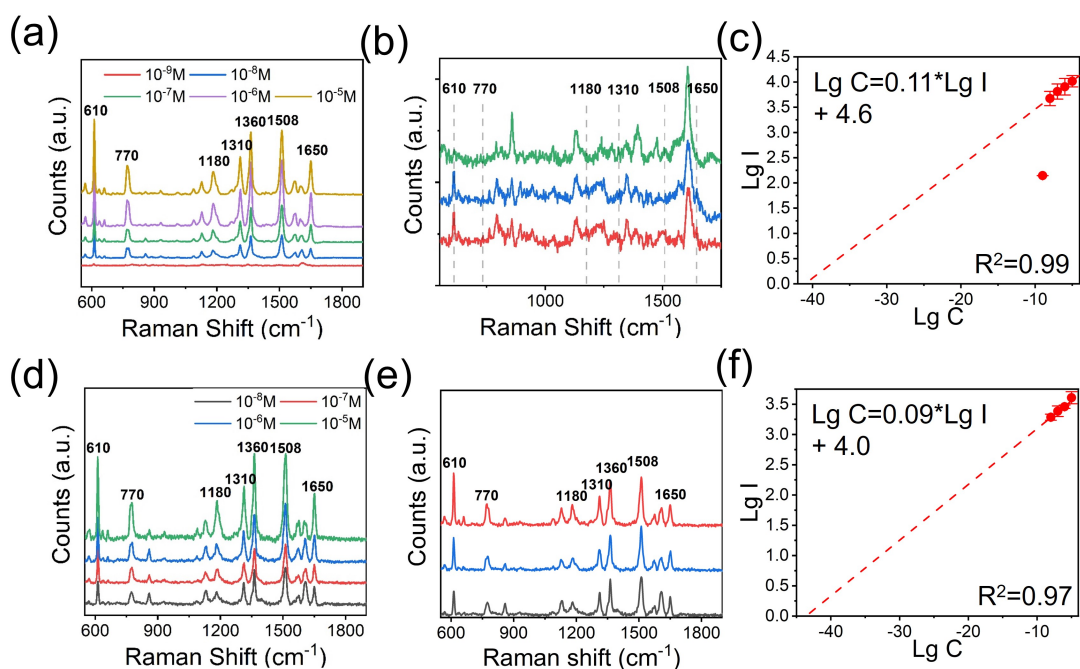


Figure 5.5: (a) and (d) are the surface enhancement Raman spectra of the R6G at different concentrations by using 50x lens and 5x lens, respectively. Three repeats in the experiments at the LoD by using 50x lens (b) and 5x lens (e) demonstrate a good reproducibility. (d) and (f) are the linear correlation of the concentration of R6G and the peak intensity at 1508  $cm^{-1}$  in lg-lg plot, respectively. Error bars are from 3 repeats of the experiment to ensure the reproducibility.

evaluated by the detection of R6G aqueous solution in a microfluid chamber. The fabricated SERS substrate by our method shows good LoD and good quantitative detection range. In addition, the SERS activity can be further improved by fabricating the silver micro-structure on a transparent glass plate. Our approach shows simple, cost-effective and green method on the fabrication of SERS substrate. The feasibility of the fabrication process may broaden our approach in a wide application situation.

# Chapter 6

## Conclusions and outlook

### 6.1 Conclusions

This thesis presents the formation and applications of functional surface nanodroplets in the identification of multicomponent acidic mixtures, understanding the partition and chemical reaction in micro-sized droplets, surface-bound materials synthesis and fabrication of SERS substrates. The as-produced surface nanodroplets show excellent properties for extraction and chemical reaction enhancement. Compared to bulk microdroplets, surface nanodroplets exhibit a long lifetime, high stability and controllable formation and thus have the potential for a wide range of practical applications. At first, we used the surface nanodroplets as a novel method to distinguish multicomponents mixtures in a one-step, in-situ and instrument-free manner. The colored surface nanodroplets containing pH indicator were formed by solvent exchange. By extracting organic acid from the external flow, the droplets show a color change due to the reduction of the pH value due to the colorimetric reaction of the extracted acid and pH indicator. The time scale of the droplet decoloration is specific to acid type, concentration and droplet size. Most importantly, the droplets change color at a characteristic time for the combination of the acid mixture with the same pH level.

We demonstrated the application of our method in anti-counterfeiting of famous Chinese spirits directly within a color change of the droplets could be simply observed by using the camera of a smartphone.

Furthermore, the decoloration time scale of surface nanodroplets works as a tool to understand the kinetics of the combinative effect of nanoextraction and colorimetric reaction in the micro-scale. Colorimetric reaction is reversible reaction, which is a kind of long-term reaction. Thus, the detail process is difficult to be measured by bulk microdroplets due to the short lifetime. Surface nanodroplets give enough lifetime and stable positions to analyze the long-term reaction. Thus, we experimentally and theoretically investigated the integrated extraction and reaction of analytes in surface nanodroplets by extracting seven different acids from the external liquid. We found a significant shift in the partition of the acids into the reacting droplets at a low concentration of acid in the external solution, leading to a more sensitive analysis compared to the bulk system. The effective partition can be 3-11 times higher than in bulk. This partition shift is attributed to the chemical reaction in the droplet and is proposed to be the rate-limiting step.

The functional surface nanodroplets provide templates and nucleation sites for fabrication materials, which can give a strong bond to the substrate and enhance the biphasic reaction. Thus, we applied the reactive surface droplet in the fabrication of surface-bound materials and highly ordered micro-structures via in-situ biphasic reaction on a solid substrate. The porous structures of the as-produced nanocap can be tunable by adding a non-reactive liquid to the droplet. The porous nanocaps show higher efficiency as a photo-catalyst in the degradation of dye solution than smooth nanocaps. In addition, this method shows excellent feasibility on fabrication of diverse materials. Thus, by forming a highly ordered surface nanodroplets array, we fabricated an ordered silver nanoparticles ring pattern. The highly ordered structure gives the certain hotspots of Raman signal, thus improving the reproducibility of the detection. Thus, a good quantification range of R6G detection from  $10^{-4}M$  to  $10^{-8}M$

has been found by using this substrate, which is competitive to the reported work. We further increase the sensitivity by fabricating the same structure on a transparent glass plate. Our method reduced the requirement of the fabrication compared to some SERS substrates with similar performance.

## 6.2 Outlook

Although great efforts have been made to apply functional surface nanodroplets in different applications, many areas still can benefit from the advantages of the surface nanodroplets in practical implements. The following works may be valuable for further research.

(1) Surface nanodroplets-based chemical extraction can be further enhanced by narrowing the channel height, leading to better mass transportation from bulk to the droplets. Besides, the nanoextraction process can also be coupled with other analytical instruments to achieve more precise analysis.

(2) Due to the color change of the pH indicator is not linear to the acid extraction, the above work for understanding the couple nanoextraction and reaction only considered the time scale of the total process. However, it is valuable to dynamically monitor the extracted analyte in the droplet with time. A fluorescence-based reaction may help to monitor the extraction and reaction process by the fluorescence intensity change during the process.

(3) At present, fabrication of the surface-bound materials is only on a lab scale. A scale-up is expected to apply this surface-bound material for higher efficiency in the photo-degradation and thus used in practical situations. Furthermore, the bi-metallic or tri-metallic surface-bound materials may also be formed to broaden the application to other areas, such as surface plasma resonance and solar harvest.

(4) The highly order micro-structures from surface nanodroplets can be further func-

tionalized by chemicals, which may help to improve the performance of the SERS activities.

# Bibliography

- [1] Z. Liu, J. Y. Lee, M. Han, W. Chen, and L. M. Gan, “Synthesis and characterization of PtRu/C catalysts from microemulsions and emulsions,” *Journal of Materials Chemistry*, vol. 12, no. 8, pp. 2453–2458, 2002.
- [2] L. Wang *et al.*, “Autonomic behaviors in lipase-active oil droplets,” *Angewandte Chemie International Edition*, vol. 131, no. 4, pp. 1079–1083, 2019.
- [3] L. Yan, H. Wang, L. Bai, Y. Fu, and Y. Cheng, “Suzuki-miyura cross-coupling reaction in droplet-based microreactor,” *Chemical Engineering Science*, vol. 207, pp. 352–357, 2019.
- [4] A. B. Theberge *et al.*, “Microdroplets in microfluidics: An evolving platform for discoveries in chemistry and biology,” *Angewandte Chemie International Edition*, vol. 49, no. 34, pp. 5846–5868, 2010.
- [5] C. Xu and T. Xie, “Review of microfluidic liquid–liquid extractors,” *Industrial & Engineering Chemistry Research*, vol. 56, no. 27, pp. 7593–7622, 2017.
- [6] J. Bednář, L. Svoboda, P. Mančík, and R. Dvorský, “Synthesis of zns nanoparticles of required size by precipitation in aerosol microdroplets,” *Materials Science and Technology*, vol. 35, no. 7, pp. 775–781, 2019.

- [7] J. Qian, G. F. Arends, and X. Zhang, "Surface nanodroplets: Formation, dissolution, and applications," *Langmuir*, vol. 35, no. 39, pp. 12 583–12 596, 2019.
- [8] M. Rezaee, Y. Assadi, M.-R. M. Hosseini, E. Aghaee, F. Ahmadi, and S. Berijani, "Determination of organic compounds in water using dispersive liquid–liquid microextraction," *Journal of Chromatography A*, vol. 1116, no. 1-2, pp. 1–9, 2006.
- [9] L. Wang, "Simultaneous determination of retinal, retinol and retinoic acid (all-trans and 13-cis) in cosmetics and pharmaceuticals at electrodeposited metal electrodes," *Analytica Chimica Acta*, vol. 415, no. 1-2, pp. 193–200, 2000.
- [10] M. Rueda, L. Sarabia, A. Herrero, and M. Ortiz, "Optimisation of a flow injection system with electrochemical detection using the desirability function: Application to the determination of hydroquinone in cosmetics," *Analytica Chimica Acta*, vol. 479, no. 2, pp. 173–184, 2003.
- [11] G. Holloway, R. Maheswaran, A. Leeks, S. Bradby, and S. Wahab, "Screening method for ethylene glycol and diethylene glycol in glycerin-containing products," *Journal of Pharmaceutical and Biomedical Analysis*, vol. 51, no. 3, pp. 507–511, 2010.
- [12] Y. S. Nam, I. K. Kwon, and K.-B. Lee, "Monitoring of clobetasol propionate and betamethasone dipropionate as undeclared steroids in cosmetic products manufactured in korea," *Forensic Science International*, vol. 210, no. 1-3, pp. 144–148, 2011.

- [13] X. Wang, L. Wei, G. Tao, and L. Dai, "Determination of hydrocortisone in cosmetics by CdSe/CdS quantum dots-based fluoroimmunoassay using magnetic  $Fe_3O_4/Au$  nanoparticles as solid carriers," *Chinese Journal of Chemistry*, vol. 29, no. 3, pp. 587–591, 2011.
- [14] Y. S. Nam, I. K. Kwon, Y. Lee, and K.-B. Lee, "Quantitative monitoring of corticosteroids in cosmetic products manufactured in korea using LC-MS/MS," *Forensic Science International*, vol. 220, no. 1-3, e23–e28, 2012.
- [15] N Cabaleiro, I De La Calle, C Bendicho, and I Lavilla, "Current trends in liquid–liquid and solid–liquid extraction for cosmetic analysis: A review," *Analytical Methods*, vol. 5, no. 2, pp. 323–340, 2013.
- [16] R. Zalieckaitė, E. Adomavičiūtė, and V. Vičkačkaitė, "Single-drop microextraction for the determination of phthalate esters.," *Chemija*, vol. 18, no. 3, 2007.
- [17] M. Saraji and S. Mirmahdieh, "Single-drop microextraction followed by in-syringe derivatization and GC-MS detection for the determination of parabens in water and cosmetic products," *Journal of Separation Science*, vol. 32, no. 7, pp. 988–995, 2009.
- [18] M Borremans, J Van Loco, P Roos, and L. Goeyens, "Validation of hplc analysis of 2-phenoxyethanol, 1-phenoxypropan-2-ol, methyl, ethyl, propyl, butyl and benzyl 4-hydroxybenzoate (parabens) in cosmetic products, with emphasis on decision limit and detection capability," *Chromatographia*, vol. 59, no. 1, pp. 47–53, 2004.

- [19] C. Feng and S. Jiang, "Micro-scale quantitation of ten phthalate esters in water samples and cosmetics using capillary liquid chromatography coupled to uv detection: Effective strategies to reduce the production of organic waste," *Microchimica Acta*, vol. 177, no. 1-2, pp. 167–175, 2012.
- [20] L. Guo, N. binte Nawi, and H. K. Lee, "Fully automated headspace bubble-in-drop microextraction," *Analytical Chemistry*, vol. 88, no. 17, pp. 8409–8414, 2016.
- [21] C Villa, R Gambaro, E Mariani, and S Dorato, "High-performance liquid chromatographic method for the simultaneous determination of 24 fragrance allergens to study scented products," *Journal of Pharmaceutical and Biomedical Analysis*, vol. 44, no. 3, pp. 755–762, 2007.
- [22] A. Zgoła-Grześkowiak and T. Grześkowiak, "Dispersive liquid-liquid microextraction," *TrAC Trends in Analytical Chemistry*, vol. 30, no. 9, pp. 1382–1399, 2011.
- [23] C. Almeida, J. Fernandes, and S. Cunha, "A novel dispersive liquid–liquid microextraction (DLLME) gas chromatography-mass spectrometry (GC-MS) method for the determination of eighteen biogenic amines in beer," *Food Control*, vol. 25, no. 1, pp. 380–388, 2012.
- [24] S. Khodadoust and M. Hadjmohammadi, "Determination of n-methylcarbamate insecticides in water samples using dispersive liquid–liquid microextraction and hplc with the aid of experimental design and desirability function," *Analytica Chimica Acta*, vol. 699, no. 1, pp. 113–119, 2011.

- [25] A. Gong and X. Zhu, “Miniaturized ionic liquid dispersive liquid–liquid microextraction in a coupled-syringe system combined with uv for extraction and determination of danazol in danazol capsule and mice serum,” *Spectrochimica Acta Part A: Molecular and Biomolecular Spectroscopy*, vol. 159, pp. 163–168, 2016.
- [26] S. A. Vitale and J. L. Katz, “Liquid droplet dispersions formed by homogeneous liquid- liquid nucleation: “the ouzo effect”,” *Langmuir*, vol. 19, no. 10, pp. 4105–4110, 2003.
- [27] P. Viñas, N. Campillo, I. López García, and M. Hernández Córdoba, “Dispersive liquid–liquid microextraction in food analysis. a critical review,” *Analytical and Bioanalytical Chemistry*, vol. 406, no. 8, pp. 2067–2099, 2014.
- [28] Y. Zhang, J. Duan, M. He, B. Chen, and B. Hu, “Dispersive liquid liquid microextraction combined with electrothermal vaporization inductively coupled plasma mass spectrometry for the speciation of inorganic selenium in environmental water samples,” *Talanta*, vol. 115, pp. 730–736, 2013.
- [29] Z. Wei, Y. Li, R. G. Cooks, and X. Yan, “Accelerated reaction kinetics in microdroplets: Overview and recent developments,” *Annual Review of Physical Chemistry*, vol. 71, pp. 31–51, 2020.
- [30] J. K. Lee, S. Banerjee, H. G. Nam, and R. N. Zare, “Acceleration of reaction in charged microdroplets,” *Quarterly Reviews of Biophysics*, vol. 48, no. 4, pp. 437–444, 2015.

- [31] J. K. Lee, S. Kim, H. G. Nam, and R. N. Zare, “Microdroplet fusion mass spectrometry for fast reaction kinetics,” *Proceedings of the National Academy of Sciences*, vol. 112, no. 13, pp. 3898–3903, 2015.
- [32] I. Nam, J. K. Lee, H. G. Nam, and R. N. Zare, “Abiotic production of sugar phosphates and uridine ribonucleoside in aqueous microdroplets,” *Proceedings of the National Academy of Sciences*, vol. 114, no. 47, pp. 12 396–12 400, 2017.
- [33] Y. Li *et al.*, “Accelerated forced degradation of pharmaceuticals in levitated microdroplet reactors,” *Chemistry—A European Journal*, vol. 24, no. 29, pp. 7349–7353, 2018.
- [34] Z. Wei, X. Zhang, J. Wang, S. Zhang, X. Zhang, and R. G. Cooks, “High yield accelerated reactions in nonvolatile microthin films: Chemical derivatization for analysis of single-cell intracellular fluid,” *Chemical Science*, vol. 9, no. 40, pp. 7779–7786, 2018.
- [35] R. M. Bain, C. J. Pulliam, F. They, and R. G. Cooks, “Accelerated chemical reactions and organic synthesis in leidenfrost droplets,” *Angewandte Chemie International Edition*, vol. 55, no. 35, pp. 10 478–10 482, 2016.
- [36] G. Caldwell, T. F. Magnera, and P. Kebarle, “ $SN_2$  reactions in the gas phase. temperature dependence of the rate constants and energies of the transition states. comparison with solution,” *Journal of the American Chemical Society*, vol. 106, no. 4, pp. 959–966, 1984.

- [37] B. Gologan, J. R. Green, J. Alvarez, J. Laskin, and R. G. Cooks, “Ion/surface reactions and ion soft-landing,” *Physical Chemistry Chemical Physics*, vol. 7, no. 7, pp. 1490–1500, 2005.
- [38] Z. Zhou, X. Yan, Y. Lai, and R. N. Zare, “Fluorescence polarization anisotropy in microdroplets,” *The Journal of Physical Chemistry Letters*, vol. 9, no. 11, pp. 2928–2932, 2018.
- [39] M. F. Toney *et al.*, “Voltage-dependent ordering of water molecules at an electrode–electrolyte interface,” *Nature*, vol. 368, no. 6470, pp. 444–446, 1994.
- [40] A. Fallah Araghi *et al.*, “Enhanced chemical synthesis at soft interfaces: A universal reaction-adsorption mechanism in microcompartments,” *Physical Review Letters*, vol. 112, no. 2, p. 028 301, 2014.
- [41] D. N. Mortensen and E. R. Williams, “Theta-glass capillaries in electrospray ionization: Rapid mixing and short droplet lifetimes,” *Analytical Chemistry*, vol. 86, no. 18, pp. 9315–9321, 2014.
- [42] T. Müller, A. Badu-Tawiah, and R. G. Cooks, “Accelerated carbon carbon bond-forming reactions in preparative electrospray,” *Angewandte Chemie International Edition*, vol. 51, no. 47, pp. 11 832–11 835, 2012.
- [43] X. Yan, H. Cheng, and R. N. Zare, “Two-phase reactions in microdroplets without the use of phase-transfer catalysts,” *Angewandte Chemie International Edition*, vol. 129, no. 13, pp. 3616–3619, 2017.

- [44] X. Yan, Y.-H. Lai, and R. N. Zare, "Preparative microdroplet synthesis of carboxylic acids from aerobic oxidation of aldehydes," *Chemical Science*, vol. 9, no. 23, pp. 5207–5211, 2018.
- [45] S. Banerjee and R. N. Zare, "Syntheses of isoquinoline and substituted quinolines in charged microdroplets," *Angewandte Chemie International Edition*, vol. 127, no. 49, pp. 15 008–15 012, 2015.
- [46] A. Li, Q. Luo, S.-J. Park, and R. G. Cooks, "Synthesis and catalytic reactions of nanoparticles formed by electrospray ionization of coinage metals," *Angewandte Chemie International Edition*, vol. 53, no. 12, pp. 3147–3150, 2014.
- [47] L. Zhao-Miao, Y. Yang, D. Yu, and P. Yan, "Advances in droplet-based microfluidic technology and its applications," *Chinese Journal of Analytical Chemistry*, vol. 45, no. 2, pp. 282–296, 2017.
- [48] L. Liu, N. Xiang, and Z. Ni, "Droplet-based microreactor for the production of micro/nano-materials," *Electrophoresis*, vol. 41, no. 10-11, pp. 833–851, 2020.
- [49] R. Ameloot, F. Vermoortele, W. Vanhove, M. B. Roeffaers, B. F. Sels, and D. E. De Vos, "Interfacial synthesis of hollow metal–organic framework capsules demonstrating selective permeability," *Nature Chemistry*, vol. 3, no. 5, pp. 382–387, 2011.
- [50] Z. Yu, C.-F. Wang, L. Ling, L. Chen, and S. Chen, "Triphase microfluidic-directed self-assembly: Anisotropic colloidal photonic crystal supraparticles and multicolor patterns made easy," *Angewandte Chemie International Edition*, vol. 124, no. 10, pp. 2425–2428, 2012.

- [51] T. Chow, “Wetting of rough surfaces,” *Journal of Physics: Condensed Matter*, vol. 10, no. 27, p. L445, 1998.
- [52] M. Kuang, L. Wang, and Y. Song, “Controllable printing droplets for high-resolution patterns,” *Advanced Materials*, vol. 26, no. 40, pp. 6950–6958, 2014.
- [53] J. Sun, B. Bao, M. He, H. Zhou, and Y. Song, “Recent advances in controlling the depositing morphologies of inkjet droplets,” *ACS Applied Materials & Interfaces*, vol. 7, no. 51, pp. 28 086–28 099, 2015.
- [54] A. Méndez-Vilas, A. B. Jódar-Reyes, and M. L. González-Martín, “Ultrasmall liquid droplets on solid surfaces: Production, imaging, and relevance for current wetting research,” *Small*, vol. 5, no. 12, pp. 1366–1390, 2009.
- [55] M. Paine, M. Alexander, K. Smith, M Wang, and J. Stark, “Controlled electrospray pulsation for deposition of femtoliter fluid droplets onto surfaces,” *Journal of Aerosol Science*, vol. 38, no. 3, pp. 315–324, 2007.
- [56] S. C. Thickett, C. Neto, and A. T. Harris, “Biomimetic surface coatings for atmospheric water capture prepared by dewetting of polymer films,” *Advanced Materials*, vol. 23, no. 32, pp. 3718–3722, 2011.
- [57] A. Verma and A. Sharma, “Enhanced self-organized dewetting of ultrathin polymer films under water-organic solutions: Fabrication of sub-micrometer spherical lens arrays,” *Advanced Materials*, vol. 22, no. 46, pp. 5306–5309, 2010.

- [58] E. Lepeltier, C. Bourgaux, and P. Couvreur, “Nanoprecipitation and the “ouzo effect”: Application to drug delivery devices,” *Advanced Drug Delivery Reviews*, vol. 71, pp. 86–97, 2014.
- [59] V. C. F. Mosqueira, P. Legrand, H. Pinto Alphandary, F. Puisieux, and G. Barratt, “Poly (d, l-lactide) nanocapsules prepared by a solvent displacement process: Influence of the composition on physicochemical and structural properties,” *Journal of Pharmaceutical Sciences*, vol. 89, no. 5, pp. 614–626, 2000.
- [60] R. Bodmeier, H. Chen, P. Tyle, and P. Jarosz, “Spontaneous formation of drug-containing acrylic nanoparticles,” *Journal of Microencapsulation*, vol. 8, no. 2, pp. 161–170, 1991.
- [61] A. Ma, J. Xu, and H. Xu, “Impact of spontaneously adsorbed hydroxide ions on emulsification via solvent shifting,” *The Journal of Physical Chemistry C*, vol. 118, no. 40, pp. 23 175–23 180, 2014.
- [62] C. Solans, D. Morales, and M. Homs, “Spontaneous emulsification,” *Current Opinion in Colloid & Interface Science*, vol. 22, pp. 88–93, 2016.
- [63] X. H. Zhang and W. Ducker, “Formation of interfacial nanodroplets through changes in solvent quality,” *Langmuir*, vol. 23, no. 25, pp. 12 478–12 480, 2007.
- [64] X. Zhang, J. Ren, H. Yang, Y. He, J. Tan, and G. G. Qiao, “From transient nanodroplets to permanent nanolenses,” *Soft Matter*, vol. 8, no. 16, pp. 4314–4317, 2012.
- [65] D. Lohse and X. Zhang, “Surface nanobubbles and nanodroplets,” *Reviews of Modern Physics*, vol. 87, no. 3, pp. 981–1035, 2015.

- [66] X. Zhang *et al.*, “Formation of surface nanodroplets under controlled flow conditions,” *Proceedings of the National Academy of Sciences*, vol. 112, no. 30, pp. 9253–9257, 2015.
- [67] S. Grossmann and D. Lohse, “Fluctuations in turbulent rayleigh–bénard convection: The role of plumes,” *Physics of Fluids*, vol. 16, no. 12, pp. 4462–4472, 2004.
- [68] B. Dyett, A. Kiyama, M. Rump, Y. Tagawa, D. Lohse, and X. Zhang, “Growth dynamics of surface nanodroplets during solvent exchange at varying flow rates,” *Soft Matter*, vol. 14, no. 25, pp. 5197–5204, 2018.
- [69] G. I. Taylor, “Dispersion of soluble matter in solvent flowing slowly through a tube,” *Proceedings of the Royal Society of London. Series A. Mathematical and Physical Sciences*, vol. 219, no. 1137, pp. 186–203, 1953.
- [70] H. Yu, Z. Lu, D. Lohse, and X. Zhang, “Gravitational effect on the formation of surface nanodroplets,” *Langmuir*, vol. 31, no. 46, pp. 12 628–12 634, 2015.
- [71] H. Yu, S. Maheshwari, J. Zhu, D. Lohse, and X. Zhang, “Formation of surface nanodroplets facing a structured microchannel wall,” *Lab on a Chip*, vol. 17, no. 8, pp. 1496–1504, 2017.
- [72] Z. Lu, S. Peng, and X. Zhang, “Influence of solution composition on the formation of surface nanodroplets by solvent exchange,” *Langmuir*, vol. 32, no. 7, pp. 1700–1706, 2016.

- [73] Z. Lu, H. Xu, H. Zeng, and X. Zhang, "Solvent effects on the formation of surface nanodroplets by solvent exchange," *Langmuir*, vol. 31, no. 44, pp. 12 120–12 125, 2015.
- [74] M. Li, L. Bao, H. Yu, and X. Zhang, "Formation of multicomponent surface nanodroplets by solvent exchange," *The Journal of Physical Chemistry C*, vol. 122, no. 15, pp. 8647–8654, 2018.
- [75] C. Xu *et al.*, "Collective interactions in the nucleation and growth of surface droplets," *Soft Matter*, vol. 13, no. 5, pp. 937–944, 2017.
- [76] H. Lhuissier, D. Lohse, and X. Zhang, "Spatial organization of surface nanobubbles and its implications in their formation process," *Soft Matter*, vol. 10, no. 7, pp. 942–946, 2014.
- [77] L. Bao, A. R. Rezk, L. Y. Yeo, and X. Zhang, "Highly ordered arrays of femtoliter surface droplets," *Small*, vol. 11, no. 37, pp. 4850–4855, 2015.
- [78] L. Bao, Z. Werbiuk, D. Lohse, and X. Zhang, "Controlling the growth modes of femtoliter sessile droplets nucleating on chemically patterned surfaces," *The Journal of Physical Chemistry Letters*, vol. 7, no. 6, pp. 1055–1059, 2016.
- [79] S. Peng, D. Lohse, and X. Zhang, "Spontaneous pattern formation of surface nanodroplets from competitive growth," *ACS Nano*, vol. 9, no. 12, pp. 11 916–11 923, 2015.
- [80] B. Dyett, H. Hao, D. Lohse, and X. Zhang, "Coalescence driven self-organization of growing nanodroplets around a microcap," *Soft Matter*, vol. 14, no. 14, pp. 2628–2637, 2018.

- [81] H. Yu, M. Rump, S. Maheshwari, L. Bao, and X. Zhang, “Growth of nanodroplets on a still microfiber under flow conditions,” *Physical Chemistry Chemical Physics*, vol. 20, no. 27, pp. 18 252–18 261, 2018.
- [82] Z. Lu, Z. Lu, S. Peng, X. Zhang, and Q. Liu, “Microwetting of ph-sensitive surface and anisotropic  $MoS_2$  surfaces revealed by femtoliter sessile droplets,” *Langmuir*, vol. 32, no. 43, pp. 11 273–11 279, 2016.
- [83] Z. Li, A. Kiyama, H. Zeng, D. Lohse, and X. Zhang, “Speeding up biphasic reactions with surface nanodroplets,” *Lab on a Chip*, vol. 20, no. 16, pp. 2965–2974, 2020.
- [84] Z. Li, A. Kiyama, H. Zeng, and X. Zhang, “Size effect on the reaction rate of surface nanodroplets,” *The Journal of Physical Chemistry C*, vol. 125, no. 28, pp. 15 324–15 334, 2021.
- [85] M. Li, B. Dyett, H. Yu, V. Bansal, and X. Zhang, “Functional femtoliter droplets for ultrafast nanoextraction and supersensitive online microanalysis,” *Small*, vol. 15, no. 1, p. 1 804 683, 2019.
- [86] J. B. You, D. Lohse, and X. Zhang, “Surface nanodroplet-based nanoextraction from sub-milliliter volumes of dense suspensions,” *Lab on a Chip*, vol. 21, pp. 2574–2585, 2021.
- [87] M. Li, B. Dyett, and X. Zhang, “Automated femtoliter droplet-based determination of oil–water partition coefficient,” *Analytical Chemistry*, vol. 91, no. 16, pp. 10 371–10 375, 2019.

- [88] M. Li, R. Cao, B. Dyett, and X. Zhang, “Encapsulated nanodroplets for enhanced fluorescence detection by nano-extraction,” *Small*, vol. 16, no. 47, p. 2004162, 2020.
- [89] B. Dyett, Q. Zhang, Q. Xu, X. Wang, and X. Zhang, “Extraordinary focusing effect of surface nanolenses in total internal reflection mode,” *ACS Central Science*, vol. 4, no. 11, pp. 1511–1519, 2018.
- [90] J. Qian *et al.*, “One-step nanoextraction and ultrafast microanalysis based on nanodroplet formation in an evaporating ternary liquid microfilm,” *Advanced Materials Technologies*, vol. 5, no. 2, p. 1900740, 2020.
- [91] M. Zhang, L. Wei, H. Chen, Z. Du, B. P. Binks, and H. Yang, “Compartmentalized droplets for continuous flow liquid–liquid interface catalysis,” *Journal of the American Chemical Society*, vol. 138, no. 32, pp. 10173–10183, 2016.
- [92] M. Morales, G. Luna, and R. Aparicio, “Comparative study of virgin olive oil sensory defects,” *Food Chemistry*, vol. 91, no. 2, pp. 293–301, 2005.
- [93] A. Turnbull, E. Slavcheva, and B. Shone, “Factors controlling naphthenic acid corrosion,” *Corrosion*, vol. 54, no. 11, pp. 922–930, 1998.
- [94] H. D. Dettman, N. Li, and J. Luo, “Refinery corrosion, organic acid structure, and athabasca bitumen,” in *CORROSION 2009*, NACE International, 2009.
- [95] H. Yousefi, H. Su, S. M. Imani, K. Alkhalidi, C. D. M. Filipe, and T. F. Didar, “Intelligent food packaging: A review of smart sensing technologies for monitoring food quality,” *ACS Sensors*, vol. 4, no. 4, pp. 808–821, 2019.

- [96] Z. Kerem, B. Bravdo, O. Shoseyov, and Y. Tugendhaft, "Rapid liquid chromatography–ultraviolet determination of organic acids and phenolic compounds in red wine and must," *Journal of Chromatography A*, vol. 1052, no. 1-2, pp. 211–215, 2004.
- [97] Y. H. Zhang and L. G. Danielsson, "Methods for determiningn-octanol-water partition constants," *TrAC Trends in Analytical Chemistry*, vol. 15, no. 4, pp. 188–196, 1996.
- [98] F. H. Clarke and N. M. Cahoon, "Ionization constants by curve fitting: Determination of partition and distribution coefficients of acids and bases and their ions," *Journal of Pharmaceutical Sciences*, vol. 76, no. 8, pp. 611–620, 1987.
- [99] C. T. Chiou, V. H. Freed, D. W. Schmedding, and R. L. Kohnert, "Partition coefficient and bioaccumulation of selected organic chemicals," *Environmental Science & Technology*, vol. 11, no. 5, pp. 475–478, 1977.
- [100] E. Baka, J. E. Comer, and K. Takács-Novák, "Study of equilibrium solubility measurement by saturation shake-flask method using hydrochlorothiazide as model compound," *Journal of Pharmaceutical and Biomedical Analysis*, vol. 46, no. 2, pp. 335–341, 2008.
- [101] A. Leo, C. Hansch, and D. Elkins, "Partition coefficients and their uses," *Chemical Reviews*, vol. 71, no. 6, pp. 525–616, 1971.
- [102] J. P. Kitt and J. M. Harris, "Confocal raman microscopy for in situ measurement of octanol–water partitioning within the pores of individual C18-functionalized chromatographic particles," *Analytical Chemistry*, vol. 87, no. 10, pp. 5340–5347, 2015.

- [103] B. Averill and P. Eldredge, *General chemistry: principles, patterns, and applications*. Washington, DC: Saylor Academy, 2015, p. 1472.
- [104] National Center for Biotechnology Information. PubChem Database, *Acetic acid*, *cid=176*, [(accessed on May 4, 2020)].
- [105] National Center for Biotechnology Information. PubChem Database, *Hep- tanoic acid*, *cid=8094*, [accessed on May 4, 2020].
- [106] National Center for Biotechnology Information. PubChem Database, *Gallic acid*, *cid=370*, [accessed on May 4, 2020].
- [107] National Center for Biotechnology Information. PubChem Database, *4-hydroxybenzoic acid*, *cid=135*, [accessed on Mar. 1, 2020].
- [108] National Center for Biotechnology Information. PubChem Database, *Benzoic acid*, *cid=243*, [accessed on Mar. 1, 2020].
- [109] H. Brown, D. McDaniel, and O Hafliger, *Determination of organic structures by physical methods*. Academic Press, Inc., New York, N. Y, 1955, pp. 567–662.
- [110] A. Leo, C. Hansch, and D. Elkins, “Partition coefficients and their uses,” *Chemical Reviews*, vol. 71, no. 6, pp. 525–616, 1971.
- [111] ChemSpider, *Trimesic acid*, *id=10665*.
- [112] M. Ramiasa *et al.*, “Contact line motion on nanorough surfaces: A thermally activated process,” *Journal of the American Chemical Society*, vol. 135, no. 19, pp. 7159–7171, 2013.

- [113] S. Vitale and J. Katz, “Liquid droplet dispersions formed by homogeneous liquid-liquid nucleation: The ouzo effect,” *Langmuir*, vol. 19, pp. 4105–4110, 2003.
- [114] T. N. Zemb *et al.*, “How to explain microemulsions formed by solvent mixtures without conventional surfactants,” *Proceedings of the National Academy of Sciences*, vol. 113, pp. 4260–4265, 2016.
- [115] M. A. Jeannot and F. F. Cantwell, “Solvent microextraction into a single drop,” *Analytical Chemistry*, vol. 68, no. 13, pp. 2236–2240, 1996.
- [116] G. J. Hanna and R. D. Noble, “Measurement of liquid-liquid interfacial kinetics,” *Chemical Reviews*, vol. 85, no. 6, pp. 583–598, 1985.
- [117] G. Laddha and a. E. Degaleesan, *Transport phenomena in liquid extraction*. McGraw-Hill New York, 1978, vol. 213, ch. 3.
- [118] J. Davies and E. Rideal, *Interfacial Phenomena*. Academic Press New York, 1961, ch. 7.
- [119] R. Aris, “On the dispersion of a solute in a fluid flowing through a tube,” *Proceedings of the Royal Society of London. Series A. Mathematical and Physical Sciences*, vol. 235, no. 1200, pp. 67–77, 1956.
- [120] R. Aris, “On the dispersion of a solute by diffusion, convection and exchange between phases,” *Proceedings of the Royal Society of London. Series A. Mathematical and Physical Sciences*, vol. 252, no. 1271, pp. 538–550, 1959.

- [121] J. Comer and K. Tam, “Lipophilicity profiles: Theory and measurement,” *Pharmacokinetic Optimization in Drug Research: Biological, Physicochemical and Computational Strategies*, pp. 275–304, 2001.
- [122] C Hansch, A Leo, and D Hoekman, “Exploring qsar. hydrophobic, electronic, and steric constants. acs professional reference book,” *ACS, Washington*, 1995.
- [123] C. Fang, H. Du, W. Jia, and Y. Xu, “Compositional differences and similarities between typical chinese baijiu and western liquor as revealed by mass spectrometry-based metabolomics,” *Metabolites*, vol. 9, no. 1, p. 2, 2019.
- [124] H. Yang, W. Fan, and Y. Xu, “Characterization of non-volatile organic acids in baijius (chinese liquors) based on bstfa derivatization coupled with gc-ms,” *Food and Fermentation Industries*, vol. 43, no. 5, pp. 192–197, 2017.
- [125] P. Sun, K. Huang, and H. Liu, “The nature of salt effect in enhancing the extraction of rare earths by non-functional ionic liquids: Synergism of salt anion complexation and hofmeister bias,” *Journal of Colloid and Interface Science*, vol. 539, pp. 214–222, 2019.
- [126] A. G. Gaonkar and R. D. Neuman, “Interfacial activity, extractant selectivity, and reversed micellization in hydrometallurgical liquid/liquid extraction systems,” *Journal of Colloid and Interface Science*, vol. 119, no. 1, pp. 251–261, 1987.
- [127] I. S. Elizarova and P. F. Luckham, “Layer-by-layer encapsulated nano-emulsion of ionic liquid loaded with functional material for extraction of  $Cd^{2+}$  ions from

- aqueous solutions,” *Journal of Colloid and Interface Science*, vol. 491, pp. 286–293, 2017.
- [128] L. Miller, “Preparative enantioseparations using supercritical fluid chromatography,” *Journal of Chromatography A*, vol. 1250, pp. 250–255, 2012.
- [129] Z. Wei, M. Li, H. Zeng, and X. Zhang, “Integrated nanoextraction and colorimetric reactions in surface nanodroplets for combinative analysis,” *Analytical Chemistry*, vol. 92, no. 18, pp. 12 442–12 450, 2020.
- [130] H. S. Fogler, *Essentials of Chemical Reaction Engineering: Essenti Chemica Reactio Engi.* Pearson Education, 2010, pp. 152–155.
- [131] B. P. Dyett and X. Zhang, “Accelerated formation of  $H_2$  nanobubbles from a surface nanodroplet reaction,” *ACS Nano*, vol. 14, no. 9, pp. 10 944–10 953, 2020.
- [132] P. W. Fedick, K. Iyer, Z. Wei, L. Avramova, G. O. Capek, and R. G. Cooks, “Screening of the suzuki cross-coupling reaction using desorption electrospray ionization in high-throughput and in leidenfrost droplet experiments,” *Journal of The American Society for Mass Spectrometry*, vol. 30, no. 10, pp. 2144–2151, 2019.
- [133] M. Girod, E. Moyano, D. I. Campbell, and R. G. Cooks, “Accelerated bimolecular reactions in microdroplets studied by desorption electrospray ionization mass spectrometry,” *Chemical Science*, vol. 2, no. 3, pp. 501–510, 2011.

- [134] R. M. Bain, C. J. Pulliam, and R. G. Cooks, “Accelerated hantzsch electro-spray synthesis with temporal control of reaction intermediates,” *Chemical Science*, vol. 6, no. 1, pp. 397–401, 2015.
- [135] J. B. Fenn, M. Mann, C. K. Meng, S. F. Wong, and C. M. Whitehouse, “Electrospray ionization—principles and practice,” *Mass Spectrometry Reviews*, vol. 9, no. 1, pp. 37–70, 1990.
- [136] J. K. Lee, H. G. Nam, and R. N. Zare, “Microdroplet fusion mass spectrometry: Accelerated kinetics of acid-induced chlorophyll demetallation,” *Quarterly Reviews of Biophysics*, vol. 50, 2017.
- [137] E. A. Crawford, C. Esen, and D. A. Volmer, “Real time monitoring of containerless microreactions in acoustically levitated droplets via ambient ionization mass spectrometry,” *Analytical Chemistry*, vol. 88, no. 17, pp. 8396–8403, 2016.
- [138] H. Chen, L. S. Eberlin, M. Nefliu, R. Augusti, and R. G. Cooks, “Organic reactions of ionic intermediates promoted by atmospheric-pressure thermal activation,” *Angewandte Chemie International Edition*, vol. 47, no. 18, pp. 3422–3425, 2008.
- [139] H. Chen, I. Cotte Rodríguez, and R. G. Cooks, “Cis-diol functional group recognition by reactive desorption electrospray ionization (DESI),” *Chemical Communications*, no. 6, pp. 597–599, 2006.
- [140] M. Rezaee, Y. Yamini, and M. Faraji, “Evolution of dispersive liquid–liquid microextraction method,” *Journal of Chromatography A*, vol. 1217, no. 16, pp. 2342–2357, 2010.

- [141] S. S. Wells and R. T. Kennedy, “High-throughput liquid–liquid extractions with nanoliter volumes,” *Analytical Chemistry*, vol. 92, no. 4, pp. 3189–3197, 2020.
- [142] M. Li, H. Yu, L. Bao, B. Dyett, and X. Zhang, “Controlled addition of new liquid component into surface droplet arrays by solvent exchange,” *Journal of Colloid and Interface Science*, vol. 543, pp. 164–173, 2019.
- [143] J. M. Park, A. Laio, M. Iannuzzi, and M. Parrinello, “Dissociation mechanism of acetic acid in water,” *Journal of the American Chemical Society*, vol. 128, no. 35, pp. 11 318–11 319, 2006.
- [144] A. Raza, A. S. Alketbi, R. Devarapalli, H. Li, and T. Zhang, “Refractory ultrathin nanocomposite solar absorber with superior spectral selectivity and thermal stability,” *Advanced Optical Materials*, vol. 8, no. 17, p. 2000 679, 2020.
- [145] Y. Wang, X. Wu, B. Shao, X. Yang, G. Owens, and H. Xu, “Boosting solar steam generation by structure enhanced energy management,” *Science Bulletin*, vol. 65, no. 16, pp. 1380–1388, 2020.
- [146] Y. Lu *et al.*, “Implementing hybrid energy harvesting in 3d spherical evaporator for solar steam generation and synergic water purification,” *Solar RRL*, vol. 4, no. 9, p. 2000 232, 2020.
- [147] R. Li, Y. Shi, M. Wu, S. Hong, and P. Wang, “Photovoltaic panel cooling by atmospheric water sorption–evaporation cycle,” *Nature Sustainability*, vol. 3, no. 8, pp. 636–643, 2020.

- [148] X. Guo *et al.*, “Bismuth oxychloride (biocl)/copper phthalocyanine (cutnpc) heterostructures immobilized on electrospun polyacrylonitrile nanofibers with enhanced activity for floating photocatalysis,” *Journal of Colloid and Interface Science*, vol. 525, pp. 187–195, 2018.
- [149] J. H. Kim, M. K. Joshi, J. Lee, C. H. Park, and C. S. Kim, “Polydopamine-assisted immobilization of hierarchical zinc oxide nanostructures on electrospun nanofibrous membrane for photocatalysis and antimicrobial activity,” *Journal of Colloid and Interface Science*, vol. 513, pp. 566–574, 2018.
- [150] D. C. Bailey and S. H. Langer, “Immobilized transition-metal carbonyls and related catalysts,” *Chemical Reviews*, vol. 81, no. 2, pp. 109–148, 1981.
- [151] G. Fan *et al.*, “Mussel-inspired immobilization of photocatalysts with synergistic photocatalytic–photothermal performance for water remediation,” *ACS Applied Materials & Interfaces*, vol. 13, pp. 31 066–31 076, 2021.
- [152] X. Zhang, Z. Wei, H. Choi, H. Hao, and H. Yang, “Oiling-out crystallization of beta-alanine on solid surfaces controlled by solvent exchange,” *Advanced Materials Interfaces*, vol. 8, no. 2, p. 2001 200, 2021.
- [153] Q. Zhu and Q. Xu, “Immobilization of ultrafine metal nanoparticles to high-surface-area materials and their catalytic applications,” *Chem*, vol. 1, no. 2, pp. 220–245, 2016.
- [154] E. V. Rebrov, E. A. Klinger, A. Berenguer-Murcia, E. M. Sulman, and J. C. Schouten, “Selective hydrogenation of 2-methyl-3-butyne-2-ol in a wall-coated

- capillary microreactor with a pd25zn75/tio2 catalyst,” *Organic Process Research & Development*, vol. 13, no. 5, pp. 991–998, 2009.
- [155] L. Zhang *et al.*, “Facile immobilization of ag nanoparticles on microchannel walls in microreactors for catalytic applications,” *Chemical Engineering Journal*, vol. 309, pp. 691–699, 2017.
- [156] C Merckle and J Blümel, “Improved rhodium hydrogenation catalysts immobilized on oxidic supports,” *Advanced Synthesis & Catalysis*, vol. 345, no. 5, pp. 584–588, 2003.
- [157] F. Gregson, J. Robinson, R. Miles, C. Royall, and J. Reid, “Drying kinetics of salt solution droplets: Water evaporation rates and crystallization,” *The Journal of Physical Chemistry B*, vol. 123, no. 1, pp. 266–276, 2018.
- [158] O. S. Abianeh, C.-P. Chen, and S. Mahalingam, “Numerical modeling of multi-component fuel spray evaporation process,” *International Journal of Heat and Mass Transfer*, vol. 69, pp. 44–53, 2014.
- [159] S Shakiba, S Mansouri, C Selomulya, and M. Woo, “The role of the intermediate stage of drying on particle in-situ crystallization in spray dryers,” *Powder Technology*, vol. 323, pp. 357–366, 2018.
- [160] H. Tan, C. Diddens, P. Lv, J. G. Kuerten, X. Zhang, and D. Lohse, “Evaporation-triggered microdroplet nucleation and the four life phases of an evaporating ouzo drop,” *Proceedings of the National Academy of Sciences of the United States of America*, vol. 113, no. 31, pp. 8642–8647, 2016.

- [161] H. Yu, S. Peng, L. Lei, J. Zhang, T. L. Greaves, and X. Zhang, “Large scale flow-mediated formation and potential applications of surface nanodroplets,” *ACS Applied Materials & Interfaces*, vol. 8, no. 34, pp. 22 679–22 687, 2016.
- [162] P. Xu *et al.*, “Use of iron oxide nanomaterials in wastewater treatment: A review,” *Science of the Total Environment*, vol. 424, pp. 1–10, 2012.
- [163] M. Mishra and D. Chun, “ $\alpha$ - $Fe_2O_3$  as a photocatalytic material: A review,” *Applied Catalysis A: General*, vol. 498, pp. 126–141, 2015.
- [164] M. Khedr, K. A. Halim, and N. Soliman, “Synthesis and photocatalytic activity of nano-sized iron oxides,” *Materials Letters*, vol. 63, no. 6-7, pp. 598–601, 2009.
- [165] S. Ge *et al.*, “Facile hydrothermal synthesis of iron oxide nanoparticles with tunable magnetic properties,” *The Journal of Physical Chemistry C*, vol. 113, no. 31, pp. 13 593–13 599, 2009.
- [166] S. Li, T. Zhang, R. Tang, H. Qiu, C. Wang, and Z. Zhou, “Solvothermal synthesis and characterization of monodisperse superparamagnetic iron oxide nanoparticles,” *Journal of Magnetism and Magnetic Materials*, vol. 379, pp. 226–231, 2015.
- [167] A. Lassoued, M. S. Lassoued, B. Dkhil, A. Gadri, and S. Ammar, “Structural, optical and morphological characterization of Cu-doped  $\alpha$ - $Fe_2O_3$  nanoparticles synthesized through co-precipitation technique,” *Journal of Molecular Structure*, vol. 1148, pp. 276–281, 2017.
- [168] C. Gao, F. Lyu, and Y. Yin, “Encapsulated metal nanoparticles for catalysis,” *Chemical Reviews*, 2020.

- [169] A. Bertran, S. Sandoval, J. Oró-Solé, Àlvar Sánchez, and G. Tobias, “Particle size determination from magnetization curves in reduced graphene oxide decorated with monodispersed superparamagnetic iron oxide nanoparticles,” *Journal of Colloid and Interface Science*, vol. 566, pp. 107–119, 2020.
- [170] H. Yang *et al.*, “A direct surface modification of iron oxide nanoparticles with various poly(amino acid)s for use as magnetic resonance probes,” *Journal of Colloid and Interface Science*, vol. 391, pp. 158–167, 2013.
- [171] R. Hufschmid *et al.*, “Synthesis of phase-pure and monodisperse iron oxide nanoparticles by thermal decomposition,” *Nanoscale*, vol. 7, no. 25, pp. 11 142–11 154, 2015.
- [172] Z. Chen, “Size and shape controllable synthesis of monodisperse iron oxide nanoparticles by thermal decomposition of iron oleate complex,” *Synthesis and Reactivity in Inorganic, Metal-Organic, and Nano-Metal Chemistry*, vol. 42, no. 7, pp. 1040–1046, 2012.
- [173] N. Koga and Y. Sato, “Formation and transformation kinetics of amorphous iron (iii) oxide during the thermally induced transformation of ferrous oxalate dihydrate in air,” *The Journal of Physical Chemistry A*, vol. 115, no. 2, pp. 141–151, 2011.
- [174] D. Lohse and X. Zhang, “Physicochemical hydrodynamics of droplets out of equilibrium,” *Nature Reviews Physics*, vol. 2, no. 8, pp. 426–443, 2020.

- [175] A. Grosvenor, B. Kobe, M. Biesinger, and N. McIntyre, "Investigation of multiplet splitting of Fe 2p XPS spectra and bonding in iron compounds," *Surface and Interface Analysis*, vol. 36, no. 12, pp. 1564–1574, 2004.
- [176] J. Mann *et al.*, "Metal oxide–zeolite composites in transformation of methanol to hydrocarbons: Do iron oxide and nickel oxide matter?" *RSC Advances*, vol. 6, no. 79, pp. 75 166–75 177, 2016.
- [177] D. Wilson and M. Langell, "XPS analysis of oleylamine/oleic acid capped  $Fe_3O_4$  nanoparticles as a function of temperature," *Applied Surface Science*, vol. 303, pp. 6–13, 2014.
- [178] T. Yamashita and P. Hayes, "Analysis of XPS spectra of  $Fe^{2+}$  and  $Fe^{3+}$  ions in oxide materials," *Applied Surface Science*, vol. 254, no. 8, pp. 2441–2449, 2008.
- [179] D. S. Jensen *et al.*, "Silicon (100)/ $SiO_2$  by XPS," *Surface Science Spectra*, vol. 20, no. 1, pp. 36–42, 2013.
- [180] B. Sayyed, A. Chatterjee, S. Kanetkar, S. Badrinarayanan, and S. Date, "Surface characterisation of an iron oxide catalyst (ethylbenzene  $\rightarrow$  styrene): An XPS study," in *Proceedings of the Indian Academy of Sciences-Chemical Sciences*, Springer, vol. 95, 1985, pp. 291–295.
- [181] Y. Ch'Ng, K. Loh, W. Daud, and A. Mohamad, "Synthesis and characterization of sulfonated graphene oxide nanofiller for polymer electrolyte membrane," in *IOP Conference Series: Materials Science and Engineering*, IOP Publishing, vol. 160, 2016, pp. 12 035–12 042.

- [182] X. Peng and M. Barteau, "Spectroscopic characterization of surface species derived from  $HCOOH$ ,  $CH_3COOH$ ,  $CH_3OH$ ,  $C_2H_5OH$ ,  $HCOOCH_3$ , and  $C_2H_2$  on MgO thin film surfaces," *Surface Science*, vol. 224, no. 1-3, pp. 327–347, 1989.
- [183] A. Ullrich, M. M. Rahman, P. Longo, and S. Horn, "Synthesis and high-resolution structural and chemical analysis of iron-manganese-oxide core-shell nanocubes," *Scientific Reports*, vol. 9, no. 1, pp. 1–9, 2019.
- [184] M. M. Lin and D. K. Kim, "In situ thermolysis of magnetic nanoparticles using non-hydrated iron oleate complex," *Journal of Nanoparticle Research*, vol. 14, no. 2, pp. 1–13, 2012.
- [185] P. Roonasi and A. Holmgren, "A fourier transform infrared (FTIR) and thermogravimetric analysis (TGA) study of oleate adsorbed on magnetite nanoparticle surface," *Applied Surface Science*, vol. 255, no. 11, pp. 5891–5895, 2009.
- [186] L. M. Bronstein *et al.*, "Influence of iron oleate complex structure on iron oxide nanoparticle formation," *Chemistry of Materials*, vol. 19, no. 15, pp. 3624–3632, 2007.
- [187] T. Nakamoto, M. Hanaya, M. Katada, K. Endo, S. Kitagawa, and H. Sano, "Phase transition in a crystal of the mixed-valence trinuclear iron cyanoacetate complex  $[Fe_3O(O_2CCH_2CN)_6(H_2O)_3]$ ," *Inorganic Chemistry*, vol. 36, no. 20, pp. 4347–4359, 1997.

- [188] K. Chang *et al.*, “Synergistic effects of hydrophobicity and gas barrier properties on the anticorrosion property of pmma nanocomposite coatings embedded with graphene nanosheets,” *Polymer Chemistry*, vol. 5, no. 3, pp. 1049–1056, 2013.
- [189] T. Stirner, D. Scholz, and J. Sun, “Ab initio simulation of structure and surface energy of low-index surfaces of stoichiometric  $\alpha - Fe_2O_3$ ,” *Surface Science*, vol. 671, pp. 11–16, 2018.
- [190] S. Wang, Y. Min, and S. Yu, “Synthesis and magnetic properties of uniform hematite nanocubes,” *The Journal of Physical Chemistry C*, vol. 111, no. 9, pp. 3551–3554, 2007.
- [191] J. Meijer and L. Rossi, “Preparation, properties, and applications of magnetic hematite microparticles,” *Soft Matter*, 2021.
- [192] J. N. Israelachvili, *Intermolecular and surface forces*. Academic press, 2015, pp. 107–130.
- [193] H. T. Hai *et al.*, “Size control and characterization of wustite (core)/spinel (shell) nanocubes obtained by decomposition of iron oleate complex,” *Journal of Colloid and Interface Science*, vol. 346, no. 1, pp. 37–42, 2010.
- [194] R. Pilot, R. Signorini, C. Durante, L. Orian, M. Bhamidipati, and L. Fabris, “A review on surface-enhanced raman scattering,” *Biosensors*, vol. 9, no. 2, p. 57, 2019.

- [195] S. Nie and S. R. Emory, "Probing single molecules and single nanoparticles by surface-enhanced raman scattering," *Science*, vol. 275, no. 5303, pp. 1102–1106, 1997.
- [196] Y. C. Cao, R. Jin, and C. A. Mirkin, "Nanoparticles with raman spectroscopic fingerprints for dna and rna detection," *Science*, vol. 297, no. 5586, pp. 1536–1540, 2002.
- [197] J. Homola, "Surface plasmon resonance sensors for detection of chemical and biological species," *Chemical Reviews*, vol. 108, no. 2, pp. 462–493, 2008.
- [198] M. P. Cecchini, V. A. Turek, J. Paget, A. A. Kornyshev, and J. B. Edel, "Self-assembled nanoparticle arrays for multiphase trace analyte detection," *Nature Materials*, vol. 12, no. 2, pp. 165–171, 2013.
- [199] S. Yang, X. Dai, B. B. Stogin, and T. Wong, "Ultrasensitive surface-enhanced raman scattering detection in common fluids," *Proceedings of the National Academy of Sciences*, vol. 113, no. 2, pp. 268–273, 2016.
- [200] D. Li *et al.*, "Nanosol SERS quantitative analytical method: A review," *TrAC Trends in Analytical Chemistry*, vol. 127, p. 115 885, 2020.
- [201] J. Hao, M. Han, S. Han, X. Meng, T. Su, and Q. K. Wang, "SERS detection of arsenic in water: A review," *Journal of Environmental Sciences*, vol. 36, pp. 152–162, 2015.
- [202] D. Ciialla *et al.*, "Surface-enhanced raman spectroscopy (SERS): Progress and trends," *Analytical and Bioanalytical Chemistry*, vol. 403, no. 1, pp. 27–54, 2012.

- [203] M. F. Cardinal *et al.*, “Expanding applications of SERS through versatile nanomaterials engineering,” *Chemical Society Reviews*, vol. 46, no. 13, pp. 3886–3903, 2017.
- [204] P. A. Mosier-Boss, “Review of SERS substrates for chemical sensing,” *Nanomaterials*, vol. 7, no. 6, p. 142, 2017.
- [205] Y. Oh, M. Kang, M. Park, and K. Jeong, “Engineering hot spots on plasmonic nanopillar arrays for SERS: A review,” *BioChip Journal*, vol. 10, no. 4, pp. 297–309, 2016.
- [206] C. Cheng *et al.*, “Fabrication and SERS performance of silver-nanoparticle-decorated si/zno nanotrees in ordered arrays,” *ACS Applied Materials & Interfaces*, vol. 2, no. 7, pp. 1824–1828, 2010.
- [207] D. Liu, Q. Wang, and J. Hu, “Fabrication and characterization of highly ordered au nanocone array-patterned glass with enhanced SERS and hydrophobicity,” *Applied Surface Science*, vol. 356, pp. 364–369, 2015.
- [208] J. Chu *et al.*, “A highly-ordered and uniform sunflower-like dendritic silver nanocomplex array as reproducible SERS substrate,” *RSC Advances*, vol. 5, no. 5, pp. 3860–3867, 2015.
- [209] S. Xu *et al.*, “Highly ordered graphene-isolated silver nanodot arrays as SERS substrate for detection of urinary nucleosides,” *Laser Physics*, vol. 25, no. 11, p. 115 601, 2015.
- [210] J. Cai *et al.*, “SERS hotspots distribution of the highly ordered noble metal arrays on flexible substrates,” *Optical Materials*, p. 111 779, 2021.

- [211] B. Chen *et al.*, “Green synthesis of large-scale highly ordered core@ shell nanoporous Au@ Ag nanorod arrays as sensitive and reproducible 3d SERS substrates,” *ACS Applied Materials & Interfaces*, vol. 6, no. 18, pp. 15 667–15 675, 2014.
- [212] Y. Lu, W. Chiang, C. Liu, J. P. Chu, H. Ho, and C. Hsueh, “Wafer-scale SERS metallic nanotube arrays with highly ordered periodicity,” *Sensors and Actuators B: Chemical*, vol. 329, p. 129 132, 2021.
- [213] J. Henzie, M. Grünwald, A. Widmer-Cooper, P. L. Geissler, and P. Yang, “Self-assembly of uniform polyhedral silver nanocrystals into densest packings and exotic superlattices,” *Nature Materials*, vol. 11, no. 2, pp. 131–137, 2012.
- [214] Z. Huang, G. Meng, Q. Huang, Y. Yang, C. Zhu, and C. Tang, “Improved SERS performance from au nanopillar arrays by abridging the pillar tip spacing by ag sputtering,” *Advanced Materials*, vol. 22, no. 37, pp. 4136–4139, 2010.
- [215] H. Kang, C. Heo, H. C. Jeon, S. Y. Lee, and S. Yang, “Durable plasmonic cap arrays on flexible substrate with real-time optical tunability for high-fidelity SERS devices,” *ACS Applied Materials & Interfaces*, vol. 5, no. 11, pp. 4569–4574, 2013.
- [216] N. A. Hatab *et al.*, “Free-standing optical gold bowtie nanoantenna with variable gap size for enhanced raman spectroscopy,” *Nano Letters*, vol. 10, no. 12, pp. 4952–4955, 2010.

- [217] J. Wang, C. Qiu, X. Mu, H. Pang, X. Chen, and D. Liu, “Ultrasensitive SERS detection of rhodamine 6g and p-nitrophenol based on electrochemically roughened nano-Au film,” *Talanta*, vol. 210, p. 120 631, 2020.
- [218] D. Xu, F. Teng, Z. Wang, and N. Lu, “Droplet-confined electroless deposition of silver nanoparticles on ordered superhydrophobic structures for high uniform SERS measurements,” *ACS Applied Materials & Interfaces*, vol. 9, no. 25, pp. 21 548–21 553, 2017.
- [219] Z. Wei *et al.*, “In-situ fabrication of metal oxide nanocaps based on biphasic reactions with surface nanodroplets,” *Journal of Colloid and Interface Science*, vol. 608, pp. 2235–2245, 2022.
- [220] L. Zhang, Y. Shen, A. Xie, S. Li, B. Jin, and Q. Zhang, “One-step synthesis of monodisperse silver nanoparticles beneath vitamin E langmuir monolayers,” *The Journal of Physical Chemistry B*, vol. 110, no. 13, pp. 6615–6620, 2006.
- [221] C. Wu, E. Chen, and J. Wei, “Surface enhanced raman spectroscopy of Rhodamine 6G on agglomerates of different-sized silver truncated nanotriangles,” *Colloids and Surfaces A: Physicochemical and Engineering Aspects*, vol. 506, pp. 450–456, 2016.
- [222] R. D. Deegan, O. Bakajin, T. F. Dupont, G. Huber, S. R. Nagel, and T. A. Witten, “Capillary flow as the cause of ring stains from dried liquid drops,” *Nature*, vol. 389, no. 6653, pp. 827–829, 1997.
- [223] E. A. Kumar, N. R. Barveen, T. J. Wang, T. Kokulnathan, and Y. H. Chang, “Development of SERS platform based on ZnO multipods decorated with Ag

nanospheres for detection of 4-nitrophenol and rhodamine 6g in real samples,”

*Microchemical Journal*, vol. 170, p. 106 660, 2021.